

# 國立交通大學

應用化學系

碩士論文

利用電荷自洽密度泛函緊束縛方法探討導電高  
分子和碳奈米結構的幾何、電性和振動性質

**Geometric, electronic, and vibrational  
properties of conductive polymers and  
carbon nanostructures studied using the  
SCC-DFTB method**

研究生：李文凡

指導教授：魏恆理 教授

中華民國九十八年六月

利用電荷自洽密度泛函緊束縛方法探討導電高分子和碳奈米結構的幾何、電性和  
振動性質

**Geometric, electronic, and vibrational properties of conductive polymers and  
carbon nanostructures studied using the SCC-DFTB method**

研 究 生：李文凡

Student : Wun-Fan Li

指 導 教 授：魏恆理

Advisor : Henryk Witek

國 立 交 通 大 學

應 用 化 學 系

碩 士 論 文



National Chiao Tung University

in partial Fulfillment of the Requirements

for the Degree of

Master

in

Applied Chemistry

June 2009

Hsinchu, Taiwan, Republic of China

中華民國九十八年六月

# 利用電荷自洽密度泛函緊束縛方法探討導電高 分子和碳奈米結構的幾何、電性和振動性質

學生：李文凡

指導教授：魏恆理

國立交通大學應用化學系

## 摘要

電荷自洽密度泛函緊束縛方法（以下簡稱 SCC-DFTB）已被成功地應用在不同的化學系統的結構，電性，和振動性質上：1. 共軛雜環高分子，2. 奈米鑽石，3. 多環芳香族化合物-石墨片和 HPB 分子，4. 單層和多層富勒烯，5. 奈米碳管。我們觀察了一些新的題目。1. 對於共軛雜環高分子的研究，包括順一反式聚乙炔，聚環戊二烯，聚吡咯，聚吡喃，和聚噻吩。我們探討了能階差，電子態密度，偶極矩，四極矩和極化率等等的性質。這些性質整體而言呈現了收斂的行為。2. 對於奈米鑽石，我們計算了四面體和八面體結構之奈米鑽石的拉曼光譜。這些光譜擁有實驗得到之鑽石拉曼光譜特有的位於 1332 波數的訊號。3. 多環芳香族化合物的拉曼光譜已經以電荷自洽密度泛函緊束縛方法計算得到。4. 我們已經計算得到了單層富勒烯的電子和振動性質。我們也探討了內嵌水分子和乙炔之富勒烯包合物的振動光譜。我們發現如果外層的富勒烯足夠大，則裡面分子的振動光譜訊號會完全被外層富勒烯遮蔽。5. 我們運用了兩種不同的 SCC-DFTB 分散力模型計算了  $C_{60}@C_{240}$  的位能面。這兩種分散力模型分別是 Slater-Kirkwood 形式和 Lennard-Jones 形式。在以 Lennard-Jones 模型得到的結果中， $C_{60}$  轉動的能障僅僅只有 1.62 Kcal/mol。這指明在室溫之下， $C_{60}$  能在  $C_{240}$  裡面自由轉動，

並且位能面上存在許多局部的最小值。對於多層富勒烯之 0 結構的研究結果和  $C_{60}@C_{240}$  的位能面研究一致：對於只有單層差距的多層富勒烯 ( $C_{60}@C_{240}$  ,  $C_{240}@C_{540}$  , 和  $C_{60}@C_{240}@C_{540}$  ) , 內層富勒烯會坐落在中心點。而對於更大層距的多層富勒烯 ( $C_{60}@C_{540}$  ,  $C_{60}@C_{960}$  , 和  $C_{240}@C_{960}$  ) , 內層富勒烯傾向停留在外層富勒烯壁的附近。多層富勒烯之振動光譜的結果和富勒烯包合物的結果相似。這些光譜指出, 只要外層富勒烯的尺寸足夠大, 內層富勒烯的訊號就會被遮蔽。

5. 我們計算了不同尺寸和長度之扶手椅型單層奈米碳管的拉曼光譜。即使是在此研究中最長的碳管模型: 15 奈米的 (5,5) 單層奈米碳管, 朝著實驗所得之單層奈米碳管拉曼光譜的收斂仍未達到。目前的研究闡述了 SCC-DFTB 方法對於研究大分子性質和這些性質收斂至固態材料的能力和限制。



# Geometric, electronic, and vibrational properties of the conductive polymers and carbon nanostructures studied using the SCC-DFTB method

Student: Wun-Fan Li

Advisor: Henryk Witek

Department of Applied Chemistry  
National Chiao Tung University



## Abstract

The SCC-DFTB method has been applied for studying the geometrical, electronic, and vibrational properties of various chemical systems. The systems can be divided into following categories: 1. conjugated heterocyclic polymer chains, 2. nanodiamonds, 3. polycyclic aromatic hydrocarbons (PAHs) including graphene flakes and hexa-peri-benzacoronenes (HPBs), 4. single and multi-shell fullerenes and, 5. carbon nanotubes. Several new topics have been investigated. 1. The study on the conjugated heterocyclic oligomer chains, including trans-cisoid polyacetylene, polycyclopentadiene, polypyrrole, polyfuran, and polythiophene, shows overall convergent behavior of various properties including HOMO-LUMO gaps, DOS, dipole moment, quadrupole moment and polarizability. 2. For nanodiamonds, the Raman spectra of both series of octahedral and tetrahedral diamonds show an evidence of the unique peak at  $1332\text{ cm}^{-1}$ , which was previously observed in

experimental Raman spectra of diamond. 3. The Raman spectra of the finite PAHs have been computed out using the SCC-DFTB method. 4. The electronic and vibrational properties of single-shell fullerenes have been calculated. The vibrational spectra of endohedral fullerenes with inserted water and acetylene molecules have been discussed for different size of the encapsulating fullerene. It is found that when the cage is large enough, the signal from the inner molecule is completely shielded by the fullerene cage. The PES of  $C_{60}@C_{240}$  have been scanned with two types of dispersion-corrected SCC-DFTB models, Slater-Kirkwood type and Lennard-Jones type. The energy barrier for  $C_{60}$  to rotate is merely 1.62 Kcal/mol in the LJ scheme, which indicates that  $C_{60}$  can freely rotate at room temperature and there exist many energy local minima in the PES. The geometric structures of multi-shell fullerenes are in accord with the  $C_{60}@C_{240}$  PES study: for the multi-fullerene cages with only one shell difference ( $C_{60}@C_{240}$ ,  $C_{240}@C_{540}$ , and  $C_{60}@C_{240}@C_{540}$ ), the inner fullerene is located in the center. But for the aggregates with larger spacing between shells ( $C_{60}@C_{540}$ ,  $C_{60}@C_{960}$ , and  $C_{240}@C_{960}$ ), the inner fullerenes prefer to stay near the outer cage. Vibrational spectra of the multi-shell fullerenes lead to similar conclusions as those of the endohedral molecule-fullerene complexes. They show that if the cage is large enough, the signal from the inner fullerene is masked. 5. Raman spectra of armchair single-wall carbon nanotubes (SWNT) with different diameters and lengths are presented. The convergence toward the experimental Raman spectra of “infinitely” long SWNT is still not achieved even for the longest studied presently model, i.e. a 15nm (5,5) armchair SWNT. The present study illustrates the capability and limitations of the SCC-DFTB method for studying the properties of large molecules and their convergence toward the corresponding solid state materials.

# Acknowledgments

First of all, I would like to give my honest thanks to my advisor Henryk. He gave me a lot of precious guides in my research, and also offered me an opportunity so that I could stay in Nagoya for two months and enjoy the research there. I would like to thank my lab mates: Chien-Pin, Christopher, Amy, and also the former lab mates Mong-Jhu and Chun-Hao. When I entered this lab, I almost knew nothing about quantum chemistry, linux operating system, mathematics, even English. They helped me in every aspect and let me grow fast. Especially I appreciate the help from Chien-Pin. He taught me how to run SCC-DFTB, how to write a code, and also we had many helpful discussions on my research. I would like to thank people who helped me during my stay in Nagoya University. Prof. Irle gave me several interesting topics on the carbon nanostructures and helped me to dig into these topics. I also had a wonderful time with Nishimura-san, Hara-san, Xiao-Mei and Dr. Ying and Dr. Jiang. They were very kind and friendly. I would like to thank my parents who support me both mentally and economically every time when I meet difficulties. Especially, I appreciate my grandmother, who made much effort all the way with my growth. I also would like to thank my partner Tina, we had many precious experiences during these two years and grow up together. Thank the Lord for giving us these treasurable times. The brothers and sisters in church are definitely my firm support. Thank everyone in the brothers' home, especially Daniel, who relaxes me invisibly. I also thank the dear working saints, the saints of division 407. They are very cute and make me feel warm. I really enjoy and love the church life in 407, enjoy the love among the brothers and sisters. In the end, I would like to thank the Lord, who gave me every experience here and led me through this stage in my life. Like what said in Psalm 23 : Jehovah is my Shepherd;

I will lack nothing. He makes me lie down in green pastures; He leads me beside waters of rest. He restores my soul; He guides me on the paths of righteousness for His name's sake. Even though I walk through the valley of the shadow of death, I do not fear evil, for You are with me; Your rod and Your staff, They comfort me. You spread a table before me in the presence of my adversaries. You anoint my head with oil; my cup runs over. Sure goodness and lovingkindness will follow me all the days of my life, and I will dwell in the house of Jehovah, for the length of my days.





# Contents

<b>List of Figures</b> .....	III
<b>List of Tables</b> .....	VII
<b>1. Introduction</b> .....	1
<b>2. Theory</b> .....	5
2.1 The Electronic Properties of Condensed Matter .....	5
2.1.1 Band Structure, Density of States (DOS) and Band Gaps .....	5
2.1.2 Dipole Moment and Quadrupole Moment .....	9
2.1.3 Polarizability .....	12
2.2 The Vibrational Properties of Condensed Matter .....	13
2.2.1 Phonons and Vibrational Density of States (VDOS) .....	13
2.2.2 Principles of Raman and Infrared (IR) Spectra .....	16
2.3 The Self-Consistent Charge Density-Functional Tight-Binding (SCC-DFTB) Theory .....	19
2.3.1 The Tight-Binding (TB) Theory .....	19
2.3.2 The Density Functional Theory (DFT) .....	21
2.3.3 The SCC-DFTB Theory .....	22
2.3.4 SCC-DFTB + Dispersion Correction .....	25
2.3.5 The Derivation of Harmonic Vibrational Frequency, Raman Activity and IR Intensity in the SCC-DFTB Scheme .....	27
<b>3. Technical Details</b> .....	32
<b>4. Results and Discussion</b> .....	33
4.1 Conjugated Heterocyclic Polymer Chains .....	33
4.1.1 Evolution of Equilibrium Structures .....	38
4.1.2 Evolution of HOMO-LUMO Energy Gaps .....	45
4.1.3 Evolution of Electronic DOS Distributions .....	47
4.1.4 Evolution of Charge Distribution .....	49
4.1.5 Evolution of Dipole Moments .....	54
4.1.6 Evolution of Quadrupole Moments .....	57
4.1.7 Evolution of Polarizabilities .....	60
4.2 Raman Spectra of Nanodiamonds .....	67
4.3 Raman Spectra of Polycyclic Aromatic Hydrocarbons (PAHs) .....	78
4.4 Icosahedral Fullerenes .....	83
4.4.1 Geometrical Description of Icosahedral Fullerenes .....	83
4.4.2 Potential Energy Scan (PES) of C <sub>60</sub> @C <sub>240</sub> – Search for the Most Stable Structure .....	85
4.4.3 Signal Shielding in the Vibrational Spectra .....	89

4.4.3.1	Endohedral Fullerenes .....	89
4.4.3.2	Multi-shell Fullerenes .....	92
4.5	Raman Spectra of Single-Wall Carbon Nanotubes (SWNTs) .....	96
<b>5.</b>	<b>Conclusions</b> .....	<b>100</b>
	<b>References</b> .....	<b>103</b>



# List of Figures

<b>Figure 2.1</b>	(a) The schematic band structure of the 1D chain of hydrogen atoms with H-H distance of 1 Å. (b) The corresponding DOS. The shape of the wave function is symbolically represented by circles ..... 6	6
<b>Figure 2.2</b>	(a) The schematic band structure of the 1D chain of nitrogen atoms with N-N distance of 2 Å. And (b), the DOS of the band structure. The shapes of the wave function are iconized with circles ..... 7	7
<b>Figure 2.3</b>	The phonon dispersion curves of infinite polyynes chain calculated using the SCC-DFTB method ..... 14	14
<b>Figure 2.4</b>	Schematic representation of light scattering processes in matter .... 17	17
<b>Figure 2.5</b>	Schematic diagram of IR absorption process in matters ..... 18	18
<b>Figure 4.1</b>	Models of a) the $C_{2h}$ and b) $C_{2v}$ symmetric oligomers ..... 36	36
<b>Figure 4.2</b>	Bond length distribution comparisons between the molecular 50-mer (red line) and solid-state polymer (black line) of all the considered models in this study ..... 38	38
<b>Figure 4.3</b>	Bond length distribution convergence of the considered models in this study ..... 41	41
<b>Figure 4.4</b>	Bond length and bond angle distribution of pyrrole 50-mer. Calculated values of solid state polypyrrole are given in red solid lines ..... 42	42
<b>Figure 4.5</b>	Band gaps of all the considered models. The values shown are the extrapolated results using second-order polynomial fitting for the last forty points ..... 46	46
<b>Figure 4.6</b>	Electronic DOS distribution convergence of all the considered models. The red areas correspond to the occupied valence bands. The red area and white area are separated by the calculated Fermi level ..... 49	49

<b>Figure 4.7</b>	Induced Mulliken charges of the heteroatoms of the 50-mer in each system. The red solid lines are the corresponding solid-state values .....	51
<b>Figure 4.8</b>	Induced Mulliken charges along the $\pi$ -conjugated carbon backbone of the 50-mer in each system. Solid lines in red and blue are the solid-state values .....	52
<b>Figure 4.9</b>	The evolution of the induced charges on the nitrogen atoms in oligopyrroles. Value for polymer is given by the solid red line .....	53
<b>Figure 4.10</b>	Evolution of the dipole moments for all the considered models. Only the dipole moments of molecules with $2m+1$ unit cells ( $C_{2v}$ symmetry) are shown .....	57
<b>Figure 4.11</b>	Evolution of the quadrupole moment tensor components of all the considered models .....	59
<b>Figure 4.12</b>	Polarizability invariants of all the considered models. The blue curves are given according to the fitting formulas .....	63
<b>Figure 4.13</b>	The structures, molecular formula, and abbreviations of the tetrahedral and octahedral nanodiamonds .....	71
<b>Figure 4.14</b>	Comparison of the Raman spectra calculated by BLYP/3-31G, SCC-DFTB, and BLYP/6-31G* (A and T2 only).....	72
<b>Figure 4.15</b>	The Raman spectra evolution with respect to the size of the tetrahedral and octahedral nanodiamonds.....	73
<b>Figure 4.16</b>	The evolution of the $T_2$ peak in the Raman spectra of the three largest nanodiamonds for tetrahedral and octahedral nanodiamonds.....	74
<b>Figure 4.17</b>	The evolution of Raman spectra for both tetrahedral and octahedral nanodiamonds with “infH” case.....	75

<b>Figure 4.18</b>	The formation of the band at around $1200\text{ cm}^{-1}$ of the “infH” tetrahedral nanodiamonds .....	76
<b>Figure 4.19</b>	The formation of the band at around $1200\text{ cm}^{-1}$ of the octahedral nanodiamonds .....	77
<b>Figure 4.20</b>	The symmetries and vibration vectors of the D band and G band in Raman spectra of PAHs .....	78
<b>Figure 4.21</b>	Geometries of PAHs. Left: C3 Right: B3.....	80
<b>Figure 4.22</b>	The deformed B3 obtained by optimization along the imaginary vibration mode .....	80
<b>Figure 4.23</b>	Comparison of the SCC-DFTB and BLYP/3-21G Raman spectra of C3 and C4 .....	81
<b>Figure 4.24</b>	Evolution of Raman spectra of both graphenes and HPBs .....	82
<b>Figure 4.25</b>	The evolution of Raman spectra of “infH” graphenes and HPBs .....	83
<b>Figure 4.26</b>	Structures of the icosahedral fullerenes considered in this study .....	85
<b>Figure 4.27</b>	Angles of rotation for $C_{60}@C_{240}$ .....	86
<b>Figure 4.28</b>	The three different orientations of the benzene dimer .....	87
<b>Figure 4.29</b>	The potential energy curves of the three different benzene dimmers .....	88
<b>Figure 4.30</b>	The PES of $C_{60}@C_{240}$ using the LJ model. Energy in Hartree ..	89
<b>Figure 4.31</b>	IR spectra of the endohedral fullerenes .....	90
<b>Figure 4.32</b>	Raman spectra of the endohedral fullerenes .....	91
<b>Figure 4.33</b>	Models of all the considered multi-shell fullerenes. Except for $C_{60}@C_{240}@C_{540}$ , the color of the inner fullerenes are changed to purple for the multi-shell fullerenes .....	93

**Figure 4.34** IR spectra of multi-shell fullerenes ..... 94  
**Figure 4.35** Raman spectra of multi-shell fullerenes ..... 95  
**Figure 4.36** Model of (9,9) 5nm SWNT ..... 97  
**Figure 4.37** Raman spectra of SWNTs considered in this study ..... 98-99



# List of Tables

<b>Table 4.1</b>	Molecular formulas for all the considered $n = 1\sim 50$ molecular models of oligomers.....	36
<b>Table 4.2</b>	HOMO-LUMO gaps and the differences between the oligomers and the solid-state value.....	47
<b>Table 4.3</b>	The optimum parameters used eq. 4.3 .....	64
<b>Table 4.4</b>	Abbreviations, molecular formula, and number of atoms for Graphenes and HPBs .....	79
<b>Table 4.5</b>	List of the SWNTs considered in this study .....	96



# Chapter 1

## Introduction

In recent years, owing to the fast development in both the computer hardwares and quantum chemical theories, computational chemistry has become applicable to study larger systems and obtain more accurate results. On the other side, many new important physical observables of solid-state materials like energy band gaps and infrared (IR) and Raman vibrational spectra, can be accessed through experiment.

For theoreticians, once the energy of the system at equilibrium is computed, vast of extended properties can be directly gained by differentiating the energy with respect to different variables.<sup>1</sup> These include the HOMO-LUMO energy gaps, equilibrium structural information, charge distribution, harmonic vibrational frequencies, etc. If external perturbation is added, the Hamiltonian can be modified to include the perturbation and the properties resulting from the interaction between the molecule and the external perturbation can be calculated. There exist in general two approaches to obtain the above properties for extended systems: molecular approach and the traditional, solid-state approach. The main idea of the molecular approach is using the quantum chemical theories to obtain the properties of interest first at the molecular level. Say, for energy gaps of polymers, one can start the calculation for a monomer and extend gradually the system to longer-and-longer oligomers to obtain the calculated energy gaps as a function of the size of the system. By extrapolating this function one can get the approximate value of the energy gap of the polymer built of infinitely many monomers, which corresponds to the band gap computed within



solid-state approach. The molecular approach ignores the effects that may occur in the real solid-state matters. For example, interactions of building blocks like chain interaction in polymers or layer interaction in graphite, are neglected. Still, the molecular approach has been used extensively and gained constructive results. The second approach, the solid-state method, employs periodic nature in the crystal lattices, this can be done in the reciprocal space introduced by Fourier transformation of the real space quantities.<sup>2,3</sup>

The Self-Consistent Charge Density-Functional Tight-Binding (SCC-DFTB)<sup>4</sup> method had been born and can be applied to material science with the two approaches mentioned above. It is a semi-empirical method based on the second-order Taylor expansion of the density functional theory (DFT) energy with respect to the charge density fluctuation. Although it is a semi-empirical method, it can cope with molecules up to thousands of atoms much faster than the existing *ab initio* methods without losing much accuracy.<sup>5,6</sup> It is a good candidate to perform the calculations for systems containing up to thousands of atoms.

The principal idea of this study is to investigate the following two issues: 1. the evolution of the physical properties with growing molecular size, and 2. the transformation of physical properties from molecular stage toward solid-state stage. We have chosen as the prototypes of the conductive polymer chains, the systems of polypyrrole, polyfuran, polythiophene, trans-cisoid polyacetylene, and polycyclopentadiene. At present, our study of these polymers mainly focuses on the molecular geometrical and electronic convergence toward the infinite polymer. This has been done by examining several properties that will be discussed in Chapter 4. Besides the well-studied conductive polymers, we also have chosen several other carbon-containing materials. First of them is the nanodiamond. For this molecule, we intend to locate the signature of the solid state Raman spectra — the unique 1332

$\text{cm}^{-1}$  peak at the molecular stage. We trace the unique  $1332 \text{ cm}^{-1}$  peak. Next, for PAHs, we focus on the evolution of the Raman spectra. The character of the Raman spectra changes with different PAH size<sup>7</sup>; we are trying to relate the change to their molecular size. The main parameter here is the so-called D/G ratio in the Raman spectra, which is defined as the intensity ratio between the  $A_{1g}$  D (disorder) band and the  $E_{2g}$  G (graphite) band. The study is still under investigation. The third type of the carbon-containing systems introduced by us are the well-known fullerene cages. We have been trying to analyze two topics concerning the icosahedral fullerenes. The first issue is signal shielding in the SCC-DFTB Raman spectra of single- and multi-shell fullerenes. The signal shielding effect is discussed for the endohedral and multi-shell fullerenes. The second issue is the scan of the potential energy surface (PES) for  $C_{60}@C_{240}$ , which is meant to give a visualization of a free rotation of  $C_{60}$  inside  $C_{240}$ . The last systems being discussed are the single-wall carbon nanotubes (SWNTs). We mainly focus on their Raman spectra. Experimental first-order Raman spectra show only the strong G band for SWNTs.<sup>8</sup> For now, we only present brief reprot showing that for the armchair (5,5) SWNTs with length of 15 nm, the Raman spectra displays only the D band, which suggests that the transformation from molecular level toward the solid-state level occurs for larger tubes. Further study will pursue this issue in the future.

In chapter 1, we give a general introduction to the topics studied in this Thesis, which is followed by the extension of various theoretical aspects in chapter 2. Chapter 3 is a brief note on the programs and the parameters we have used for calculation. Chapter 4 gives the results and discussion of the application of the SCC-DFTB method on several systems, including the conductive polymers and the carbon nanostructures. Unfortunately, at this time many of the research are still far from

completion, hence in several paragraphs only concise results are shown. The conclusions of this Thesis are given in chapter 5.



# Chapter 2

## Theory

### 2.1 The Electronic Properties of Matter

In the present study, several material properties are investigated. They are generally a subject of interest in solid-state physics. Here, we give concise introduction to each of the properties studied in this Thesis.

#### 2.1.1 Band Structure, Density of States and Band Gaps

In nature, every atom possesses its own set of atomic orbitals, in which the electrons can “reside” in. For example, every hydrogen atom has one 1s orbital, and a carbon atom has one core 1s orbital and four valence orbitals (one 2s orbital and 2p<sub>x</sub>, 2p<sub>y</sub>, 2p<sub>z</sub> orbitals). When atoms come together and form a molecule, linear combinations of the atomic orbitals belonging to each atom are made to give the molecular orbitals (MO). This approach is referred to as the linear combination of atomic orbitals (LCAO) method. For the simplest hydrogen molecule, there are two MOs originating from the two 1s AO of the two hydrogen atoms. The number of thus obtained MOs will be equal to the total number of AOs in the molecule.

When the system is expanded from a molecule to a solid crystal, there will be infinitely many orbitals made from the infinitely many AOs. We consider the simplest model: a hypothetical 1D chain built of  $n$  equally spaced hydrogen atoms. The unit cell of this crystal is a single H atom. Now we call the LCAO here the crystal orbitals

(CO), rather than molecular orbitals. The lowest in energy CO will be made by summing up all the  $n$  1s orbitals with plus signs:

$$\psi_1 = \phi_1 + \phi_2 + \phi_3 + \phi_4 + \dots + \phi_n = \sum_{j=1}^n (e^{0i})^j \phi_j = \sum_{j=1}^n \phi_j, \quad (2.1)$$

which can be interpreted as bonding orbital with zero nodes. The highest in energy CO will be

$$\psi_n = -\phi_1 + \phi_2 - \phi_3 + \phi_4 - \dots + \phi_n = \sum_{j=1}^n (e^{\pi i})^j \phi_j = \sum_{j=1}^n (-1)^j \phi_j, \quad (2.2)$$

which can be interpreted as an antibonding orbital with  $n-1$  nodes. The  $m^{\text{th}}$  CO will be

$$\psi_m = e^{i \frac{(m-1)}{(n-1)} \pi} (e^1 \cdot \phi_1 + e^2 \cdot \phi_2 + e^3 \cdot \phi_3 + e^4 \cdot \phi_4 + \dots + e^n \cdot \phi_n) = \sum_{j=1}^n (e^{i \frac{(m-1)}{(n-1)} \pi})^j \phi_j \quad (2.3)$$

The exponential term  $e^{i \frac{(m-1)j}{(n-1)} \pi}$  is called the phase factor, and the coefficient of  $i$ ,  $\frac{(m-1)j}{(n-1)} \pi$ , is the so-called  $k$  vector in the reciprocal space. The  $k$  vector is characterized by periodicity, which ranges from 0 to  $\pi$  in this case.

The mathematics behind this formalism is the Fourier transform. A periodic function  $f(x)$  which satisfies the condition:  $f(x) = f(x+a)$ , where  $a$  is the periodicity of function  $f$ , can be expanded into a Fourier series. By using Euler's formula

$$e^{inx} = \cos(nx) + i \sin(nx), \text{ we obtain } f(x) = \sum_{n=-\infty}^{n=\infty} c_n e^{inx}, \text{ where } c_n \text{ is the Fourier}$$

coefficient. Because the crystal lattice has the periodicity of the lattice translation vectors, the electron motion is also periodic in the lattice, hence can be expanded in a Fourier series. If we now plot the energies of different sets of CO corresponding to different values of  $k$ , we obtain the diagram called "band structure". The band structure of the 1D hydrogen atom chain is shown in figure 1<sup>9</sup>. Because the unit cell contains only one hydrogen atom, and thus only one 1s orbital per unit cell, the only curve in the band structure corresponds to this orbital. In practice, the systems under studied are usually 3D and contains more than one atom in the unit cell. Hence the band structure looks much more complicated. To extract the relevant information

from such complicated 3D band structures, people found out a way of doing this by means of the density of states (DOS). The DOS is defined as the number of one electron levels in a small energy interval, or mathematically in the 1D case:

$$D(E) \sim \left( \frac{dk}{dE} \right) \quad (2.4)$$

The DOS is a function of band energy  $E$ , and it is the inverse slope of the band being considered. That is, the flatter the band, the steeper the corresponding DOS. A very sharp DOS results from an extremely flat, atomic-like band, one that arises from an atomic orbital that does not overlap significantly with neighboring orbitals. Electrons occupied in such a band can not easily move through the crystal and they are slow. On the other hand, a wide DOS indicates rapidly moving electrons due to strong interatomic coupling.

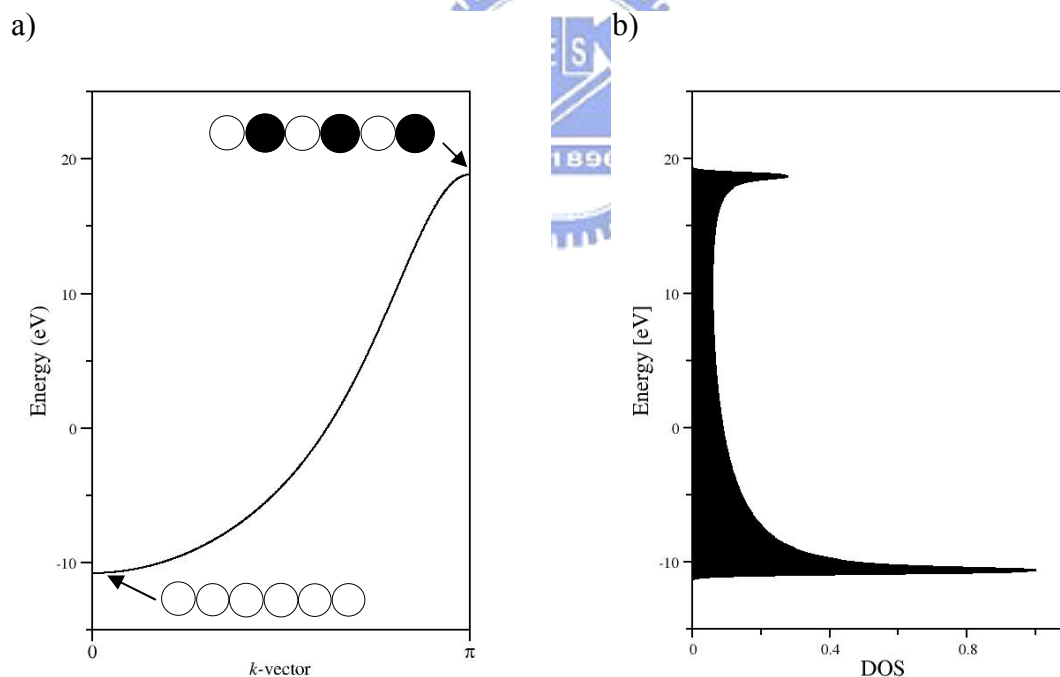


**Figure 2.1** (a) The schematic band structure of the 1D chain of hydrogen atoms with H-H distance of 1 Å. (b) The corresponding DOS. The shape of the wave function is symbolically represented by circles.

If now we turn to another 1D atomic chain, substituting hydrogen to nitrogen, then

we will have four AOs per nitrogen atom in one unit cell. The resulting band structure, as we can see, contains four valence bands. Note that the  $2p_x$  and  $2p_y$  bands are degenerate in the plot. Note that the partial DOSs come from the three 2p orbitals superpose together in the DOS diagram.

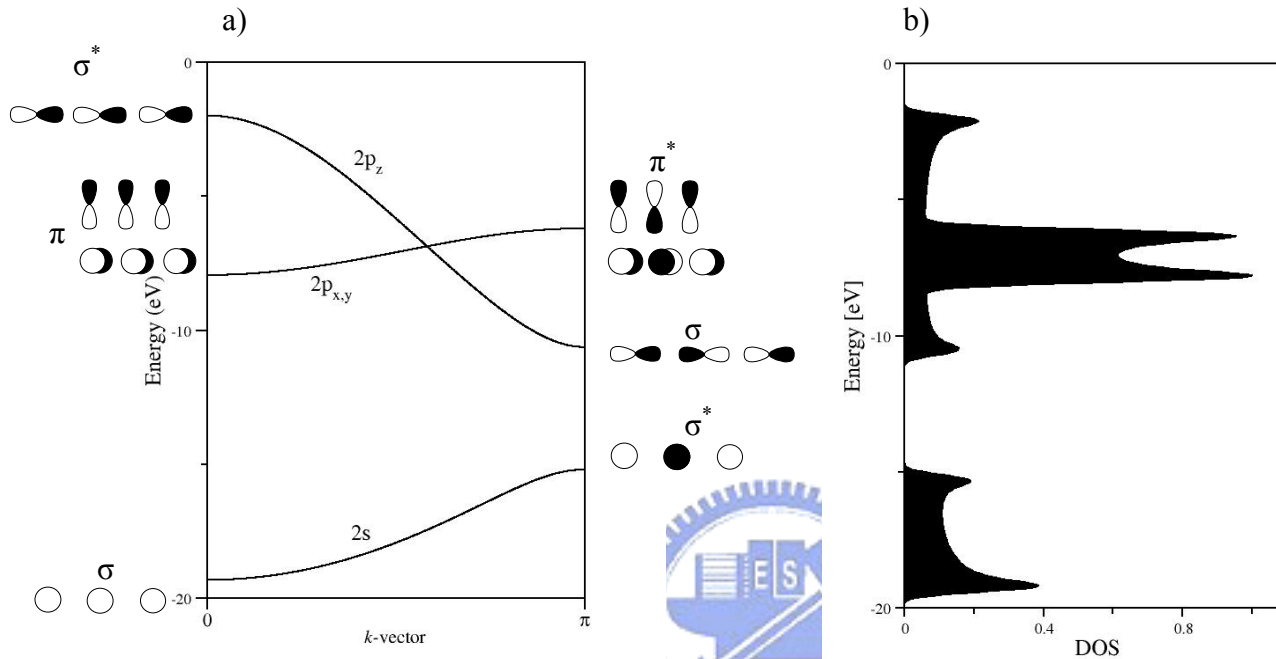


**Figure 2.2** (a) The schematic band structure of the 1D chain of nitrogen atoms with N-N distance of 2 Å. And (b), the DOS of the band structure. The shapes of the wave function are iconized with circles.

The electrons fill the bands in the same way as they fill the molecular orbitals. The bands are filled according to their energy order, for example, for the 1D atomic chain of nitrogen, the 2s band will be filled by the 2s electrons from each nitrogen atom, and the 2p electrons occupy the 2p bands. The bands filled with electrons are called *valence bands*, and the empty bands are called *conduction bands*. Note that the valence bands may be only partially filled. Electrons may be excited from the valence band to the conduction band through thermal energy or an external electric field, which results in electric current. The *Fermi-Dirac distribution*  $f(E)$  gives the probability that an orbital of energy  $E$  will be occupied in an ideal electron gas<sup>2</sup>:

$$f(E) = \frac{1}{1 + \exp\left[\frac{(E - E_F)}{kT}\right]} \quad (2.5)$$

In the formula,  $k$  is the Boltzmann constant, and  $T$  is the temperature in Kelvins. The *Fermi level*  $E_F$  is defined as the energy of the topmost filled orbital at absolute zero ( $T=0$ ). The difference in energy between the top of the highest valence band and the bottom of the lowest conduction band is the so-called *band gap*. The band gap for solids is corresponding to HOMO-LUMO energy gap for molecules. It is an index of the electrical conductivity of materials and can be used to classify the insulators, semi-conductors, and conductors. In a qualitative perspective, the insulators can be thought as solids with large band gap between the completely filled valence band and the conduction band, and these two bands do not cross at any  $k$  point. The semi-conductors are insulators with relatively small band gap (say less than 3 eV)<sup>10</sup>, thus the electrons can be excited to conduction band by thermal energy. Metals have the highest valence band partially filled, thus no energy gap exists.

### 2.1.2 Dipole Moment and Quadrupole Moment

The dipole and quadrupole moments describe the properties of the charge distributions inside a molecule. In the classical point of view, atoms or molecules can be regarded as an assembly of point charges with definite positions in space. In quantum mechanical picture, the definite description of the positions of charges are replaced by the probability distributions in space. Summations over discrete charges are also substituted by integrals over charge distribution probability corresponding to the square of the wave function.

Here we start at the classical level, to see that the molecular charge distribution can be decomposed into a hierarchy of electric moments (monopole, dipole, quadrupole, etc.).<sup>11</sup> Consider a collection of discrete charges  $\{q_i\}$  located at



distances  $\{r_i\}$  from an arbitrary origin. The resulting potential at some point  $\bar{R}$  is given by

$$V(\bar{R}) = \frac{1}{4\pi\epsilon_0} \sum_i \frac{q_i}{|\bar{R} - \bar{r}_i|}, \quad (2.6)$$

where  $\epsilon_0$  is the vacuum permittivity and  $\frac{1}{4\pi\epsilon_0}$  is the Coulomb's constant. For the

condition  $R \gg r_i$ ,  $\frac{1}{|\bar{R} - \bar{r}_i|}$  can be expanded using the Taylor expansion:

$$\frac{1}{|\bar{R} - \bar{r}_i|} = \frac{1}{R} - \bar{r}_i \cdot \nabla \left( \frac{1}{R} \right) + \frac{1}{2} \bar{r}_i \bar{r}_i : \nabla \nabla \left( \frac{1}{R} \right) + \dots \quad (2.7)$$

Here the single and double dots represent tensor contractions. The potential  $V$  is then

$$4\pi\epsilon_0 V(\bar{R}) = \frac{q}{R} - \bar{\mu} \cdot \nabla \left( \frac{1}{R} \right) + \frac{1}{2} \Theta : \nabla \nabla \left( \frac{1}{R} \right) + \dots \quad (2.8)$$

The above equation introduces a hierarchy of multipole moments: the charge  $q$  (monopole), dipole moment  $\bar{\mu}$ , quadrupole moment  $\Theta$ , etc. There are still higher order terms, like octupole, hexadecapole, etc., moments. The first three multipole moments are defined as:

$$\begin{aligned} q &= \sum_i q_i = \int \rho(\bar{r}) d\bar{r} \\ \bar{\mu} &= \sum_i q_i \bar{r}_i = \int \bar{r} \rho(\bar{r}) d\bar{r} \quad , \\ \Theta &= \sum_i q_i \bar{r}_i \bar{r}_i = \int \bar{r} \bar{r} \rho(\bar{r}) d\bar{r} \end{aligned} \quad (2.9)$$

with  $\rho(\bar{r})$  being the charge density.

Note that the charge is a scalar, the dipole moment is a vector, and the quadrupole moment is a tensor. The definitions express the multipole moments either as summations of discrete charges or integrals over continuous charge density. Usually the dipole moment has the unit of Debye.  $1D = 3.336 \times 10^{-30} \text{ C} \cdot \text{m}$ . The quadrupole moment is a symmetric square matrix with totally nine components. But only six of

them are independent due to symmetry relations. That is,  $\Theta_{ij} = \Theta_{ji}$ , where  $i$  and  $j$  can be  $x, y$  or  $z$ . Usually the quadrupole tensor is chosen to be traceless, which means that the sum of the diagonal terms is zero. The traceless  $\Theta$  is defined as

$$\Theta = \frac{1}{2} \sum_i q_i (3\bar{r}_i \bar{r}_i - \bar{r}_i^2 \mathbf{I}), \quad (2.10)$$

where  $\mathbf{I}$  is the unit matrix, with diagonal elements equal to one.

The multipole moments introduced above can be used to describe the interaction of electromagnetic field with matter. For example, the energy of a collection of charges subjected to an external field is given by

$$W = qV - \bar{\mu} \cdot \bar{E} - \frac{1}{3} \Theta : \nabla \bar{E} + \dots \quad (2.11)$$

Here we use  $W$  to denote energy, to avoid the confusion with the electric field  $\bar{E}$ . The picture here is that the total charge  $q$  interacts with the potential, the dipole moment interacts with the field, and the quadrupole moment interacts with the field gradient. They contribute additional energy to the total energy in the presence of the electric field.

In the SCC-DFTB framework (which will be introduced later), the Mulliken charge is used to describe the charge  $q$ . The electron density  $\rho(\vec{r})$  at certain position  $\vec{r}$  within a molecule is defined as the square of the MO.<sup>1</sup>

$$\rho(\vec{r}) = \psi(\vec{r})^2 \quad (2.12)$$

The  $i$ th MO in a molecule can be expanded in the LCAO form as described in the previous section,

$$\psi_i = \sum_{\alpha} c_{i\alpha} \phi_{\alpha} \quad (2.13)$$

, where  $c_{i\alpha}$  is the coefficient for the AO  $\phi_{\alpha}$ . The square of the MO is then

$$\psi_i^2 = \sum_{\alpha\beta} c_{i\alpha} c_{i\beta} \phi_{\alpha} \phi_{\beta}. \quad (2.14)$$

We introduce the occupation number (number of electrons),  $n$ , for each MO. Then the total number of electrons  $N$  in a molecule can be given by

$$N = \sum_i^{MO} n_i \int \psi_i^2 d\mathbf{r} = \sum_{\alpha\beta}^{AO} \sum_i^{MO} n_i c_{i\alpha} c_{i\beta} \phi_\alpha \phi_\beta = \sum_{\alpha\beta}^{AO} \sum_i^{MO} n_i c_{i\alpha} c_{i\beta} S_{\alpha\beta} = \sum_{\alpha\beta}^{AO} D_{\alpha\beta} S_{\alpha\beta} \quad (2.15)$$

, where  $S$  is defined as the overlap matrix of AOs and  $D$  is the density matrix given by summing up the multiplications the occupation numbers and the AO coefficients.

In computational chemistry, the Mulliken population analysis based on the  $DS$  matrix is used for distributing the electrons into the atomic contributions.

The contributions from all AOs located on a given atom A may be summed up to give the number of electrons associated with atom A. In the Mulliken scheme, the contribution involving basis functions on different atoms is divided equally between the two atoms. The Mulliken electron population is thereby defined as

$$\rho_A = \sum_{\alpha \in A}^{AO} \sum_{\beta}^{AO} D_{\alpha\beta} S_{\alpha\beta} \quad (2.16)$$

The gross charge on atom A is the sum of the nuclear and electronic contributions.

$$q_A = Z_A - \rho_A \quad (2.17)$$

Here  $Z_A$  is the number of positive charge that the nucleus owns.

### 2.1.3 Polarizability

In the presence of the external electric field, the molecular charge distribution may be distorted and leads to modified multiple moments.<sup>11</sup> Using the Taylor expansion, the previously discussed electric dipole moment  $\mu$  can be expanded in a power series in the applied field:

$$\bar{\mu} = \bar{\mu}_0 + \alpha \cdot \bar{E} + \beta : \bar{E}\bar{E} + \dots, \quad (2.18)$$

where  $\bar{\mu}_0$  is the permanent dipole moment, i.e., the dipole moment in the absence of the external field.  $\alpha$  is the linear response of the dipole moment to the applied field, called polarizability. And  $\beta$  is the hyperpolarizability, which describes the leading contribution to the nonlinear response of the dipole in the applied field. The

polarizability is in fact a tensor with nine components:

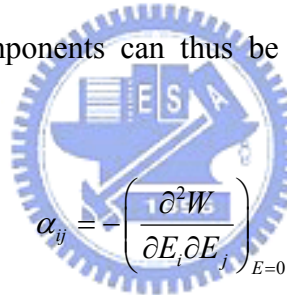
$$\alpha = \begin{bmatrix} \alpha_{xx} & \alpha_{xy} & \alpha_{xz} \\ \alpha_{yx} & \alpha_{yy} & \alpha_{yz} \\ \alpha_{zx} & \alpha_{zy} & \alpha_{zz} \end{bmatrix}. \quad (2.19)$$

The polarizability tensor is symmetric, hence only six tensor components are needed to specify the whole tensor. Physically, it is a measure of the easiness that the larger magnitude of the dipole moment can be induced by an external field, or in other words, it is the ratio of the induced dipole and the external electric field.

The total energy of the system can also be expanded using the power series of the electric field.

$$W = W_0 - \bar{\mu}_0 \cdot \bar{E} - \frac{1}{2} \bar{E} \cdot \alpha \cdot \bar{E} \quad (2.20)$$

The polarizability tensor components can thus be expressed in terms of the total energy:



$$\alpha_{ij} = - \left( \frac{\partial^2 W}{\partial E_i \partial E_j} \right)_{E=0} \quad (2.21)$$

In the case of our SCC-DFTB calculations, the derivative in the equation above is computed numerically.

## 2.2 The Vibrational Properties of Matter

### 2.2.1 Phonon Dispersion Relations and Vibrational Density of States (VDOS)

In crystals, the energy of a lattice vibration is quantized. The quantum of energy is called phonon, similar to photon for light. The relationship of phonon and lattice vibration is in analogy with photon and light.

Consider an ideal crystal consisting of  $M$  diatomic unit cells (note that in reality

the number of unit cells should be infinitely many). The total number of vibrational modes for a single unit cell is  $3 \times 2 = 6$ , because every atom in the unit cell has 3 degrees of freedom. The resulting phonon structure will contain six bands. In accord with the band structure plot, in the phonon dispersion plot, the vertical axis gives the vibrational frequency of the vibrational modes, and the horizontal axis correspond to the  $k$ -points used in the Fourier transform. For instance, at  $k=0$ , the crystal vibration of the first phonon band (lowest in energy)  $D_{1,k=0}$  is formed by summation of the vibrational modes in each unit cell lowest in energy with plus signs over all the  $M$  lattices.

$$D_{1,k=0} = Q_{11} + Q_{12} + Q_{13} + \dots = \sum_{l=1}^M e^{(0i)l} Q_{1l} = \sum_{l=1}^M (1)^l Q_{1l} \quad (2.22)$$

The  $Q_{1l}$  denotes the vibrational normal mode lowest in energy of the  $l$ th unit cell. The crystal vibration of the second phonon band at  $k=0$  is given by

$$D_{2,k=0} = Q_{21} + Q_{22} + Q_{23} + \dots = \sum_{l=1}^M e^{(0i)l} Q_{2l} = \sum_{l=1}^M (1)^l Q_{2l} \quad (2.23)$$

Here  $Q_{2l}$  corresponds to the second lowest in energy vibrational normal mode of the  $l$ th unit cell. The rest four bands have the same formalism. If at  $k = \pi$ , the vibraional mode of the whole crystal is given by

$$D_{1,k=\pi} = -Q_{11} + Q_{12} - Q_{13} + \dots = \sum_{l=1}^M e^{(i\pi)l} Q_{1l} = \sum_{l=1}^M (-1)^l Q_{1l} \quad (2.24)$$

In general, the crystal vibration mode of the  $j$ th phonon band at an arbitrary  $k$  point is composed of the linear combination of the unit cell normal modes as

$$D_{j,k} = \sum_{l=1}^M e^{i\left(\frac{l-1}{M-1}\right)\pi} Q_{jl} = \sum_{l=1}^M e^{ik\pi} Q_{jl}, \quad (2.25)$$

given  $k$  the phase factor and also it is the wave vector in solid state physics, which is defined as

$$k = \frac{2\pi}{\lambda}, \quad (2.26)$$

with  $\lambda$  the wavelength of the incident radiation.

The phonon branches can be classified as longitudinal or transversal according to

the vibration spatial characteristics. These two types of phonons can be divided further into the so called *optical* or *acoustic* modes. The optical phonon branches are named “optical” because in the ionic crystals, these types of modes are easily excited by radiation, and in the vibration the positive and negative ions at adjacent lattice sites swing against each other, creating a time-varying electrical dipole moment. The atoms in the acoustic mode vibrate in the way similar to acoustic waves, that all the atoms or (ions) vibrate in phase. The acoustic modes have zero frequency at  $k=0$ , because they are in fact the translations when all the unit cells move in the same direction.

An example of the phonon dispersion curve is shown in Figure 2.3. This is the phonon dispersion curves of the infinite polyyne chain containing two carbon atoms per unit cell. There are six phonon bands, but two bands are degenerated, which results in only four visible curves in the plot. The LO denotes the longitudinal optical mode and LA, the longitudinal acoustic mode. Analogous transversal phonons are denoted as TO and TA. The symbols  $\Gamma$  and X at the  $k$ -vector axis are the special points of high symmetry in the Brillouin zone.

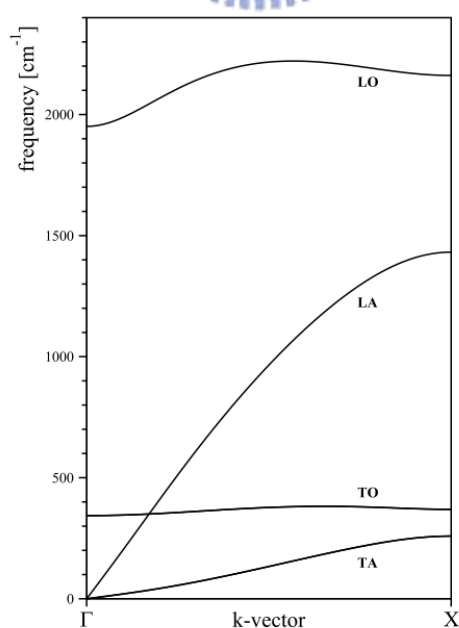


**Figure 2.3** The phonon dispersion curves of infinite polyyne chain calculated using the SCC-DFTB method.

The VDOS is defined analogously like the DOS in band structure theory. The VDOS is given by

$$d(\omega) = \frac{\partial k}{\partial \omega}, \quad (2.27)$$

with  $\omega$  the vibrational frequency.

In the SCC-DFTB VDOS calculation, we take the molecular harmonic vibrational frequencies, smear them along the  $k$ -axis with a Gaussian function, and then superpose these Gaussian functions to make the usual VDOS.

### 2.2.2 Principles of Raman and Infrared (IR) Spectra

Under the radiation of the infrared light, molecules may be excited into their vibrational excited states. There are several phenomena can be observed during the radiation. Among them, the light absorption and emission is responsible for the IR spectrum, and light scattering for the Raman spectrum. A simple description of these two processes is given below.



#### Light Scattering

In the light scattering, the incident light, or photon, is not absorbed by molecules, but instead, the scattering occurs. As shown in the diagram below, there are three types of scattering. They are Rayleigh scattering, Stokes shift, and anti-stokes shift. Only Rayleigh scattering is elastic, i.e., the photon keeps its initial energy  $h\nu_0$  after being scattered by the molecule. In the second case, the incident photon losses certain amount of energy, which corresponds to one quantum of vibrational energy equal to vibrational level difference  $h\nu_v$  of the molecule. Hence the emitted radiation will give a signal at the lower energy side with respect to the Rayleigh line in the Raman spectrum. This is the Stokes shift. In the third case, a photon gains more energy after scattering, hence the signal appears at the higher-energy side relative to the Rayleigh

line and is called anti-Stokes shift. The later two cases are inelastic processes and are called Raman scattering.

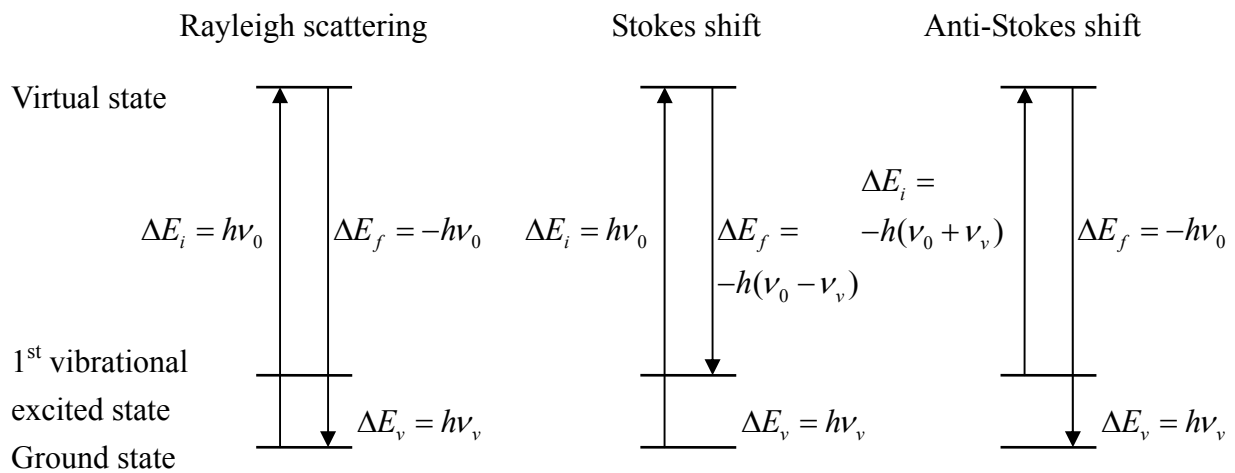


**Figure 2.4** Schematic representation of light scattering processes in matter.

Noteworthy, these processes are not step-wise, but, the light absorption and emission take place simultaneously.

Quantum chemically, the Raman scattering intensity is evaluated by applying the Kramers-Heisenberg-Dirac (KHD) dispersion formula<sup>12</sup>. Based on the KHD formula, we assume that the difference between the vibrational energy levels and the virtual state is much greater than the incident photon energy, that is, the off-resonance condition. The Raman scattering tensor  $a_{\rho\sigma}$  can then be approximated by

$$a_{\rho\sigma} = \langle \nu'' | \alpha_{\rho\sigma} | \nu' \rangle, \quad (2.28)$$

with  $\alpha_{\rho\sigma}$  the polarizability tensor and  $\nu'', \nu'$  the vibrational parts of the final state wave function and initial state wave function. This is the so-called *Placzek's approximation*. We can further expand the polarizability tensor into a power series of normal coordinates about the equilibrium molecular geometry:



$$\alpha_{\rho\sigma} = \alpha_{\rho\sigma}^0 + \sum_j \left( \frac{\partial \alpha_{\rho\sigma}}{\partial Q_j} \right)_0 Q_j + \dots \quad (2.29)$$

Substituting eq. (2.29) into eq. (2.28), we have

$$a_{\rho\sigma} = \sum_j \left( \frac{\partial \alpha_{\rho\sigma}}{\partial Q_j} \right)_0 (\nu'' | Q_j | \nu') \quad (2.30)$$

And the resulting selection rules are:

$\Delta\nu = \pm 1$  (the plus sign + for Stokes shift, the minus sign - for anti-Stokes shift)

$$\left( \frac{\partial \alpha_{\rho\sigma}}{\partial Q_j} \right)_0 \neq 0 \quad (2.31)$$

In the SCC-DFTB Raman spectra calculations, we adapt the off-resonance conditions and the Placzek's approximation is made.

### Light absorption

IR vibrational spectrum occurs when molecules absorb infrared light, to be excited into vibrational excited states (absorption spectrum), or emit a light with same energy (emission spectrum).

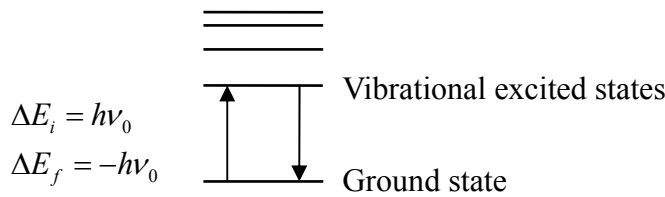


**Figure 2.5** Schematic diagram of IR absorption process in matters.

The IR intensity is related to the transition moment  $\langle f | \mu | i \rangle$  and it is given under the Born-Oppenheimer approximation and the dipole approximation, by

$$\langle f | \mu | i \rangle \approx \left( \frac{\partial \mu_e}{\partial Q_j} \right)_0 (\nu'' | Q_j | \nu') \quad (2.32)$$

It is proportional to the derivative of the dipole moment derivatives with respect to a

normal coordinate, and to the matrix element  $\langle \nu'' | Q_j | \nu' \rangle$ . Under the harmonic approximation, the selection rules for IR spectrum are given by:

$$\Delta \nu = 1$$

$$\left( \frac{\partial \mu_e}{\partial Q_j} \right) \neq 0 \quad (2.33)$$

## 2.3 The SCC-DFTB Method

### 2.3.1 The Tight-Binding (TB) Theory

The electronic properties of solids play crucial roles in the development of novel materials. Especially in semiconductor industry, the electronic properties like band gap decide whether a composite is insulating, semi-conductive, or conductive. To well describe these properties theoretically, several important theories have been developed in the past decades. One among these theories is the tight-binding (TB) theory. The introductory description of this theory is given below.

In the TB theory,<sup>9</sup> under the presumption that the electron conduction in a material is not significant, the atoms are assumed to be neutral free atoms, so that the electrons belonging to these atoms are regarded as “tightly bound ” to them. The atomic wave function under this condition should be very close to the original atomic wave functions. Thus the wave function of the electrons in the crystal can be approximated as a linear combination of atomic orbitals (LCAO) in the Bloch form:

$$\psi_j(k, r) = \sum_T e^{ikT} \sum_A \sum_{\substack{\mu=1 \\ \mu \in A}}^n c_{\mu j}(k) \phi_\mu(r-T), \quad (2.34)$$

where T denotes the translation vector in the real space. This equation indicates that the wave function is formed in the periodic reciprocal lattice space. This is an analog

of the usual molecular LCAO method, where one uses linear combination of atomic orbitals to describe the electron motions in molecules, except that the TB method is  $k$ -dependent and being used in solid state calculations.

The TB theory uses several important simplifications speeding up the computations. First, it treats only the valence electrons, and the basis sets used in the expansion of the atomic orbitals are minimal basis sets, i.e. for carbon atom, only four functions are needed:  $2s$ ,  $2p_x$ ,  $2p_y$ , and  $2p_z$  to describe the four valence electrons.

The total energy expression in TB theory<sup>13</sup> is assumed to be in the following form:

$$E = \sum_{i=1}^n \varepsilon_i + \sum_{\alpha} \sum_{\beta \neq \alpha} U(|R_{\alpha} - R_{\beta}|) \quad (2.35)$$

The  $\varepsilon_i$ 's are the eigenvalues of some effective one-particle Hamiltonian  $\hat{H}$ ,

$$\hat{H}\psi_i(r) = \left[ -\frac{1}{2}\nabla^2 + V(r) \right] \psi_i(r) = \varepsilon_i \psi_i(r) \quad (2.36)$$

, and  $U(|R_{\alpha} - R_{\beta}|)$  is a short-ranged pairwise repulsion between two atoms placed at  $R_{\alpha}$  and  $R_{\beta}$ , respectively. This equation is solved variationally within a basis of localized atomic-like functions,  $\{\phi_{\alpha}\}$ , which leads to a secular equation

$$|\mathbf{H} - \varepsilon \mathbf{S}| = 0 \quad (2.37)$$

where  $\mathbf{H}_{\alpha\beta} = \langle \phi_{\alpha} | \hat{\mathbf{H}} | \phi_{\beta} \rangle$  is the Hamiltonian matrix and  $\mathbf{S}_{\alpha\beta} = \langle \phi_{\alpha} | \phi_{\beta} \rangle$  is the overlap matrix.

SCC-DFTB treats the matrix elements in the framework of the two-center parametrization introduced by Slater and Koster.<sup>14</sup> There are at least four functions ( $ss\sigma$ ,  $sp\sigma$ ,  $pp\sigma$ ,  $pp\pi$ ) of inter-atomic distance to fit for a  $sp$  bonded solid and at least ten ( $ss\sigma$ ,  $sp\sigma$ ,  $sd\sigma$ ,  $pp\sigma$ ,  $pp\pi$ ,  $pd\sigma$ ,  $pd\pi$ ,  $dd\sigma$ ,  $dd\pi$ ,  $dd\delta$ ) for a solid with  $s$ ,  $p$ , and  $d$  electrons.

### 2.3.2 The Density Functional Theory (DFT)

Before we give an outlook of the SCC-DFTB theory, we first quickly density functional theory (DFT). Hohenberg and Kohn stated<sup>15</sup> that the ground state electron density determines the total energy of a system:

$$E_0 = E[\rho_0(\mathbf{r})] \quad (2.38)$$

They also proved the existence of an universal functional that connects the density and energy of a many-electron system :

$$F_{HK}[\rho] = T[\rho] + V_{ee}[\rho], \quad (2.39)!!!$$

where  $T[\rho]$  is the functional of kinetic energy and  $V_{ee}[\rho]$  of electron-electron interaction. The total energy expression as the functional of the electron density is given by

$$E[\rho(\mathbf{r})] = F[\rho] + \int v_{ext}(\mathbf{r})\rho(\mathbf{r})d\mathbf{r} = T[\rho] + V_{ee}[\rho] + V_{ext}[\rho] \quad (2.40)$$

Kohn and Sham further introduced orbitals into DFT to let the kinetic energy be calculated in a simple fashion. This can be achieved by the one-particle wave functions  $\psi_i(r)$  and the occupation numbers  $n_i$ . Their method is first for the N non-interacting electrons. The ground state kinetic energy is then written as

$$F[\rho] = T_s[\rho] = \sum_{i=1}^N n_i \langle \psi_i(\mathbf{r}) | \hat{t} | \psi_i(\mathbf{r}) \rangle = \sum_{i=1}^N n_i \langle \psi_i(\mathbf{r}) | -\frac{\Delta}{2} | \psi_i(\mathbf{r}) \rangle \quad (2.41)$$

The equation above is only true for non-interacting particles, which is no more validated for interacting particles. To take the particle interaction into account, they suggest expand the universal functional in the following way:

$$F[\rho] = T_s[\rho] + J[\rho] + E_{xc}[\rho] \quad (2.42)$$

Here in addition to the kinetic term  $T_s[\rho]$ , the Coulomb interaction functional

$$J[\rho] = \frac{1}{2} \iint \frac{\rho(\mathbf{r})\rho(\mathbf{r}')}{|\mathbf{r} - \mathbf{r}'|} d\mathbf{r}d\mathbf{r}' \quad (2.43)$$

and the exchange-correlation energy functional  $E_{xc}[\rho]$  are also included.

$E_{xc}[\rho]$  is defined as the difference between the exact functional and  $T_s[\rho]$  plus  $J[\rho]$ :

$$E_{xc}[\rho] = F_{HK} - T_s[\rho] - J[\rho] \quad (2.44)$$

The expression of the total energy is now given by:

$$\begin{aligned} E[\rho(\mathbf{r})] &= F[\rho] + \int v_{ext}(\mathbf{r})\rho(\mathbf{r})d\mathbf{r} \\ &= \sum_i^N n_i \langle \psi_i | -\frac{\Delta}{2} | \psi_i \rangle + \frac{1}{2} \iint \frac{\rho(\mathbf{r})\rho(\mathbf{r}')}{|\mathbf{r}-\mathbf{r}'|} d\mathbf{r}d\mathbf{r}' + E_{xc}[\rho] + \int v_{ext}(\mathbf{r})\rho(\mathbf{r})d\mathbf{r} \end{aligned} \quad (2.45)$$

By applying the variational principle to the energy expression above, the so-called Kohn-Sham equations are introduced, with the effective one-particle Hamiltonian operator  $\hat{H}$  and the energies  $\varepsilon_i$ . This is actually a one-particle eigenvalue problem of the form:

$$\hat{H}|\psi_i\rangle = \varepsilon_i|\psi_i\rangle \quad i = 1, \dots, N \quad (2.46)$$

$$\hat{H} = -\frac{\Delta}{2} + v_{ext} + \int \frac{\rho(\mathbf{r}')}{|\mathbf{r}-\mathbf{r}'|} d\mathbf{r}' + v_{xc}[\rho] \quad (2.47)$$

The exchange-correlation potential is a functional derivative of  $E_{xc}$ :

$$v_{xc}[\rho] = \frac{\delta E_{xc}[\rho]}{\delta \rho} \quad (2.48)$$

The KS equation is solved in a self-consistent manner.

Finally the DFT total energy reads:

$$E[\rho(\mathbf{r})] = \sum_i^N n_i \varepsilon_i - \frac{1}{2} \iint \frac{\rho(\mathbf{r})\rho(\mathbf{r}')}{|\mathbf{r}-\mathbf{r}'|} d\mathbf{r}d\mathbf{r}' - \int v_{xc}[\rho]\rho(r) + E_{xc}[\rho] \quad (2.49)$$

### 2.3.3 The SCC-DFTB Theory

The SCC-DFTB theory<sup>4</sup> can be regarded as a semi-empirical approximation of DFT. Foulkes and Haydock<sup>6,9</sup> showed that it can be regarded as a second order expansion of the DFT energy at the reference density  $\rho_0(r)$  with respect to the density fluctuations  $\delta\rho$ . By including the Taylor-expanded exchange-correlation functional  $E_{xc}$  and the nuclear-nuclear interaction, the resulting energy reads:

$$\begin{aligned}
E_{tot} = & \sum_i^{occ} n_i \langle \psi_i | -\frac{\Delta}{2} + v_{ext} + \int \frac{\rho_0(\mathbf{r}')}{|\mathbf{r}-\mathbf{r}'|} d\mathbf{r}' + v_{xc}[\rho_0(\mathbf{r})] | \psi_i \rangle \\
& - \frac{1}{2} \iint \frac{\rho_0(\mathbf{r}')\rho_0(\mathbf{r})}{|\mathbf{r}-\mathbf{r}'|} d\mathbf{r}d\mathbf{r}' - \int v_{xc}[\rho_0(\mathbf{r})]\rho_0(\mathbf{r})d\mathbf{r} + E_{xc}[\rho_0] + E_{NN} \quad (2.50) \\
& + \frac{1}{2} \iint \left[ \frac{1}{|\mathbf{r}-\mathbf{r}'|} + \left( \frac{\delta^2 E_{xc}[\rho]}{\delta\rho(\mathbf{r})\delta\rho(\mathbf{r}')} \right)_{n=n_0} \right] \delta\rho(\mathbf{r})\delta\rho(\mathbf{r}')d\mathbf{r}d\mathbf{r}'
\end{aligned}$$

This expression can be resolved into three parts, the first one is the Hamiltonian matrix with operator  $\widehat{H}_0$ . The second is the second line, which accounts for the repulsive interaction. The third one is the second order term depending on the density fluctuation.

Hence the terms can be further transformed into the following:

$$E_{tot} = \sum_i^{occ} n_i \langle \psi_i | \widehat{H}_0[\rho_0(\mathbf{r})] | \psi_i \rangle + E_{rep}[\rho_0(\mathbf{r})] + E_{2nd} \quad (2.51)$$

If we neglect the second order contribution  $E_{2nd}$ , then the  $E_{tot}$  is the non-SCC DFTB energy. The repulsive energy can be approximated as a summation of pairwise, short-ranged potentials  $U(|\mathbf{R}-\mathbf{R}'|)^{16}$ , so that

$$E_{rep} = \frac{1}{2} \sum_{A,B \neq A}^M U(|\mathbf{R}_A - \mathbf{R}_B|) \quad (2.52)$$

The repulsive energy is a function of the inter-atomic distance, and can be derived from the difference of the total energy of a self-consistent DFT calculation and the band structure energy in a range of inter-atomic pair distances  $|\mathbf{R}_A - \mathbf{R}_B|$

$$E_{rep} = E_{tot}^{KS}(|\mathbf{R}_A - \mathbf{R}_B|) - E_{BS}(|\mathbf{R}_A - \mathbf{R}_B|) - E_{2nd}(|\mathbf{R}_A - \mathbf{R}_B|) \quad (2.53)$$

As in TB theory, the molecular orbitals in the DFTB method are expanded using LCAO method. The atomic orbitals are using the confined Slater-type functions.

Hence the Hamiltonian matrix elements read:

$$\langle \psi_i | \widehat{H}_0[\rho_0(\mathbf{r})] | \psi_i \rangle = \sum_{\alpha,\beta} c_{i\alpha}^* c_{i\beta} \langle \phi_\alpha | \widehat{H}_0[\rho_0(\mathbf{r})] | \phi_\beta \rangle = \sum_{\alpha,\beta} c_{i\alpha}^* c_{i\beta} H_{\alpha\beta}^0[\rho_0(\mathbf{r})] \quad (2.54)$$

Interactions between a chosen atom and other atoms other than the nearest ones are neglected, the two center approximation is made. Therefore the Hamiltonian matrix elements can be classified as:

$$H_{\alpha\beta}^0 = \begin{cases} \mathcal{E}_\alpha^{\text{free atom}} & \text{if } \alpha=\beta \\ \langle \phi_\alpha^A | \hat{t} + \hat{V}[\rho_0^A(\mathbf{r}) + \rho_0^B(\mathbf{r})] | \phi_\beta^B \rangle & \text{if } \alpha \neq \beta, A(\alpha) \neq B(\beta) \\ 0 & \text{otherwise.} \end{cases} \quad (2.55)$$

The matrix elements  $H_{\alpha\beta}^0$  as well as the overlap matrix  $S_{\alpha\beta} = \langle \phi_\alpha | \phi_\beta \rangle$  are needed to be calculated only once, and tabulated for a range of inter-atomic distances for future calculations.

While dealing with systems displaying charge transfer between atoms, the previously omitted second-order charge density fluctuation correction should be included in the total energy. This forms the final frame of SCC-DFTB. The density fluctuation can be expanded in a series of radial and angular functions centering on each atom, and decay fast with increasing distance from the corresponding centered. The expansion is truncated after the monopole term, and the coefficient is recognized as the fluctuation of the Mulliken charges.

$$\delta\rho^A(\mathbf{r}) = \sum_{lm} c_{lm}^A F_{lm}^A Y_{lm}^A \approx \Delta q^A F_{00}^A Y_{00}^A \quad (2.56)$$

The Mulliken charge and the charge fluctuation are:

$$q^A = \sum_i^{occ} n_i \sum_\alpha \sum_\beta c_{i\alpha} c_{i\beta} S_{\alpha\beta} \quad (2.57)$$

$$\Delta q^A = q^A - q_0^A \quad (2.58)$$

where  $q_0^A$  stands for the number of valence electrons of a neutral atom  $A$ .

Hence the second-order correction  $E_{2nd}$  can be expressed as

$$E_{2nd} = \frac{1}{2} \sum_A^M \sum_B^M \gamma_{AB}(\mathbf{R}_{AB}) \Delta q_A \Delta q_B \quad (2.59)$$

, and

$$\gamma_{AB}(\mathbf{R}_{AB}) = \iint \left[ \frac{1}{|\mathbf{r}-\mathbf{r}'|} + \left( \frac{\delta^2 E_{xc}[\rho(\mathbf{r})]}{\delta\rho(\mathbf{r})\delta\rho(\mathbf{r}')} \right)_{n=n_0} \right] \frac{F_{00}^A F_{00}^B}{4\pi} d\mathbf{r} d\mathbf{r}' \quad (2.60)$$

, where  $\gamma$  is discussed more in detail in ref 6.

The final SCC-DFTB energy is transformed into:

$$E_{tot} = \sum_i^{occ} n_i \sum_{\alpha, \beta} c_{i\alpha}^* c_{i\beta} H_{\alpha\beta}^0 + \frac{1}{2} \sum_A^M \sum_B^M \gamma_{AB}(\mathbf{R}_{AB}) \Delta q_A \Delta q_B + E_{rep} \quad (2.61)$$

The coefficients of atomic orbitals can be solved by imposing the condition that the total energy must be stationary with respect to changes of  $c_{i\alpha}$ ,

$$\frac{\partial E_{tot}}{\partial c_{i\alpha}} = 0 \quad \forall i, \alpha \quad (2.62)$$

This leads to a set of secular equations:

$$\sum_{\alpha} c_{i\alpha} (H_{\alpha\beta} + \Omega_{AB} S_{\alpha\beta} - \varepsilon_i S_{\alpha\beta}) = 0, \quad \forall i, \alpha \quad \text{and} \quad \alpha \in A, \beta \in B, \quad (2.63)$$

where

$$\Omega_{AB} = \frac{1}{2} \sum_C^M (\gamma_{AC} + \gamma_{BC}) \Delta q_C \quad (2.64)$$

is the Hamiltonian shift due to induced charge.  $A$  and  $B$  are the indices of the atoms that the atomic orbitals  $\alpha$  and  $\beta$  are located on. Because the Hamiltonian matrix elements depend on the Mulliken charges, but these are calculated from the LCAO coefficients  $c_{i\alpha}$  which in turn are obtained from the secular equations, hence a self-consistency treatment is needed.

### 2.3.3 SCC-DFTB + Dispersion Correction

Van der Waals (vdW) forces, also known as London interactions, are a type of interaction force between two neutral, separated particles with a non-overlapping charge density and without a permanent dipole moment. It is several orders weaker than typical covalent bonds and ionic bonds in molecules. It plays important role in realistic systems. One representative example is the formation of the protein structures in biological systems. Hydrogen bonding and the vdW forces between the base-pairs of amino acids in a protein stabilize the various 3D structures of the proteins and give them different functionalities. The vdW force has a well-known  $R^{-6}$  behavior for two interacting particles, where  $R$  is the inter-particle distance.



To study the systems that include the dispersive force, computational chemistry needs to take into account the long-range interaction between atoms or molecules in a system. The traditional DFT theories lack an ability to handle these kinds of dispersive long range interactions.<sup>17</sup> Hence, to validate the DFT-based SCC-DFTB theory for wider applications into different fields, people add a dispersion term into the SCC-DFTB total energy, aiming to describe the long range interactions more physically and accurately. Presently, there are two different formalisms of the dispersion term being included into SCC-DFTB, one is the Slater-Koster (SK) model by Elstner *et al.*<sup>18</sup> and the other one is the Lennard-Jones (LJ) potential by Zhechkov *et al.*<sup>19</sup>.

We briefly introduce these two types of dispersion interactions. First, for the SK model, London dispersion potential is obtained based on the vdW coefficient ( $C_6$ )<sup>20</sup>.

$$C_6^A = 0.75\sqrt{N_A p_A^3} \quad (2.65)$$

, where  $N_A$  is the Slater-Kirkwood effective number of electrons. For C to Ne atoms, it is given by

$$N_A = 1.17 + 0.33n_v^A \quad (2.66)$$

, with  $n_v^A$  the valence electrons of atom  $A$ .  $p_A$  is the polarizability of atom  $A$ . For diatomic vdW coefficients, the Slater-Kirkwood combination rule is used and the coefficient is given by:

$$C_6^{AB} = \frac{2C_6^A C_6^B p_A p_B}{p_A^2 C_6^A + p_B^2 C_6^B} \quad (2.67)$$

At small inter-atomic distances, the vdW interaction no longer exists and the  $R^{-6}$  term should be damped at the position where the electron densities start to overlap. The damping function is proposed as

$$f(R) = \left[ 1 - \exp(-d(R/R_0)^N) \right]^M \quad (2.68)$$

The determination of the constants is reported in ref 9 and ref 11. The dispersion energy term can be expressed as

$$E_{dis} = -\sum_A \sum_B f(R_{AB}) C_6^{AB} (R_{AB})^{-6} \quad (2.69)$$

The second formalism of dispersion energy is of Lennar-Jones (LJ) type. Using the universal force field (UFF) parameterization<sup>21</sup>, the LJ dispersion includes two parameters: the vdW distance ( $r_{ij}$ ) and well depth ( $d_{ij}$ )

$$U_{ij}(r) = d_{ij} \left[ -2 \left( \frac{r_{ij}}{r} \right)^6 + \left( \frac{r_{ij}}{r} \right)^{12} \right] \quad (2.70)$$

At short range, the LJ potential is substituted by the following polynomial with the parameters given as follows:

$$U_{ij}^{short-range}(r) = U_0 - U_1 r^n - U_2 r^{2n} \quad (2.71)$$

$$U_0 = \frac{396}{25} d_{ij} \quad (2.72)$$

$$U_1 = 2^{5/6} \frac{672}{25} \frac{d_{ij}}{r_{ij}^5} \quad (2.73)$$

$$U_2 = -2^{2/3} \frac{552}{25} \frac{d_{ij}}{r_{ij}^{10}} \quad (2.74)$$

The parameters are determined such that the polynomial can match the zero-, first-, and second derivatives of eq. (2.71). That is, the energy, force and Hessian maintain the continuous character. For details the readers are referred to ref 10 and ref 12.

### 2.3.4 The Derivation of Harmonic Vibrational frequency, Raman Activity and IR Intensity in the SCC-DFTB Scheme

#### Harmonic Vibrational Frequency

The vibrational frequency is an important quantity in chemistry being a unique

fingerprint of molecules or functional groups; it is extensively used in determination of molecular structure or identification of molecular constituents. In quantum chemistry, the harmonic vibrational frequency can be obtained through the second derivatives of the computed total energy with respect to nuclear coordinates. In the SCC-DFTB scheme,<sup>22</sup> harmonic vibrational frequencies are related to the eigenvalues  $\lambda_i$  of the matrix  $\mathbf{m}^{-1/2}\mathbf{G}\mathbf{m}^{-1/2}$  by

$$\omega_i = \sqrt{\lambda_i} \quad (2.75)$$

Here  $\mathbf{m}$  is the diagonal matrix containing the atomic masses, and  $\mathbf{G}$  is the Hessian or force constant matrix.

The Hessian matrix  $\mathbf{G}$  is constituted by the second derivatives of the SCC-DFTB total energy with respect to the Cartesian coordinates

$$G_{ab} = \frac{\partial^2 E}{\partial a \partial b} \quad (2.76)$$

The symbols  $a$  and  $b$  denote any of the  $3N$  Cartesian coordinates in the system containing  $N$  atoms.

In practice, the Hessian can be obtained by differentiating once the atomic forces with respect to the Cartesian coordinates

$$G_{ab} = \frac{\partial F_a}{\partial b} \quad (2.77)$$

with the atomic force given by:

$$F_a = \sum_i^{occ} n_i \sum_{\alpha\beta}^M c_{ia}^* c_{i\beta} \left[ \frac{\partial H_{\alpha\beta}^0}{\partial a} - (\epsilon_i - \Omega_{AB}) \frac{\partial S_{\alpha\beta}}{\partial a} \right] + \Delta q_A \sum_K^M \frac{\partial \gamma_{AK}}{\partial a} \Delta q_K + \frac{\partial E_{rep}}{\partial a} \quad (2.78)$$

A set of coupled perturbed SCC-DFTB equations should then be solved. Details are covered in ref 13.

The harmonic frequency of a vibrational mode informs about the position of the peak in a vibrational spectrum, while the intensity of the mode informs about the height of the peak; both these quantities contribute a complete vibrational spectrum.

The interaction of a static external electric field with molecular electron density can be approximated in the zero-order of multipole expansion as interaction of the field with induced atomic charges. Thus one additional term in the SCC-DFTB Hamiltonian is introduced. This lead to the modified SCC-DFTB total energy :

$$E_{tot} = \sum_i^{occ} n_i \sum_{\alpha,\beta} c_{i\alpha}^* c_{i\beta} h_{\alpha\beta}^0 + \frac{1}{2} \sum_A^M \sum_B^M \gamma_{AB} \Delta q_A \Delta q_B + \sum_A^M \sum_B^M E_{AB}^{rep} - \sum_A^M \Delta q_A \sum_{j=1}^3 D_j x_a(j), \quad (2.79)$$

where  $D_j$  is a Cartesian component of the electric field and  $x_a(j)$  is a Cartesian coordinate of atom  $A$ , with  $j$  equal to  $x, y$ , or  $z$ . We minimize the energy by setting  $\frac{\partial E_{tot}}{\partial c_{i\alpha}}$  to zero, which leads to a new set of secular equations, further differentiation of the modified energy with respect to nuclear coordinates gives the new atomic force on atoms in the presence of an external electric field.



### Raman Intensity

The Raman activities (Raman intensities can be derived from activity) and IR intensities are also implemented into the SCC-DFTB code<sup>23,24</sup>. The Raman intensity can be estimated using the Placzek's theory of polarizability as described above. We consider the first-order geometrical derivatives of polarizability tensor at the equilibrium molecular geometry,

$$\frac{\partial \alpha_{ij}}{\partial Q_k} \quad \text{for } i, j = x, y, z, \quad (2.80)$$

where  $Q_k$  is the normal coordinate associated with  $k$ th molecular vibration.

In practice, we calculate the polarizability tensor in the following way:

$$\frac{\partial \alpha_{ij}}{\partial Q_k} = \sum_a \frac{\partial \alpha_{ij}}{\partial a} \frac{\partial a}{\partial Q_k} = \sum_a \frac{\partial^3 E}{\partial a \partial D_i \partial D_j} \frac{\partial a}{\partial Q_k} = \sum_a \frac{\partial^2 F}{\partial D_i \partial D_j} \frac{\partial a}{\partial Q_k} \quad (2.81)$$

Subsequently, two invariants of polarizability derivatives are calculated,

the mean value  $\bar{\alpha}$  and the anisotropy  $\gamma$ :

$$\bar{\alpha} = \frac{1}{3} \left( \frac{\partial \alpha_{xx}}{\partial Q_k} + \frac{\partial \alpha_{yy}}{\partial Q_k} + \frac{\partial \alpha_{zz}}{\partial Q_k} \right) \quad (2.82)$$

$$\begin{aligned} \gamma^2 = \frac{1}{2} & \left[ \left( \frac{\partial \alpha_{xx}}{\partial Q_k} - \frac{\partial \alpha_{yy}}{\partial Q_k} \right)^2 + \left( \frac{\partial \alpha_{xx}}{\partial Q_k} - \frac{\partial \alpha_{zz}}{\partial Q_k} \right)^2 + \left( \frac{\partial \alpha_{yy}}{\partial Q_k} - \frac{\partial \alpha_{zz}}{\partial Q_k} \right)^2 \right] \\ & + 3 \left[ \left( \frac{\partial \alpha_{xy}}{\partial Q_k} \right)^2 + \left( \frac{\partial \alpha_{yz}}{\partial Q_k} \right)^2 + \left( \frac{\partial \alpha_{zx}}{\partial Q_k} \right)^2 \right] \end{aligned} \quad (2.83)$$

The Raman activity of each vibration can be obtained as

$$S_n = \frac{1}{45} \left( 45\bar{\alpha}^2 + 13\gamma^2 \right) \quad (2.84)$$

$$S_p = \frac{1}{45} \left( 45\bar{\alpha}^2 + 7\gamma^2 \right), \quad (2.85)$$

where the subscript  $n$  and  $p$  stand for the *natural* light or *plane-polarized* light as the source of radiation.

Finally, the Raman intensity for each vibration is given by

$$I_n = KI_0 \frac{(\nu_0 - \nu_k)^4}{M\nu_k(1 - e^{-h\nu_k/kT})} \left( 45\bar{\alpha}^2 + 13\gamma^2 \right) \quad (2.86)$$

for the natural incident light, and

$$I_p = KI_0 \frac{(\nu_0 - \nu_k)^4}{M\nu_k(1 - e^{-h\nu_k/kT})} \left( 45\bar{\alpha}^2 + 7\gamma^2 \right) \quad (2.87)$$

for the plane-polarized incident light.

The constants are defined as

$\nu_0$  : the frequency of the incident light

$I_0$  : the intensity of the incident light

$M$  : the effective mass of each vibrational mode (equals to one because the normal coordinates  $Q_k$  have been mass-wieghted.)

$\nu_k$  : vibrational frequency of the  $k$ th mode

$K$ : constant set to one in our calculations<sup>12</sup>

$T$ : the temperature in Kelvin

## IR Intensity

The intensities in the IR vibraional spectrum are closely related to changes of molecular dipole moment  $\mu$  during the molecular oscillation. When in diluted gases it can be evaluated as<sup>24</sup>

$$A_i = K \left( \frac{\nu_i}{\omega_i} \right) \left[ \left( \frac{\partial \mu_x}{\partial Q_i} \right)^2 + \left( \frac{\partial \mu_y}{\partial Q_i} \right)^2 + \left( \frac{\partial \mu_z}{\partial Q_i} \right)^2 \right] \quad (2.88)$$

Here  $A_i$  is the IR intensity,  $\nu_i$  is the fundamental frequency and  $\omega_i$  is the harmonic frequency of the  $i$ th vibration. The constant  $K$  and the ratio of fundamental and harmonic frequencies  $\frac{\nu_i}{\omega_i}$  are set to unity in our calculations. In practice, we calculate the dipole moment derivatives using the following formula to save computing time:

$$\frac{\partial \mu_j}{\partial Q_j} = \sum_a \frac{\partial \mu_j}{\partial a} \frac{\partial a}{\partial Q_j} = \sum_a \frac{\partial^2 E}{\partial a \partial D_j} \frac{\partial a}{\partial Q_j} = \sum_a \frac{\partial F_a}{\partial D_j} \frac{\partial a}{\partial Q_j} \quad (2.89)$$



# Chapter 3

## Technical Details

All the molecular energies, geometrical optimizations and vibrational spectra calculations were employing the FORTRAN based SCC-DFTB code. For the solid state band structure calculations, the SCC-DFTB+<sup>25</sup> code was employed.

The force convergence criterion for all the geometrical optimizations in this study is  $10^{-6}$ . The SCC threshold was set to be  $10^{-12}$ .

To plot the bond length distributions, IR and Raman vibrational spectra, VDOS and DOS, we use Gaussian functions to smear the discrete raw data, then we superpose these Gaussians to make the plots.

For all the 2D plots in this study, the program GRACE under the GNU project had been employed. 3D plots were carried out using the GNUPLOT program and SIGMAPLOT for the PES of  $C_{60}@C_{240}$ . The molecular geometries are visualized using the MOLDEN program and GAUSSVIEW.

# Chapter 4

## Results and discussion

### 4.1 Conjugated Heterocyclic Polymer Chains

The main idea of this study is to investigate the evolution of various physical properties of  $\pi$ -conjugated oligomers with the increasing length of the system. In the limit of an infinite chain, the studied systems converge toward polymers. Thus, it would be natural to think that also the properties of the finite oligomers should converge toward those of the polymers. This concept is a foundation of so-called “oligomer approach”<sup>26</sup> used for experimental and theoretical determination of properties of infinite polymers. A natural, theoretical alternative to the oligomer approach are the usual techniques of solid-state physics dealing with infinite systems and the translational symmetry. Both of these methodologies were used in a number of studies to investigate a variety of physical properties of extended systems.<sup>27-39</sup>

However, none of these publications was fully devoted to a systematic analysis of the rate of convergence of the aforementioned properties of finite molecules upon elongation toward the values characteristic for the corresponding infinite systems. Such practical knowledge would certainly simplify the studies of polymers based on the oligomer approach. At present, one has to investigate a series of homologues—some of them very far from the convergence region and some of them already beyond the saturation limit—to get the information about the properties of polymers. This makes the oligomer approach, theoretical or experimental, unnecessarily expensive and cumbersome. Thus, a methodical determination of the



convergence region for various oligomer properties would make such studies much more automatic and efficient.

In this paper we investigate the behavior of various geometrical and electronic properties of a series of structurally-related  $\pi$ -conjugated oligomers in their ground electronic states. We explicitly consider oligomers built of the following *trans*-connected monomers: *cis*-1,3-butadiene, cyclopentadiene, pyrrole, furan, and thiophene. In principle, two mesomeric forms are possible for the studied systems, aromatic and quinoid (or *trans*-cisoid and *cis*-transoid, respectively),<sup>33</sup> which differ by the relative position of double bonds in the carbon backbone. Since it was demonstrated<sup>40</sup> that the former form is substantially lower in energy, we consider only the aromatic-like oligomers and polymers. Note that the resulting infinite structure obtained from *cis*-1,3-butadiene is distinct from that one of all-*trans*-cisoid polyacetylene that was studied previously.<sup>41</sup> We focus on the rate of convergence of the following physical properties: equilibrium structures, HOMO-LUMO energy gaps, electronic densities of states, distributions of induced charges, dipole and quadrupole moments, and polarizabilities. Our main interest lies in determining how rapidly the aforementioned properties saturate towards a constant value in the interior of the oligomers. Also, we want to find out the minimum length of the oligomer chain for which the properties are indistinguishable from those of a given polymer. Selected properties of the systems studied here were already investigated either theoretically or experimentally in a number of studies. A complete review of these studies is out of scope of the present work. However, the concise compilation presented here for the polymers and oligomers built of the acetylene,<sup>42,43</sup> cyclopentadiene,<sup>32,43,44</sup> pyrrole,<sup>32,39,41,43-47</sup> furan,<sup>32,41,43-46</sup> and thiophene<sup>32,41,43-46</sup> units is supposed to give a representative sample of the related research.

The theoretical tool used for our analysis is based on the SCC-DFTB

approximation<sup>4</sup>. which can be considered as a simplified version of density functional theory (DFT). We are fully aware that the results obtained within the framework of this method may not be very accurate. In fact, quantitative assessment of some of the studied properties, e.g., polarizability or quadrupole moment, is known to require highly advanced theoretical techniques and large basis sets. However, we are interested in the evolution of the physical properties rather than in their actual values. We are convinced that the qualitative picture we have obtained is correct even if the quantitative accuracy may need further verification by more elaborate theoretical treatment. On the other hand, using SCC-DFTB gives us the advantage of investigating extended molecular systems necessary to study the evolution of properties, which converge only in the limit of very large oligomers containing hundreds of atoms. An argument in favor of using SCC-DFTB for the analysis of  $\pi$ -conjugated systems is the successful application of this method in studying analogous properties of finite and infinite linear carbon chains.<sup>48</sup> A comparison with experimental and more advanced theoretical results demonstrated an excellent performance of the approximate approach. Another very important advantage of using the SCC-DFTB method for our investigation is the possibility of a direct comparison with the analogous solid-state results. It should be stressed that the same identical SCC-DFTB Hamiltonian is used within the usually incompatible frameworks of quantum chemical and solid-state machineries. For the studied evolution of physical properties in oligomers, the solid-state calculations provide us with the necessary benchmark of relevant values for infinite polymers.

The practical applicability of our results is not limited only to the methodological issues. The conclusions obtained from our investigations can be directly applied for studying various properties of conducting polymers, which have stimulated widespread attention since Shirakawa's discovery of highly conductive

polyacetylenes.<sup>49</sup> The conjugated polymers are widely applied to fabricate light emitting diodes (LED)<sup>50-52</sup>, biosensors<sup>53,54</sup>, photovoltaic cells<sup>55</sup>, etc. The first five-member heterocyclic polymers studied in detail were polypyrrole and polythiophene. Polypyrrole was found to be an insulator with a band gap of 2.85 eV.<sup>27</sup> However, after oxidative doping its conductivity reached 500 S/cm.<sup>56</sup> Polythiophene was also found to be an insulator with a slightly smaller band gap of 2.0 eV<sup>30</sup>, and the conductivity of 2000 S/cm was reported for its doped derivatives.<sup>28</sup> Later, a successful synthesis of polyfuran, with a band gap of 2.35 eV and conductivity of 100 S/cm (in a doped form), was reported.<sup>29,35</sup> Polycyclopentadiene has been studied only theoretically.<sup>31-34,37,43,44</sup> The smallest computed band gap is 0.98 eV (extrapolated TD-DFT/B3LYP oligomer results). Eventually, *trans-cis*-polyacetylene, which can be treated as the carbon skeleton of all of the previously discussed systems, was studied theoretically as a less stable isomer of all-*trans*-polyacetylene.<sup>30,41,42</sup> The presence conjugated  $\pi$ -electron system results also in increased dependence of polarizabilities and second-order hyperpolarizabilities on details of the molecular structure, which opens the way of engineering the molecular properties so that they can be used in various photonic devices like optical switches, logical gates or signal processors.

The chemical formulas of polymers studied in this work are shown in Table 4.1 .

**Table 4.1** Molecular formulas for all the considered  $n = 1\sim 50$  molecular models of oligomers.

Molecules	Formula	number of atoms in the largest model
Trans-cisoid polyacetylene	$8m+2$	402
Polycyclopentadiene	$9m+2$	452
Polypyrrole	$8m+2$	402
Polyfuran	$7m+2$	352
Polythiophene	$7m+2$	352

We have considered explicitly five families of one-dimensional polymers: trans-cisoid polyacetylene, polycyclopentadiene, polyfuran, polypyrrole, and polythiophene. The size of the studied finite oligomers has varied from a single monomer ( $m=1$ ) unit to 50 monomer units ( $m=50$ ). The models are assumed to be planar. (This assumption has been further validated by vibrational analysis.) Their schematic geometrical representation together with molecular symmetry is shown in Fig 4.1 separately for the even and odd number of monomers. In addition to the quantum chemical calculations for the finite oligomers we have performed calculations for the infinite polymer chains ( $m=\infty$ ) using a standard solid state approach. The unit cell used in these calculations—shown in Fig 4. 1a—is composed of two monomer units. By construction our molecules possess translational symmetry in one dimension and therefore they can be considered as one-dimensional crystals. Although the effects of the interchain interactions, defects, and doping present in real three-dimensional crystals have been neglected, we still believe that our models are closely related to experimentally investigated structures and can yield valuable information about the convergence behavior for various molecular properties for each type of polymers.

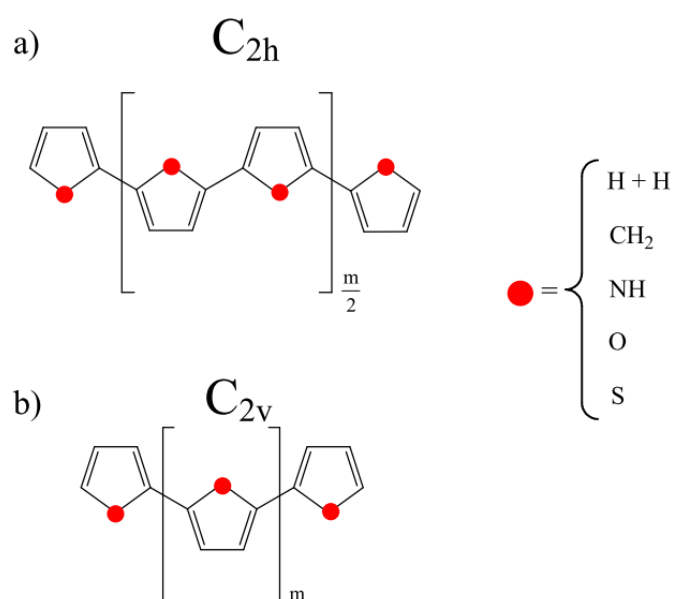


**Figure 4.1** Models of a) the  $C_{2h}$  and b)  $C_{2v}$  symmetric oligomers.

Both the quantum chemical and solid state calculations have been performed in the framework of the SCC-DFTB method. In the solid-state calculations, the initial unit cell structure of each system has been extracted from the central region of the longest studied finite oligomers (50-mer). The lattice vectors perpendicular to the main axis of each polymer have been set to 100 Å to simulate a quasi-one-dimensional periodic structure. The positions of atoms within the initial unit cell and the remaining lattice constant  $a$  have been optimized to yield a structure corresponding to minimal energy. After obtaining the equilibrium geometry of the unit cells, we have used 500  $k$ -points between 0 and  $\pi/a$  to sample the band structure of each 1D polymer and to construct the electronic density of states (DOS) plots.

In the present work we investigate the evolution of geometric and electronic properties of a family of finite heterocyclic oligomers upon the elongation of the chain. The molecular properties studied explicitly are equilibrium geometries, electronic densities of states (DOS), HOMO-LUMO gaps, distribution of induced charges, dipole moments, quadrupole moments, and polarizabilities. The results obtained for finite chains are compared with the corresponding solid state calculations, previous theoretical findings, and with experiment (whenever possible). Analogous results obtained for the vibrational and spectroscopic properties will be discussed in the subsequent study.

#### **4.1.1 Evolution of Equilibrium Structures**

We have computed equilibrium SCC-DFTB geometry for a series of finite oligomers built of five-membered monomer units introduced earlier. We are going to analyze the evolution of selected equilibrium bonds and angles, as represented in Figs. 4.2 and 4.3

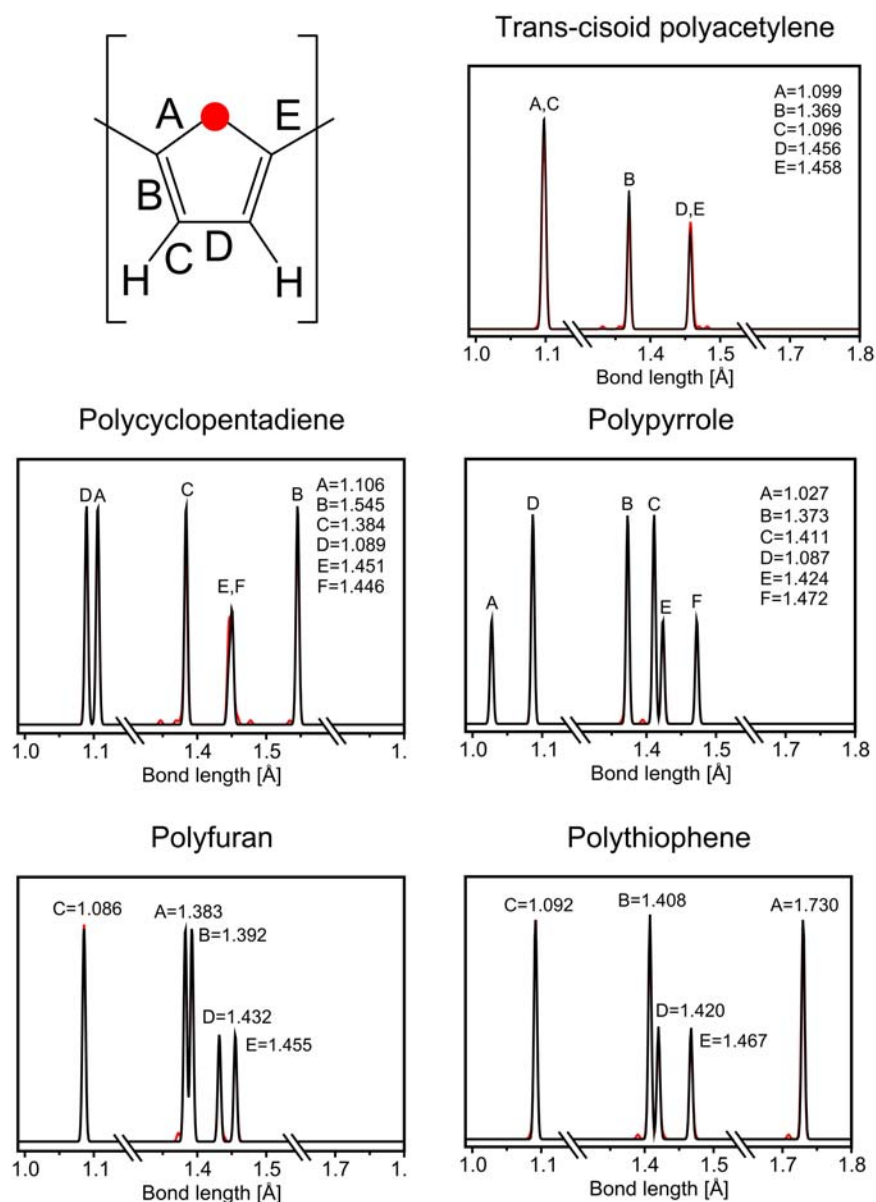


**Figure 4.2** Bond length distribution comparisons between the molecular 50-mer (red line) and solid-state polymer (black line) of all the considered models in this study.

The distribution of equilibrium bond lengths for the infinite polymers (solid black line) and for the longest studied oligomers (solid red line) is shown in Fig. 2. It is clear that both distributions are almost identical for all the considered systems. The only difference concerns a few small peaks associated with the terminal monomers. A brief inspection of Fig. 4.

be identical. This observation gives us the first important conclusion of this study, which states that the equilibrium geometry of an infinite system can be accurately

accessed using the corresponding finite-length model. A natural question arising from this observation is how long the oligomer chain should be to reproduce the geometric parameters of the polymer. Figure 4.2 shows that 50-mers are more than sufficient for this purpose. In fact, Figures 4.3 and 4.4 demonstrate that the convergence of equilibrium bond lengths and angles is obtained much faster; they reach the bulk limit for approximately 15–20 monomer units. The most dramatic changes in molecular geometry are observed for very short oligomer chains ( $m=1-10$ ), which shows that such short chains should not be used for modeling the properties of polymers. However, the analysis of the presented data suggests that already a 20-mer makes an adequate geometrical model of an infinite polymer chain. Since the differences in the bond distributions for the finite and infinite systems come mainly from the effect of the terminal units, we have investigated in detail the behavior of selected bond lengths and bond angles as a function of their position in the chain, using the finite 50-mer of pyrrole as a representative of all the systems under study. The results are presented in Fig. 4.4 for two bond lengths and two bond angles (as defined in Fig. 4.2). The results are more than surprising! Figure 4.4 shows that the effect of the finite termination is very local and is limited only to the 3–4 monomers adjacent to the terminal unit.



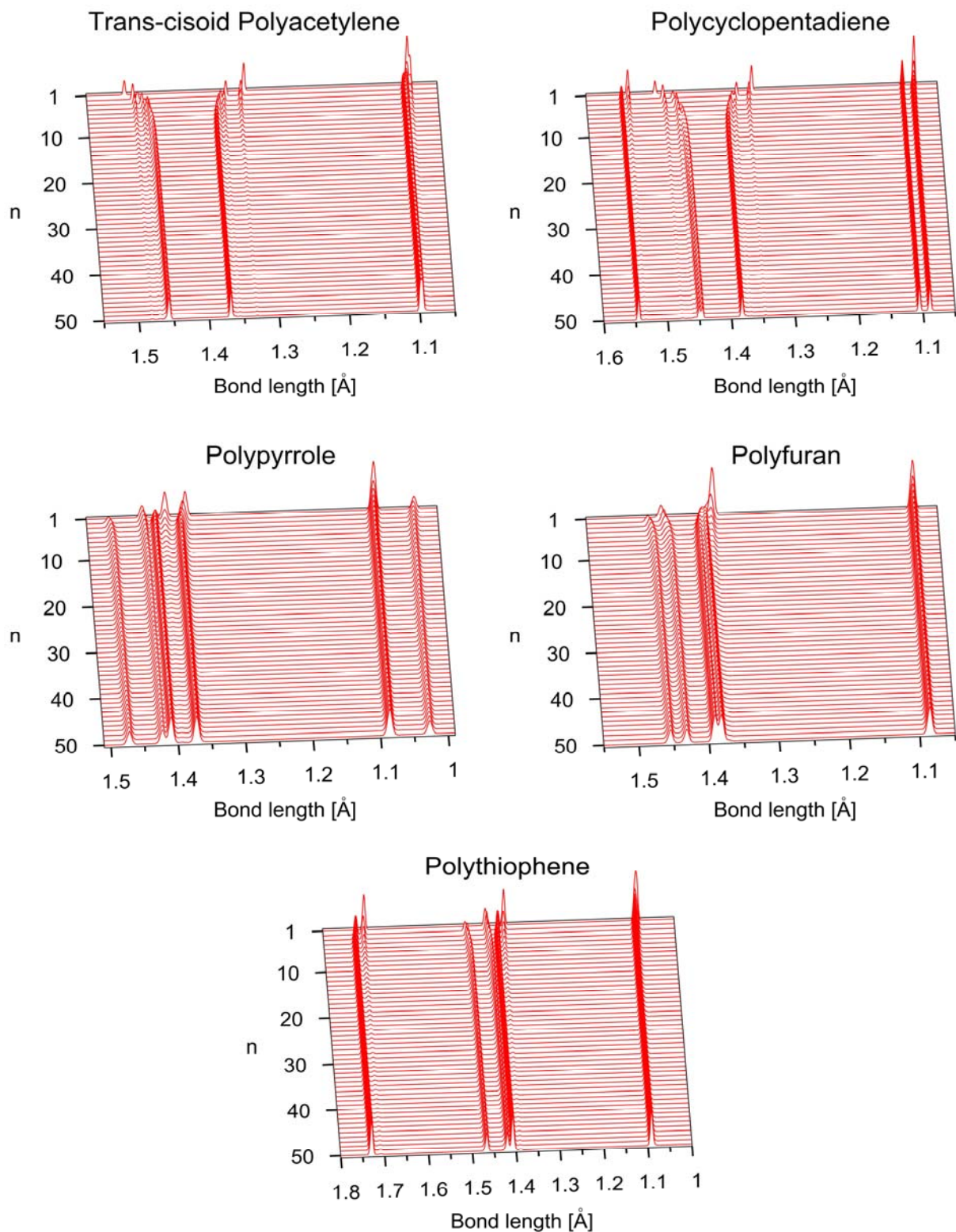


**Figure 4.3** Bond length distribution convergence of the considered models in this study.



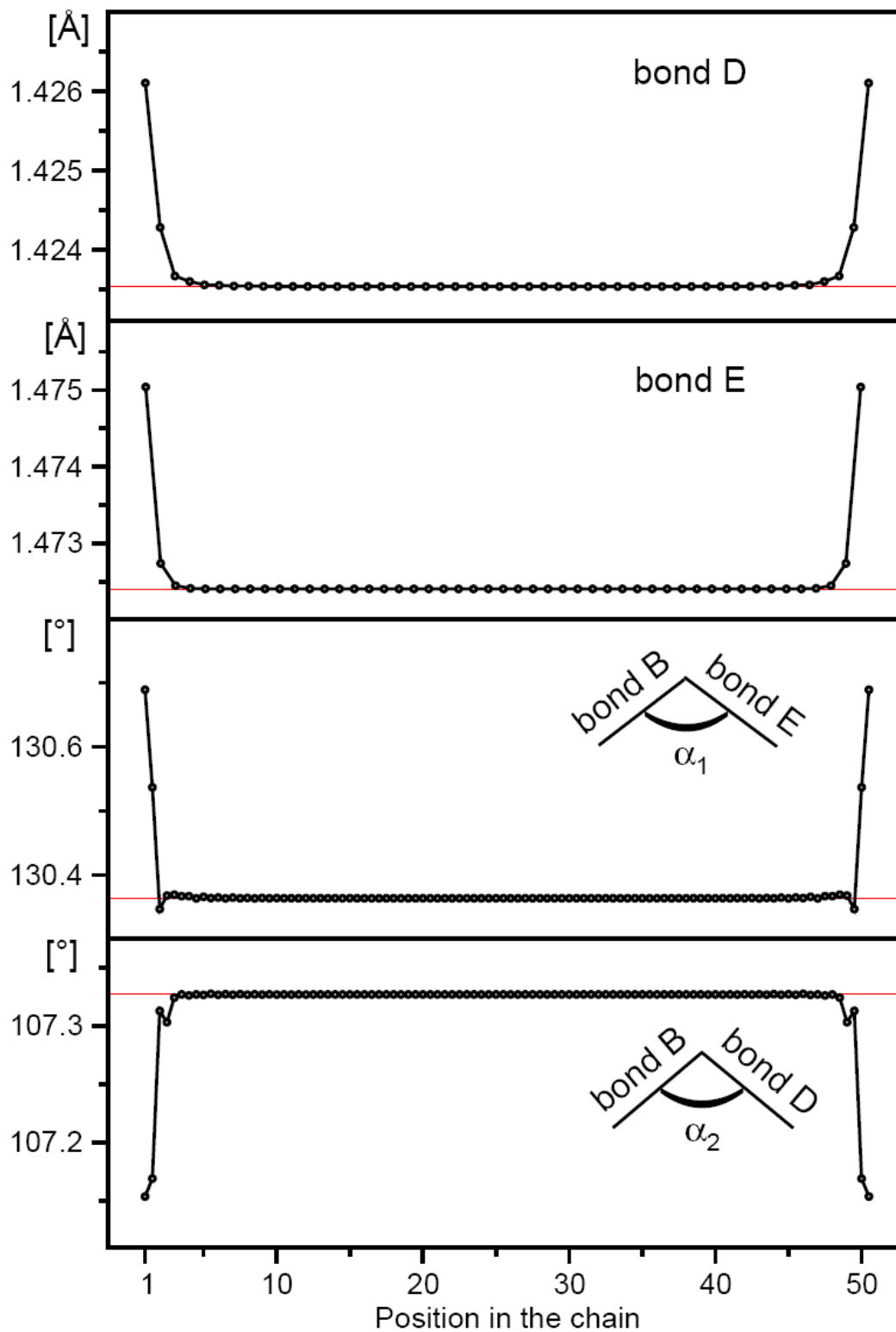


**Figure 4.4** Bond length and bond angle distribution of pyrrole 50-mer. Calculated values of solid state polypyrrole are given in red solid lines.

To highlight this effect, we have also plotted in Fig. 4 the limit value obtained from the corresponding solid state calculations. The whole interior of the 50-mer of pyrrole is virtually identical to the structure of the infinite polymer. This observation gives us the second important conclusion of this study, which states that the equilibrium structure of the infinite polymer chain can be obtained by inspecting the interior of relatively short oligomer chains built of approximately 20 monomer units. In fact, almost perfect structural parameters of a polymer can be extracted already from the central unit of the corresponding decamer.<sup>44,57</sup> For shorter chains, an experimental X-ray study of single crystals of terthiophene and sexithiophene single crystals showed that the geometry variation in the central units is of order 0.01 Å for bond lengths and 1° for valence bond angles. Further elongation of the chain to 12 monomer units modifies the bond lengths by another 0.01 Å.

Structural similarity of the five studied families of oligomers calls for investigation of the effect of the heteroatom substitution on the structure of the polymer. This can be easily done using Fig. 2, in which analogous types of bonds for the five studied systems are marked with the same letters. Clearly, it is not very informative to compare the bond lengths between the carbon atoms and the heteroatom (i.e., bond A), but the analysis of carbon backbone structure (i.e., bonds B, D, and E) should yield interesting information. The first two systems (i.e., *trans-cis*-polyacetylene and polycyclopentadiene) are expected to have polyene-like structure, while the remaining three systems should display a certain degree of aromaticity within the monomer rings. This regularity can be observed in the  $r_D - r_B$  bond length difference, which is 0.087 and 0.067 Å for *trans-cis*-polyacetylene and polycyclopentadiene, respectively, and only 0.012 and 0.013 Å for polythiophene and polypyrrole, respectively. For polyfuran, a value of 0.040 Å reveals a structure intermediate between the polyenic and aromatic one. It is interesting to compare these values to the analogous data for a

single monomer, which are: 0.170 Å for 1,3-butadiene, 0.151 Å for cyclopentadiene, 0.034 Å for pyrrole, 0.073 Å for furan, and 0.042 Å for thiophene.<sup>CCCBDB</sup> Two facts are apparent from this comparison: i) the aromatic character of a given monomer is enhanced upon the elongation of the chain and ii) the semi-aromatic character of polyfuran is inherited from the monomer. Additionally, we can state that the bonds connecting the adjacent monomers are predominantly single in their character. However, the bond lengths are somewhat smaller for monomers displaying less aromatic character, which may be rationalized in terms of enhanced delocalization of the  $\pi$  electrons along the chain. Note that the computed SCC-DFTB values of the  $r_D - r_B$  bond length differences in isolated monomers compare rather favorably with experimental data, which are: 0.139 Å for 1,3-butadiene, 0.120 Å for cyclopentadiene, 0.035 Å for pyrrole, 0.070 Å for furan, and 0.053 Å for thiophene.<sup>CCCBDB</sup> Unfortunately, experimental data for longer oligomers and polymers are very scarce, which impedes experimental verification of our theoretical results.

For all the studied oligomers, the optimized SCC-DFTB dihedral angles between the adjacent monomers are equal to 180°. In fact, equilibrium geometries of some of the analyzed oligomers obtained from more advanced calculations are not strictly planar.<sup>58</sup> In the case of oligothiophenes the energy changes associated with deviations from planarity are small owing to low curvature of the potential energy surface along the inter-ring torsional angles; the infinite polythiophene chain has been found to be indeed planar.<sup>58</sup> It was also found that aromatic systems tend to maintain their aromaticity for small twisting angles.<sup>59-64</sup> Thus, one may expect that the impact of the non-planarity on the physical properties of the unsubstituted conjugated oligomers and on their remaining geometric parameters is rather marginal.<sup>39,58,65</sup> (Note that for substituted systems, large steric hindrance can lead to highly non-planar structures with seriously modified molecular properties.<sup>53</sup>) This effect of non-planarity is

anticipated to be particularly small for long chains, which spontaneously gravitate toward the planar infinite structures.

#### 4.1.2 Evolution of HOMO–LUMO Energy Gaps

Experimental and theoretical investigations of the energy gaps of conjugated polymers via the analysis of the HOMO–LUMO gaps of a series of finite oligomers received considerable attention.<sup>40,42</sup> The computed HOMO–LUMO gaps for the five families of studied oligomers are presented in Fig. 4.5. The convergence of the HOMO-LUMO gaps towards the corresponding polymer band gaps seems very fast. However, closer scrutiny of Fig. 4.5 shows that the actual behavior is more complex. For oligomers of certain length, the HOMO-LUMO energy gap dependence on the reciprocal of the number of monomers  $m$  slowly begins to change from linear to quadratic.<sup>57</sup> Deviations from the linear trend are initially very subtle and one has to study quite long oligomers (20-mers, 30-mers, or even longer) to obtain a distinct quadratic dependence allowing for the proper (quadratic) extrapolation procedure.<sup>46</sup> The slow change in the nature of dependence the HOMO-LUMO gap with respect to  $1/m$  was the source of serious inaccuracies in a number of the reported polymer band gaps, obtained by applying the linear extrapolation procedure to the oligomer results.<sup>8</sup> Our SCC-DFTB calculation estimates of the band gaps for the systems under study, using a quadratic fit for the longest 40 structures (so that the linear region is avoided) yields values almost identical to the actual energy gaps in infinite polymers obtained from the solid state simulations. The correlation coefficients  $r^2$  are all 0.99 for the quadratic fitting curves of the five systems. The convergence of the HOMO–LUMO gaps for oligomers toward the band gaps of the corresponding polymers is demonstrated in Table 4.2 Note that for the longest studied finite chains, the HOMO-LUMO gap itself constitutes a good estimate of the polymer energy gap.

## Band gaps of all the considered models

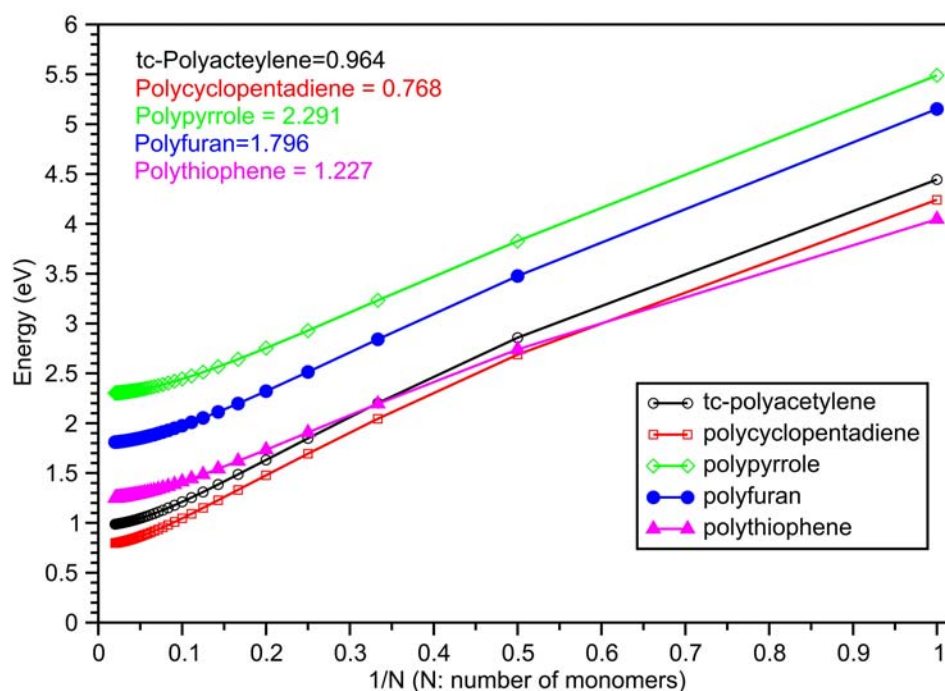


**Figure 4.5** Band gaps of all the considered models. The values shown are the extrapolated results using second-order polynomial fitting for the last forty points.

The actual value of the energy gap is proportional to the degree of the  $\pi$ -electron delocalization along the polymer chain. Inspection of Table 4.1 shows, that apparently the electrons can move more freely along the polymer chain in polycyclopentadiene and polyacetylene than in the polymers built of the heterocyclic rings. Also, the presence of strongly electronegative, second row heteroatoms (nitrogen and oxygen) seems to hinder the electronic mobility, as the band gaps of the corresponding polymers are larger than the one for polythiophene.

**Table 4.2** HOMO-LUMO gaps and the differences between the oligomers and the solid-state value.

	HOMO-LUMO Gaps				
	tc-PA	PCp	PPy	PFu	PTh
Exp.			2.85	2.35	2.0
10-mer	1.211	1.045	2.444	1.975	1.412
20-mer	1.046	0.865	2.337	1.851	1.292
30-mer	1.008	0.821	2.314	1.824	1.264
40-mer	0.994	0.805	2.306	1.814	1.252
50-mer	0.987	0.797	2.302	1.81	1.247
extrapolated 50-mer	0.964	0.768	2.291	1.796	1.227
polymer	0.974	0.782	2.295	1.801	1.231
$\Delta$ polymer_10-mer	0.243	0.336	0.065	0.097	0.147
$\Delta$ polymer_20-mer	0.074	0.106	0.018	0.028	0.050
$\Delta$ polymer_30-mer	0.035	0.050	0.008	0.013	0.027
$\Delta$ polymer_40-mer	0.021	0.029	0.005	0.007	0.017
$\Delta$ polymer_50-mer	0.013	0.019	0.003	0.005	0.013
$\Delta$ polymer extrapolated 50-mer	0.010	0.018	0.002	0.003	0.003

all units in eV

### 4.1.3 Evolution of Electronic DOS Distributions

The electronic density of states (DOS) is defined in solid state physics as an integral of one-electron energy levels over the Brillouin zone. In practice, however, only a finite number of Brillouin zone's points are sampled and the electronic DOS is obtained as a superposition of a finite number of the discrete energy levels. To ensure smooth character of DOS constructed in such a way, the discrete energy levels are usually smeared using a Gaussian envelope of a constant width (sometimes referred to as the relaxational broadening<sup>24</sup>). The equivalence of these two procedures in the limit of large number of sampling points suggests that the electronic DOSs can be also constructed using the set of discrete one-electron energy levels (i.e., orbital energies) of finite oligomers. This idea was used by Salzner *et al.*<sup>17</sup> to show in a qualitative way that the orbital levels of oligomers develop in the infinite limit into the band structures of the corresponding polymers. We have further tested this hypothesis in a quantitative way by plotting the resulting—finite and infinite—electronic densities of

states in Fig. 4.6 Since SCC-DFTB employs minimal atomic basis sets, it is only meaningful to analyze the resulting DOSs around the Fermi level. To facilitate the analysis of these graphs, the peaks corresponding to the occupied energy levels (valence band) have shaded area, while those corresponding to the virtual energy levels (conduction band) are depicted with a solid line. The electronic DOSs for finite oligomers presented in Fig. 4.6 show a surprisingly fast convergence toward the infinite limit. Already for less than 10 monomer units, the finite DOSs are very similar to the one of the polymer. The electronic DOSs for the longest studied oligomers ( $m=50$ ) are practically indistinguishable from those obtained in the solid state calculations. Similar observation was previously made for polypyrrole,<sup>24</sup> for which the DOS for oligomers built of six monomer units and the DOS for the corresponding polymer were closely related. Note that for each of our finite length oligomers, there are some tiny additional peaks present in every DOS. These spurious peaks correspond to the energy levels of the terminal hydrogen atoms. Obviously, the relative magnitude of these peaks decreases with the growing size of the chain and it is reduced to zero in the infinite limit.



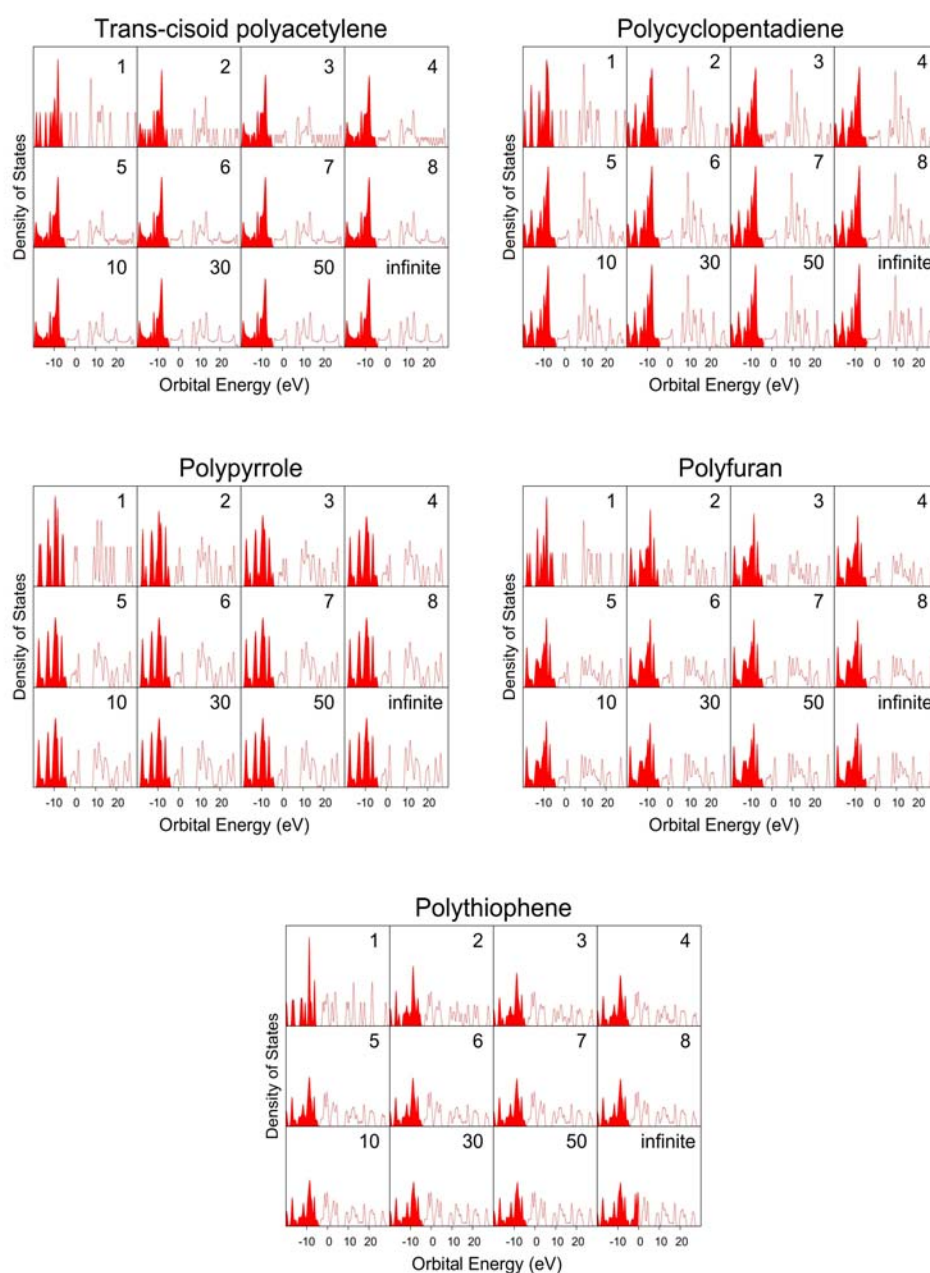


**Figure 4.6** Electronic DOS distribution convergence of all the considered models. The red areas correspond to the occupied valence bands. The red area and white area are separated by the calculated Fermi level.

#### 4.1.4 Evolution of Charge Distribution

Another important molecular quantity studied in this work is the electronic charge distribution. The main focus here is on the change of induced atomic charges with the position of a given atom along the chain. We also investigate how the induced charge



distribution varies with the elongation of the oligomer. The induced atomic charges are computed using the Mulliken population analysis. The structure of the studied oligomer chains dictates a natural distinction between the atoms constituting the  $\pi$ -conjugated carbon skeleton and the heteroatoms. Therefore, we investigate the evolution of induced charges for these two subsystems separately. In fact, the term “heteroatom” has been used here a little frivolously as we also applied it to describe the  $sp^3$  carbon atom of cyclopentadiene. However, its use underlines a different character of that atom with respect to the carbon atoms involved in the  $\pi$ -conjugated system. Note that no heteroatom is present in the case of *trans-cis*-polyacetylene, which leads to a slightly different behavior of this system in comparison with the other chains.

First we discuss the distribution of the induced charges along the longest studied oligomer chains. Figure 4.7 shows the induced charges on the heteroatoms. The most striking feature is nearly instantaneous convergence of the induced charge to the bulk value. The effect of the chain boundaries is visible only at the two terminal monomers. All the remaining monomers have virtually the same induced charge as the infinite polymer. Figure 4.8 shows the change of induced charges along the  $\pi$ -conjugated chains of carbon atoms. The  $C_{2v}$  symmetry of the monomer units implies the presence of two pairs of carbons with identical charges,  $C_\alpha$  and  $C_\beta$ , as defined in Figure BB. The symmetry enforces the same behaviour in the corresponding, infinite polymer chains. Therefore, we expect that similar behavior can be also observed for the finite oligomers. Analysis of Figure 4.8 shows that such symmetry of charge distribution is indeed observed in oligomers, as long as a given monomer is not located too close to the chain boundary. The charges at the two-three terminal units deviate from the values calculated for the corresponding polymers, but the charges at all the remaining monomers are virtually indistinguishable from those in polymers. Again, the rate with

which the charges reach the bulk value is quite striking.

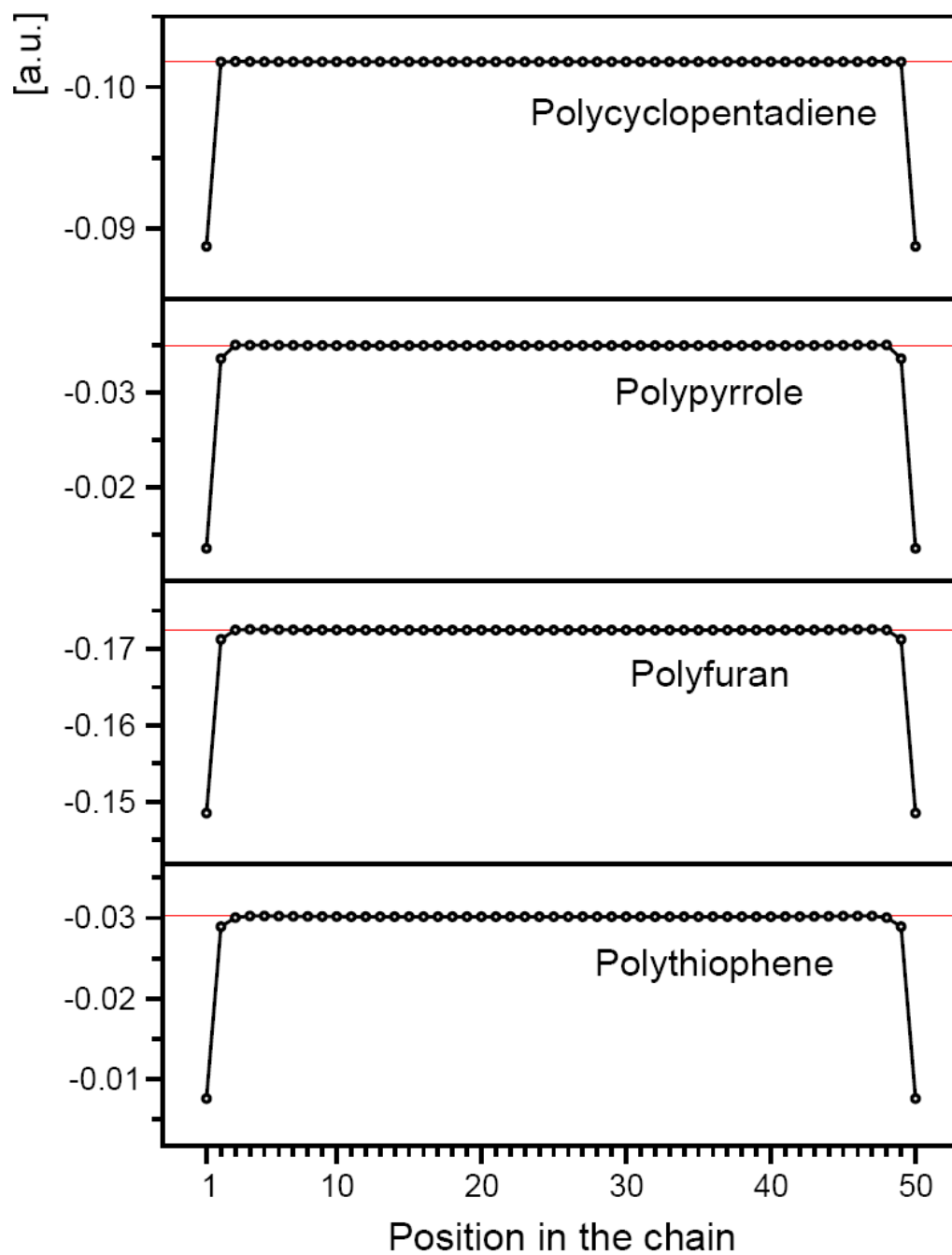


**Figure 4.7** Induced Mulliken charges of the heteroatoms of the 50-mer in each system. The red solid lines are the corresponding solid-state values.

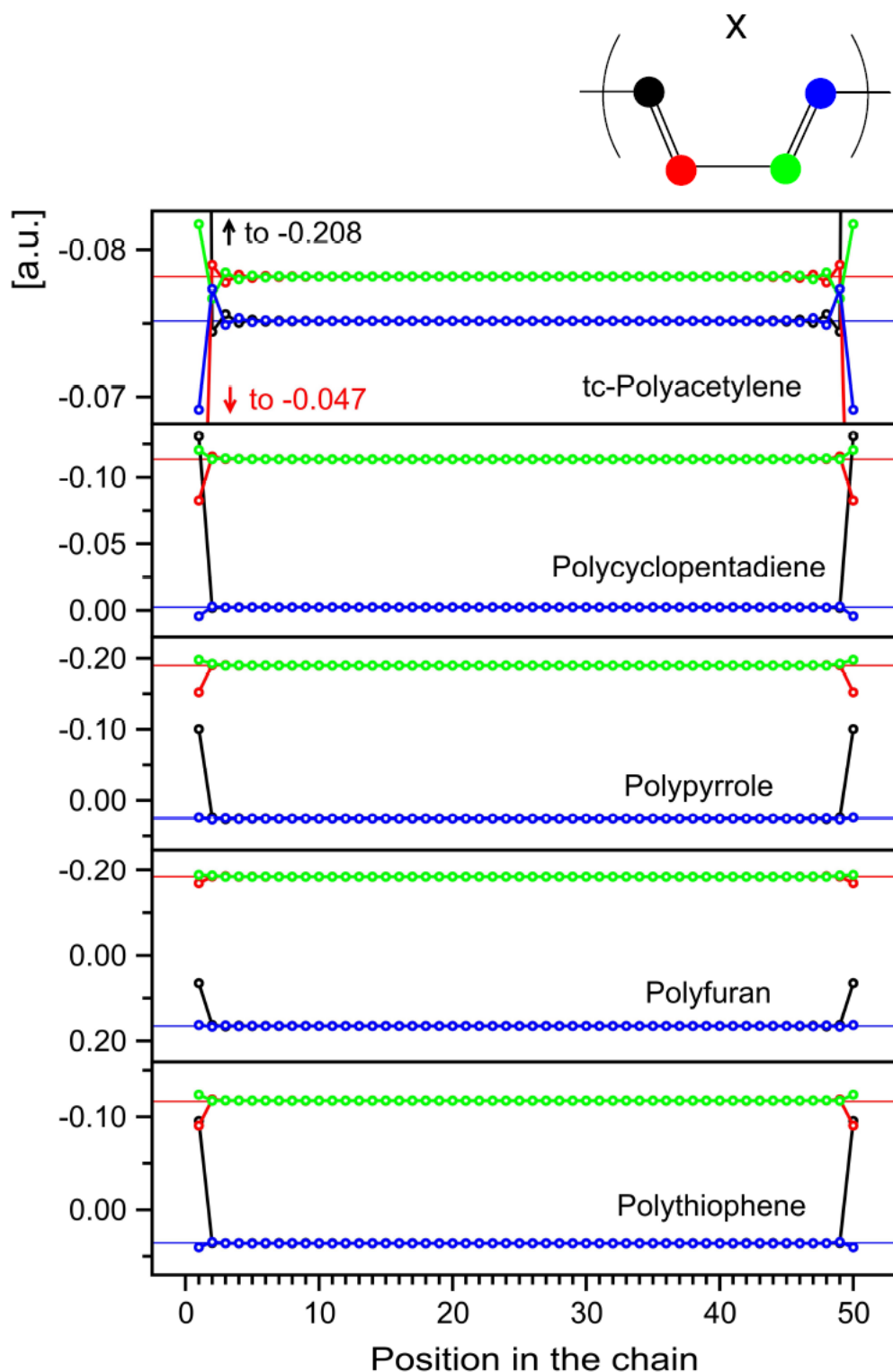


**Figure 4.8** Induced Mulliken charges along the  $\pi$ -conjugated carbon backbone of the 50-mer in each system. Solid lines in red and blue are the solid-state values.

It is obvious that for *trans-cis*-polyacetylene, the charges on carbons  $\alpha$  and  $\beta$  must be very similar, owing to their nearly identical surroundings. A slight difference

between these two charges stems from the *cis-trans* alternation in the chain structure. (Note that in the *trans*-only chain the values would be identical). In all other cases the difference is more pronounced and depends quite strongly on the heteroatom present in the ring. However, significant differences in the charge distribution within a monomer have little influence on the observed fast convergence of the calculated induced charges towards the bulk values. It thus appears to be a universal characteristic of the oligomers with conjugated system of  $\pi$ -bonds.

Eventually, let us inspect the evolution of the induced charges with the elongation of the oligomer chain. The detailed analysis performed above for the 50-mers reveals that the induced charges reach constant values already very close to the boundaries of the finite oligomers. This suggests that the interior of the chain will not be affected even after substantial reduction of the chain length. The illustration of such a behavior is given in Figure 4.9, which shows the distribution of the induced charge on the nitrogen atoms in a series of finite oligopyrroles. The nature of the chain interior is preserved even in the 10-mer, which is a little surprising since the central part of such a short chain might be expected to “remember” its molecular origin. The presented results show, however, that the evolution of the induced charges with the elongation of the oligomer chain is one of the most rapidly convergent properties among those studied in this work.

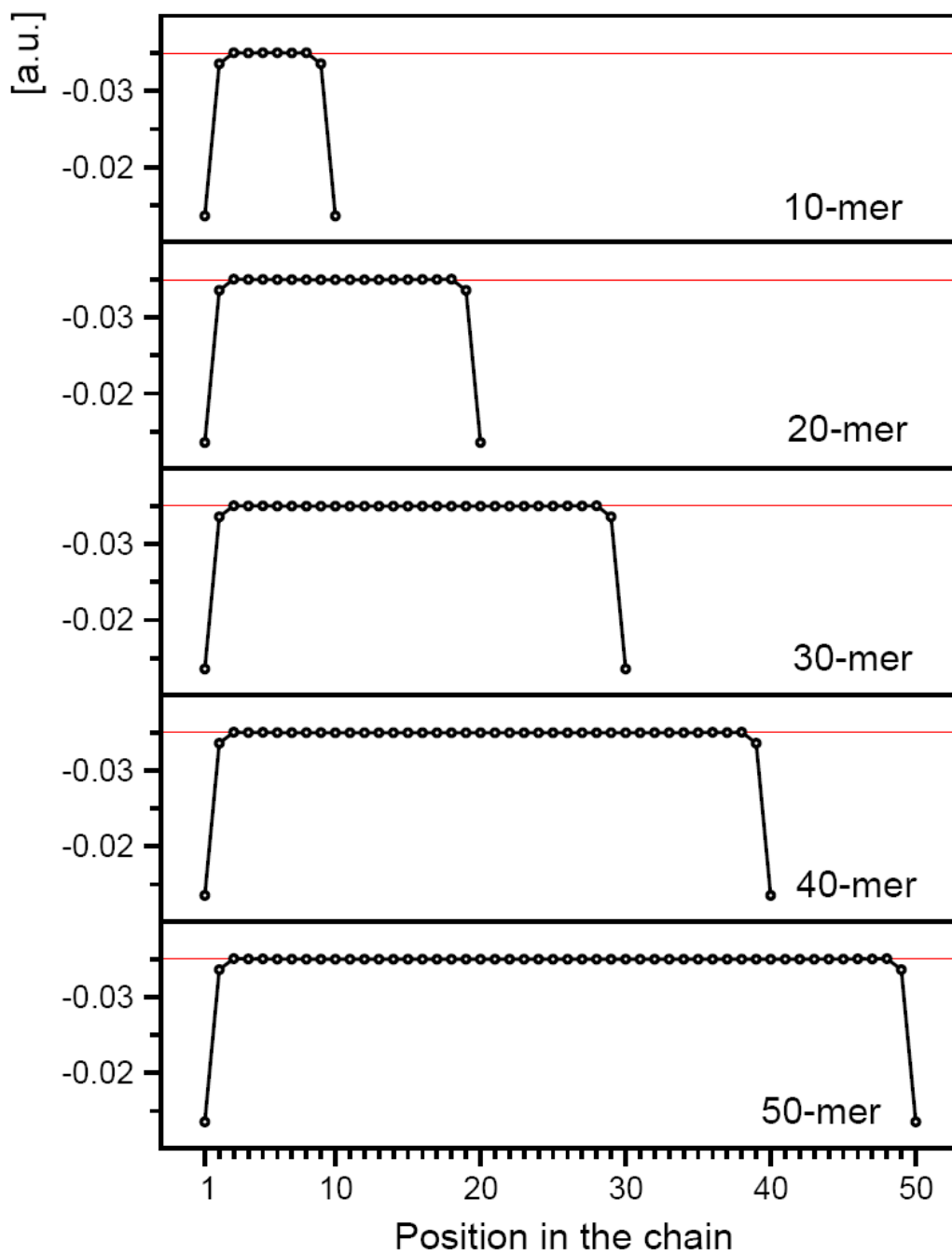


**Figure 4.9** The evolution of the induced charges on the nitrogen atoms in oligopyrroles. The value for polymer is given by the solid red line.

#### 4.1.5 Evolution of Dipole Moments

The oligomers built of an even number of monomers possess an inversion center (see Fig. 4.1) and therefore do not have any dipole moment. The situation is quite different for the oligomers with an odd value of  $m$ . The dipole moment in each of the considered monomers is oriented along the  $C_2$  symmetry axis. Adding another

monomer will result in another identical dipole oriented along the same direction but with the opposite sign. It is clear that in a dimer—and analogously also in longer oligomers with even  $m$ —these two dipoles cancel out yielding a non-polar molecule, which is consistent with the presence of the inversion center. In oligomers with odd  $m$  complete cancellation is impossible. A short reflection on the value of the dipole moment in oligomers with odd  $m$  shows that it should be comparable in magnitude to the dipole of a monomer. We have plotted the absolute values of the dipole moments as a function of  $m$  in Fig. 4.10. The presented plots look very much alike. The dipole moment is reduced upon the elongation by 0.01–0.15 D. This change is the most pronounced for short chains. For chains longer than 11 monomer units, the absolute value of the dipole moment is practically constant. These results show that the modulus of the dipole moment is a rapidly converging molecular property and the bulk value is obtained already for  $m > 11$ .

Note a certain logical difficulty rising from our results. The series of oligomers that consist of  $2m$  monomers is characterized by a lack of a permanent dipole moment (owing to the presence of the center of inversion), while the dipole moment of oligomers containing  $2m + 1$  monomer units converge to a non-zero value. However, in the infinite limit both series of oligomers should form the same polymer, the dipole moment of which vanishes due to symmetry reasons. Clearly, this is possible only for the series of even- $m$  oligomers, as the magnitude of the dipole moment for the odd- $m$  oligomers converges to a non-zero constant value (see Fig. 4.10). Apparently, the proper way to reproduce the dipole moment of the polymer by means of the oligomer approach requires using the *genuine* unit cell that contains two *trans*-connected rings (or *cis*-butadiene units). Such a unit cell has its own local centre of inversion and therefore, its dipole moment vanishes. This property is then naturally inherited by both the oligomers and the polymers constructed of such building blocks. The proper

repetitive unit of the polymer is thus different from the concept of the “monomer unit cell” commonly used in the oligomer approach. Still, many polymer properties, like the bond lengths or induced atomic charges, can be reproduced by using a single monomer as the building block. In other words, extrapolation of the monomer properties is sufficient for approaching the properties of the polymer.

It is important to mention here that dipole moments are defined within the framework of the SCC-DFTB method using a discrete summation over the induced Mulliken charges. Clearly this is not a very accurate approximation giving an average error of 0.5 debye.<sup>66</sup> In our calculations, the SCC-DFTB dipole moments for a single monomer of pyrrole, furan, thiophene, and cyclopentadiene are 2.13, 0.07, 0.38, and 0.50 D, respectively. The corresponding experimental values are 1.84, 0.66, 0.55, and 0.42 D.<sup>66</sup> The evolution of dipole moments with growing  $m$  does not introduce changes larger than 0.15 D, showing that the dipole moment of longer odd- $m$  oligomers can be well approximated by taking the SCC-DFTB value and correcting it for the difference to experiment for a single monomer.

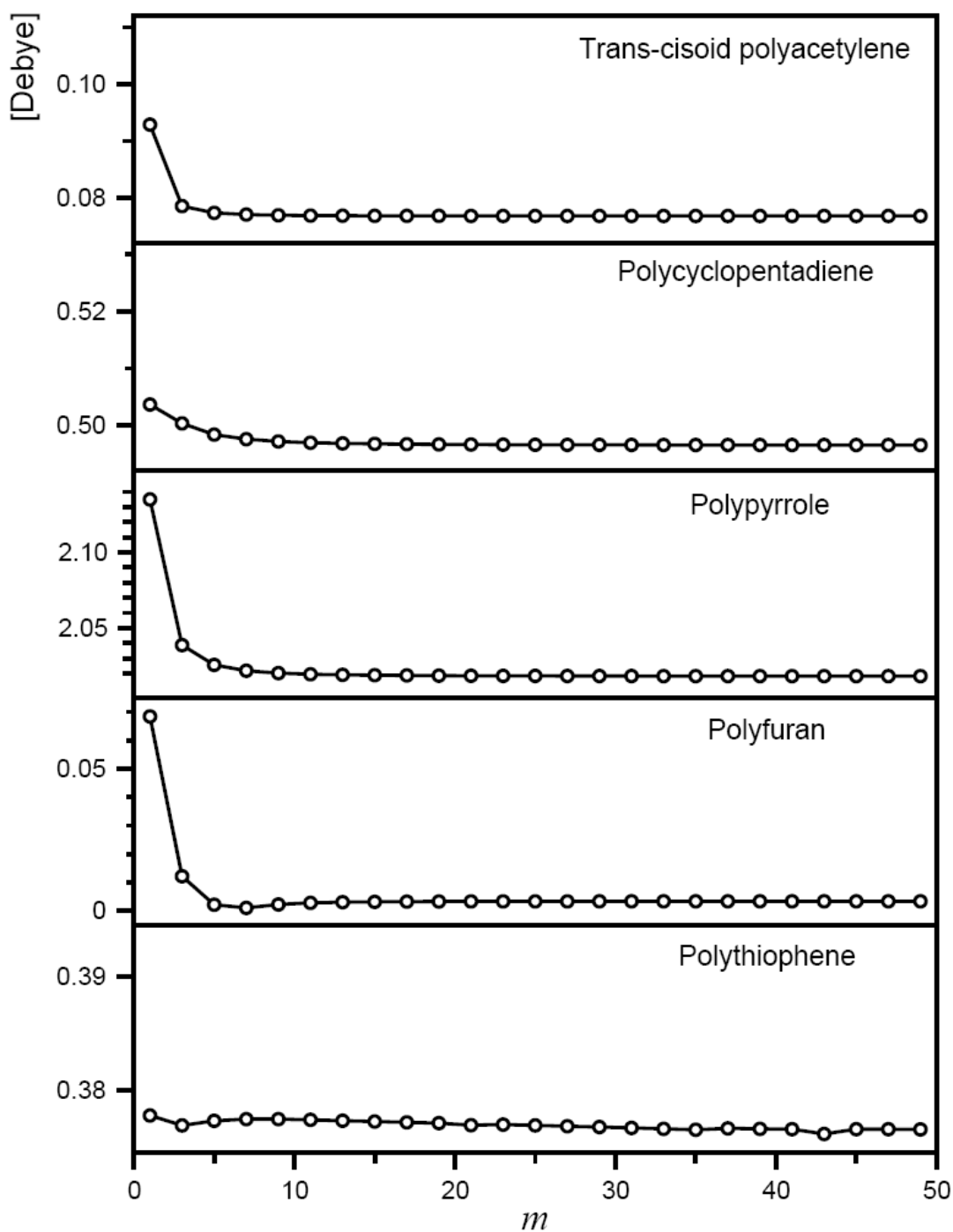


**Figure 4.10** Evolution of the dipole moments for all the considered models. Only the dipole moments of molecules with  $2m+1$  unit cells ( $C_{2v}$  symmetry) are shown.

#### 4.1.6 Evolution of Quadrupole Moments

The molecular quadrupole moment (QM) is a symmetric second rank tensor with



six independent components. Within the SCC-DFTB formalism, the QM tensor  $\Theta$  is defined via a discrete summation over the induced atomic charges

$$\Theta_{ij} = \sum_A^{\text{atoms}} \Delta q^A r_i^A r_j^A, \quad (4.1)$$

where  $\Delta q^A$  is the induced Mulliken charge on atom  $A$  and  $r_i^A$  and  $r_j^A$  are the Cartesian coordinates of the atom  $A$ . Note that owing to the discrete character of the charge distribution in the SCC-DFTB formalism, all the components of  $\Theta$  related to the  $z$  coordinate—i.e., the coordinate perpendicular to the plane of the studied molecules—are identically equal to zero<sup>67</sup> for all the studied systems except for polycyclopentadiene. Therefore, it is sufficient to investigate the evolution of the tensor components related to the products of the  $x$  and  $y$  coordinates only. Moreover, for the molecules possessing the  $C_{2v}$  point group symmetry, i.e., for all the oligomers built of odd number of monomers, it is required for symmetry reasons that  $\Theta_{xy} = 0$ . It is assumed that the molecular axis  $y$  coincides with the  $I_{\max}$  principal axis of tensor of inertia and the molecular axis  $x$  is the other in-plane principal axis of tensor of inertia.

The components of the QM tensor grow with the length of the investigated oligomers. To facilitate the comparison of this property for systems of different sizes, in Fig. 4.11 we show of  $\Theta_{xx}$ ,  $\Theta_{yy}$ , and  $\Theta_{xy}$  normalized by  $1/m$ . The reduced tensor components seem to approach constant values; this suggests that the dependence of the QM tensor components on the size of the system may become linear for sufficiently long oligomers. The convergence toward linearity is more pronounced and seemingly faster for  $\Theta_{xx}$  than for  $\Theta_{yy}$ . The result for  $\Theta_{xx}$  is not surprising, since its linear growth is a simple consequence of an increasing number of repetitive units. More complicated mechanism seems to be responsible for the relatively slow

convergence of  $\Theta_{yy}$  and  $\Theta_{xy}$ . We intend to address this issue in the oncoming paper.

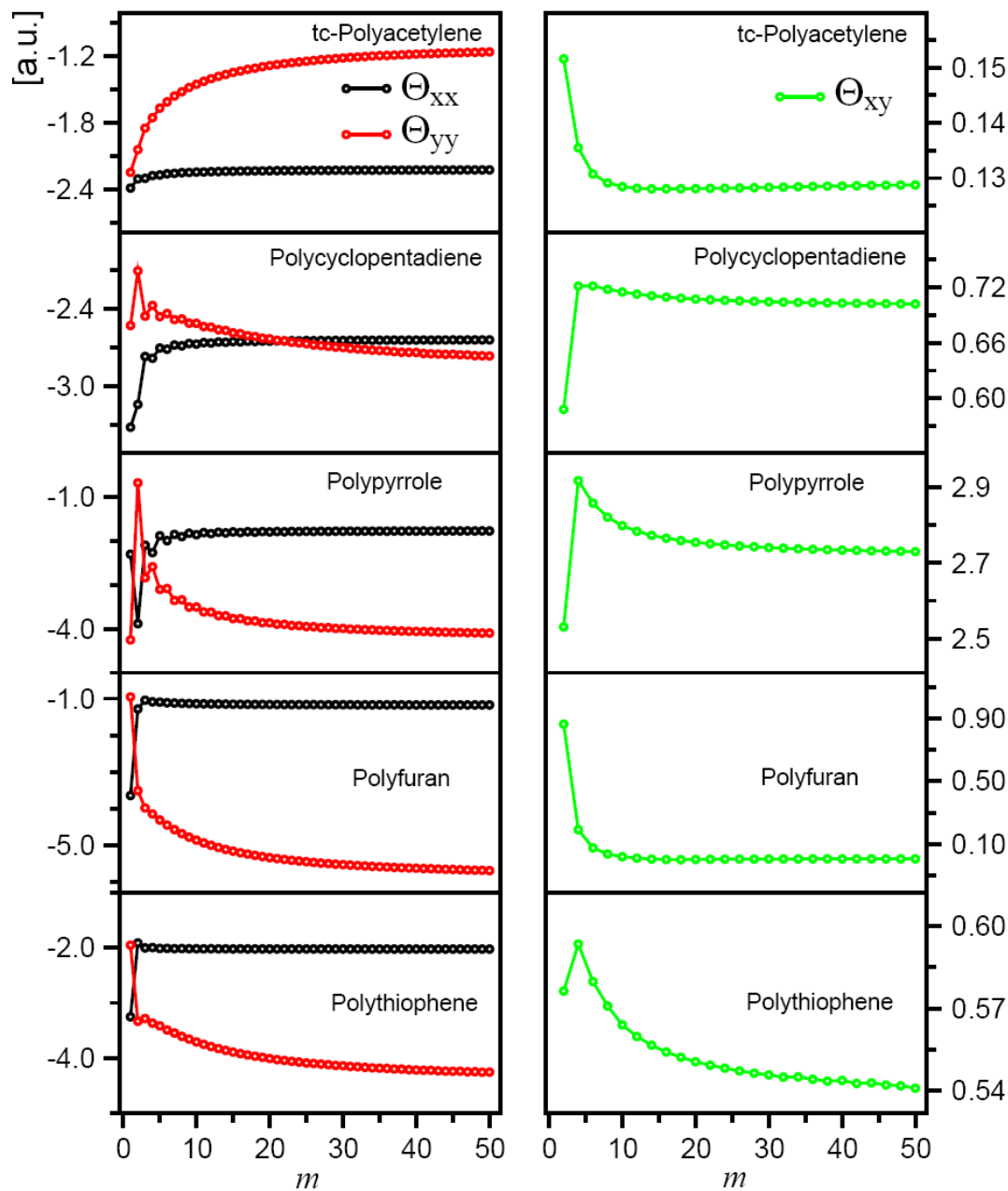
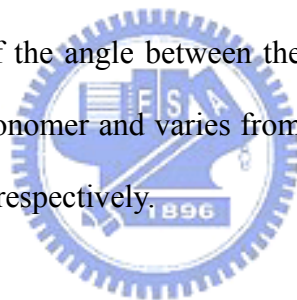


**Figure 4.11** Evolution of the quadrupole moment tensor components of all the considered models.

Another interesting observation for even- $m$  oligomers is significant discrepancy between the relative orientations of the principal axes of the tensor of inertia and the

principal axes of the QM tensor. For these systems, the molecular point group ( $C_{2h}$ ) does not determine any particular directions in the  $xy$  plane. Taking into account strong geometrical asymmetry of the molecule and the interpretation of quadrupole moment as a measure of deviations of the charge distribution from sphericity, one might expect that the principal axes of both tensors would be similar. However, our calculations show that this is not the case. On the one hand, the anisotropy of the tensor of inertia and the orientation of its principal axes are naturally rooted in the shape and size of the molecule. On the other hand, the molecular geometry does not seem to have a strong influence on the anisotropy and orientation of the quadrupole moment tensor. Even for the longest studied even- $m$  oligomers, the in-plane principal axes of the QM tensor do not coincide with the corresponding principal axes of the tensor of inertia. The value of the angle between the long axes depends strongly on the type of heteroatom in a monomer and varies from  $0.08^\circ$  to  $42.46^\circ$ , for the 50-mer of furan and cyclopentadiene, respectively.



#### **4.1.7 Evolution of Polarizabilities**

The molecular polarizability has been extensively studied for a variety of molecular systems.<sup>68-77</sup> In the case of oligomers and polymers, built from repeating units, the natural question was whether, or to what extent, the property can be regarded as additive. The problem is non-trivial since in oligomers, as well as in other types of molecular aggregates, a single monomer is influenced by the surrounding molecules. This influence can be particularly strong in case of the electrostatic properties, since the electrostatic forces give rise to long range interactions. Therefore, perfect additivity can only be achieved as long as the oligomer chain properties (such as geometry, induced charges or electron density) are constant in a large region of molecule with respect to a given monomer. Also, since the molecular polarizability

depends on the eigenstate energies and transition dipole moments of the whole molecule, these properties must be within their convergence limits before one may properly estimate the monomer contribution to the polarizability.

In the case of conjugated oligomers and polymers, the issue of polarizability as an additive property is even more complicated because of the large mobility of  $\pi$  electrons along the chain. This mobility is quantified by the so called conjugation length<sup>40</sup>, which sets the effective range in which the monomers can influence one another through the delocalized system of electrons. The conjugation length depends on a number of factors, such as the molecular geometry (especially the bond length alternation along the conjugated carbon chain), degree of aromaticity of the monomer units, and type of heteroatoms or substituents. As the mobility of  $\pi$  electrons greatly contributes to the strength of the electron density response to the applied electric field, it comes as no surprise, that it is the key factor determining the magnitude of molecular polarizability. The polarizability is thus linked to the conjugation length in the  $\pi$ -electron systems.

From the theoretical point of view, the conjugation length is extremely sensitive to the applied methodology; it is seriously underestimated in the HF based calculations and largely overestimated in the DFT calculations. Hybrid functionals, such as B3LYP<sup>78</sup> or B3PW86<sup>79</sup> offer a reasonable compromise, yet they also fail in reproducing such conjugation-dependent properties as vibrational frequencies of the Raman active modes in linear carbon chains.<sup>48,80,81</sup> Therefore, accurate calculations of polarizabilities for the  $\pi$ -conjugated, extended systems are not trivial and the results often bear considerable errors. Additionally, owing to the considerable the conjugation length, the molecular polarizabilities display very slow convergence with the length of the oligomers.<sup>82</sup> The size of systems required to reach the saturation limit makes such calculations very demanding. In order to circumvent technical difficulties, a number

of approaches were used, based either on the quantum calculations at various level of theory<sup>70,72-74,76,77,83</sup> or on more or less advanced physical models<sup>69,71,83-86</sup>. Owing to the slow convergence of the oligomer polarizabilities with the length of the system, a variety of extrapolation techniques had to be used<sup>69,71,72,77,85,87,88</sup> to estimate the monomer contribution to polarizability in the nearly infinite chain (additivity limit). The results of our calculations are in accordance with the reported behavior. Therefore, we adopt the formula of Schulz *et al.* (equation 3.1 on page 455)<sup>72</sup>, applied successfully for modeling the evolution of polarizabilities for eight different conjugated oligomers, and later also for carbon nanotubes.<sup>85</sup> We analyze the behavior of trace and anisotropy of the polarizability tensors, defined as:

$$\langle \alpha \rangle = \frac{1}{3}(\alpha_{xx} + \alpha_{yy} + \alpha_{zz})$$

$$\alpha_{ani} = \sqrt{\frac{1}{2}[(\alpha_{xx} - \alpha_{yy})^2 + (\alpha_{xx} - \alpha_{zz})^2 + (\alpha_{yy} - \alpha_{zz})^2] + 3(\alpha_{xy}^2 + \alpha_{xz}^2 + \alpha_{yz}^2)}, \quad (4.2)$$

as these invariants are of direct, practical importance in theories of optoelectronics and intermolecular forces. For the sake of clarity, we renormalize the aforementioned properties to values per monomer, so that they converge to a constant when the additivity limit is reached.

The results of our calculations are given in Figure 4.12. One can easily observe the convergent behavior of the polarizability invariants. However, careful scrutiny of the graphs, however, shows that saturation limits are not reached for none of the investigated systems.

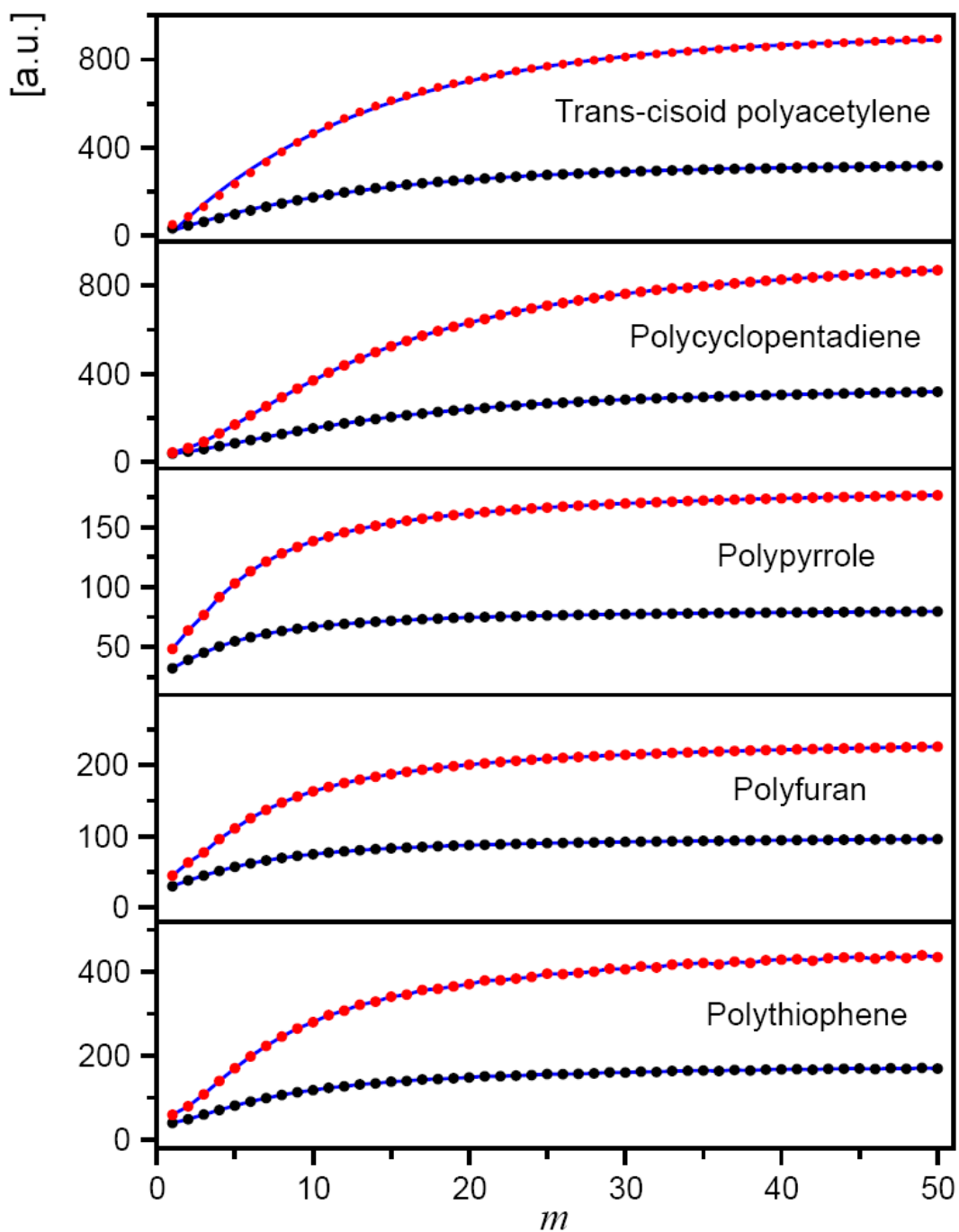


**Figure 4.12** Polarizability invariants of all the considered models. The blue curves are given according to the fitting formulas.

Also, the convergence appears to be faster for oligomers containing aromatic rings than for those built from non-aromatic monomers. In order to obtain the converged values of polarization we used the relation:

$$\alpha_m = \alpha_\infty - c \cdot \exp\left(-\frac{m}{m_{\text{sat}}}\right), \quad (4.3)$$

where  $\alpha_n$  denotes the polarizability per monomer as calculated for the  $m$ -mer, and  $\alpha_\infty$  stands for the analogous polarizability for infinite chain. The constant  $c$  for ideal case should be equal to  $\alpha_\infty$  as for  $n = 0$  the polarizability should also be zero. However, by allowing  $c$  to vary a better fit to the calculated data points can be obtained, and consequently, a more accurate value of  $\alpha_\infty$ . The parameter  $n_{sat}$  is a characteristic value of a given type of oligomers and is inversely proportional to the rate of convergence. It can thus be considered as a rough measure of the  $\pi$ -electron delocalization along the oligomer chain. The larger the value of  $n_{sat}$ , the more pronounced the conjugation length along the chain and the more reluctant the polarizability to converge. The optimum parameters of equation 4.3 are presented in Table 4.3.

**Table 4.3** The optimum parameters used in eq. 4.3

		$\alpha_\infty$ [a.u.]	$c$ [a.u.]	$m_{sat}$
<i>trans-cis</i> -polyacetylene	$\langle \alpha \rangle$	322	324	13.0
	$\alpha_{ani}$	910	967	13.1
<i>trans</i> -polycyclopentadiene	$\langle \alpha \rangle$	335	331	16.4
	$\alpha_{ani}$	922	987	16.7
<i>trans</i> -polypyrrole	$\langle \alpha \rangle$	78.5	51.4	6.9
	$\alpha_{ani}$	173.7	140.9	7.5
<i>trans</i> -polyfuran	$\langle \alpha \rangle$	94.5	71.7	8.0
	$\alpha_{ani}$	222.9	200.0	8.6
<i>trans</i> -polythiophene	$\langle \alpha \rangle$	168.8	144.5	10.0
	$\alpha_{ani}$	435.0	424.5	10.3

The extrapolated values of the average polarizabilities per monomer as well as of the polarization anisotropies clearly show that the studied systems can be divided into

two groups. Significantly larger values are associated with systems containing all-carbon monomers, namely *trans-cis*-polyacetylene and *trans*-polycyclopentadiene, while for the systems built of the heterocyclic units (pyrrole, furan and thiophene) the polarizabilities are relatively small. Also, the anisotropies of the polarizability with respect to the average values are much larger in the former group. Clearly, in the former group the longitudinal components of the polarizability tensor are more pronounced with respect to the transversal ones. It indicates that the all-carbon oligomers are characterized by the increased  $\pi$ -electron mobility along the oligomer chain, or larger conjugation length, as compared to the oligomers containing the heteroatoms. It is also reflected by the values of  $m_{sat}$  parameter, which are considerably larger for *trans-cis*-polyacetylene and *trans*-polycyclopentadiene than for the remaining systems.

The observed differences can be rationalized in terms of the aromaticity of the monomer units. On the one hand, the aromaticity of a given monomer is associated with a decreased intra-monomer bond length difference with respect to non-aromatic systems. Accordingly, the difference between the (averaged) intra-monomer bond length and the length of the bond linking monomers becomes more pronounced. Eventually, this leads to the increase of the band gap for polymers (HOMO-LUMO gap for oligomers) built from aromatic units. This in turn influences the polarizability, which in a crude approximation may be considered inversely proportional to the HOMO-LUMO, and consequently, should be lower for polymers containing highly aromatic building blocks. On the other hand, the electronic polarizability can also be interpreted in terms of molecular response to the external, uniform electric field, which brings about reorganization of the electronic density leading to polarization of the molecule. Aromaticity increases the electron confinement within the monomers and thus decreases the  $\pi$ -electron mobility along the oligomer chains and reduces the



molecular polarizability. This behavior manifests itself very clearly in our results. Interestingly, the polarizability of thiophene, which has similar degree of aromaticity as pyrrole<sup>76</sup> is considerably larger than the polarizability of the remaining aromatic systems. This effect can be attributed to the influence of the heteroatom; the large electronegativity of nitrogen and oxygen (3 and 3.5, respectively) gives additional contribution to the  $\pi$ -electron confinement within the monomers. The influence of sulphur is less pronounced, as sulphur has smaller electronegativity than the second row elements. Thus, the calculated polarizabilities for the studied oligomers reflect the basic chemistry of the conjugated systems. The actual values of polarizabilities, however, are more difficult to verify, as experiments are scarce and limited to very short oligomers. Also, direct comparison with experiment and other calculations is hindered by the inherent limitation of the SCC-DFTB method, according to which the polarizability component perpendicular to the molecular plane is equal to 0. SCC-DFTB uses a minimum valence basis to describe the behavior of valence electrons. Such a small basis does not have enough variational freedom to describe properly the behavior of the cloud of  $\pi$ -electrons when the field is perpendicular to the plane of the molecule. Despite its apparent simplicity, the SCC-DFTB performs remarkably well. Our average polarizabilities for 6-mers are by no more than 10% smaller than the values obtained by Delaere *et al.*<sup>76</sup> at the B3LYP/DZP level of theory, with one exception of polyacetylene, for which the average polarizability was underestimated by 22%. Also, the calculated values for the polarizability tensor in-plane components seem reasonable. The longitudinal polarizability per monomer, calculated for polypyrrole at the Hartree-Fock/6-31G\* level of theory using oligomer approach yielded 136 a.u.<sup>70</sup>. Analogous calculations based on couple-perturbed Hartree-Fock approach gave somewhat smaller value of 115 a.u. and 112 a.u. for polyfuran and polypyrrole, respectively<sup>83</sup>. Our calculations extrapolated to infinite

chains produced 241 a.u. for polyfuran and 191 a.u. for polypyrrole. Our values are clearly overestimated with respect to the HF values. However, the HF calculations are bound to yield too low polarizabilities owing to their serious overestimating of the band gaps, whereas DFT methodology gives too small band gaps<sup>83,89</sup> and overestimates the polarizabilities. Champagne *et al.*<sup>83</sup> showed that the longitudinal polarizability for 10-mer of acetylene computed with different methods vary from 101 a.u. for the CPHF approach to over 200 a.u. for pure DFT calculations. This proves how difficult it is to obtain accurate polarizabilities for conjugated systems. Also, in view of such large discrepancies, the SCC-DFTB results can be regarded as fair estimates of the oligomer (and polymer) polarizabilities available with very limited computational effort.

## 4.2 Raman Spectra of Nanodiamonds

Nanodiamond is an attractive material both for experimentalists and theoreticians.<sup>90</sup> Its potential applications are ultrathin and ultrahard antifriction coatings, optical coatings, and insulating or semiconducting layers in electronic devices.<sup>91,92</sup> Higher diamondoids were isolated in 2003<sup>93</sup>; this stimulated the characterization of nanodiamonds. The experimental Raman spectrum of a single crystal diamond has an unique triply degenerate  $T_{2g}$  peak appearing at  $1332\text{ cm}^{-1}$ . Several theoretical studies had been devoted to the Raman spectra of molecular diamond<sup>94,95</sup>. These works tried to find out the signature of the nanodiamond Raman spectra. The different goal of this work is to observe the evolution of the Raman spectra of diamond from the molecular level to the bulk scale, tracing the appearance of the unique  $1332\text{ cm}^{-1}$  peak. This study can be helpful for the future experimental also theoretical investigation of the Raman spectra of nanodiamond clusters.

Figure 4.13 presents the models being considered in the present study. Note that the

original space group of single crystal diamond is  $Fd3m$ , but owing to the missing inversion symmetry operation, it reduces to the  $T_d$  symmetry for molecular diamond. There are two distinct structures belonging to the  $T_d$  point group: octahedron and tetrahedron. In this study we chose both series of nanodiamonds. We saturate the surface carbon atoms with hydrogen atoms to stabilize the structure. For simplicity, new notations for these two series of diamonds have been made. Their molecular formulas and notations are listed in Figure 4.13. We call adamantane ( $C_{10}H_{16}$ ) as A; it is the smallest molecule in both octahedral and tetrahedral diamond series. By counting how many layers of “caves” in one tetrahedron formed by  $sp^3$  carbon networks in one molecule, we use symbols O2 to O8 to present the octahedral diamonds, and T2 to T10 for the tetrahedral diamonds. The temperature is set to be 25 °C and the laser frequency is 514.5 nm, which are corresponding to experimental environment for obtaining Raman intensity.

The SCC-DFTB Raman spectra are shown in Figure 4.14; we perform the DFT vibrational spectra calculations for selected molecules, A, O1, O2, O3, T2, T3, and T4. The BLYP density functional and 3-21G basis set are used for geometric optimizations and vibrational spectra calculation. For A and T2, we calculate the vibrational spectra using a larger 6-31+G\* basis set. Here we truncate the high frequency CH stretching signal from the spectra, because this signal will not appear in real experimental Raman spectra of single crystal diamond. At first glance, one can easily observe that the spectra from the two different methods show an overall agreement. Especially for the BLYP/6-31+G\* Raman spectra of A and T2, the agreement is even closer. The most significant deviation of the spectra is the peak at around  $1500\text{ cm}^{-1}$ . This signal corresponds to the CH scissoring mode. The deviation is probably due to that the SCC-DFTB repulsive parameters for the carbon-hydrogen pair is not accurate enough, the new optimization of these parameters is under process.

The other discrepant peak appears at around  $1150\text{ cm}^{-1}$ , this is a  $T_2$  CC waving mode. The discrepancy of the frequency is around  $50\text{ cm}^{-1}$ , which is within a reasonable range as reported in the previous benchmark.<sup>5</sup> These facts provide us with an evidence for the quality of the SCC-DFTB Raman spectra of larger nanodiamonds.

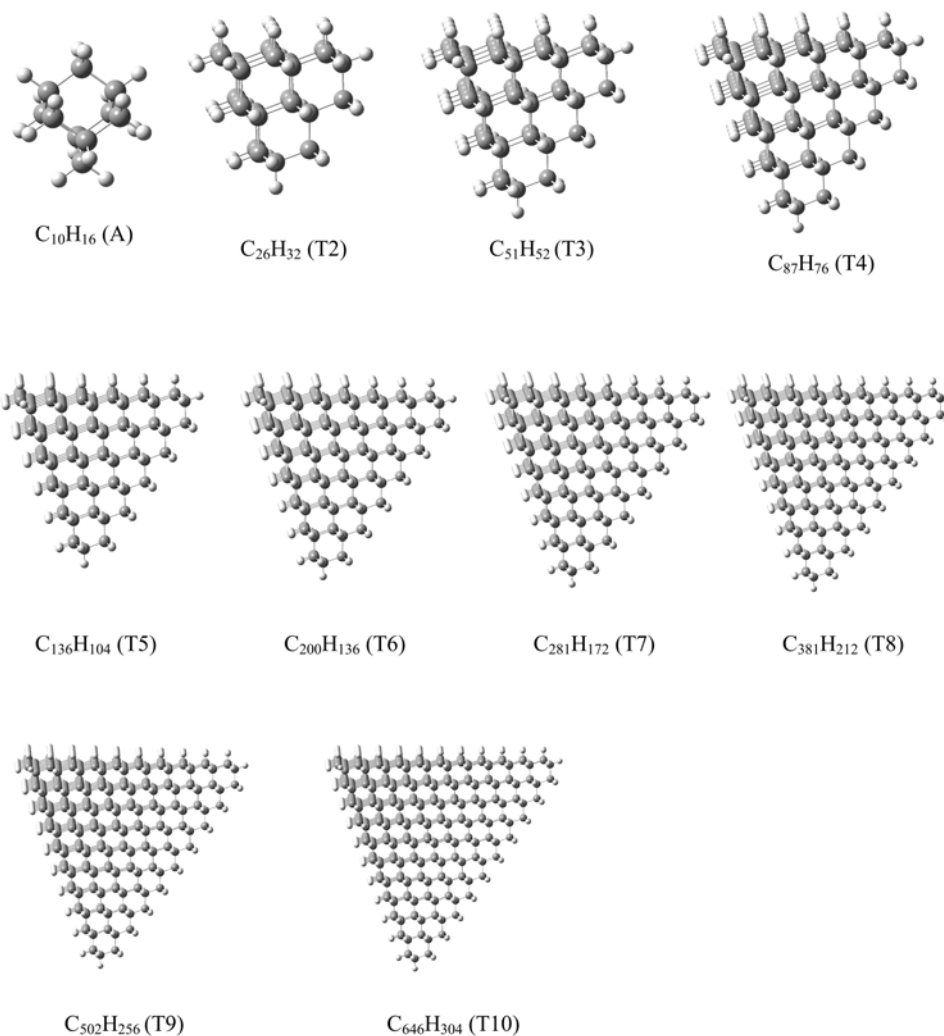
Further, the SCC-DFTB Raman spectra of both tetrahedral and octahedral diamonds are shown in Figure 4.15. As pointed out by Filik *et al*<sup>95</sup>, the peaks assemble into three groups. The lowest frequency group contains the  $A_1$  cage breathing mode. This mode is the peak that lowest in energy. As mentioned before<sup>95</sup>, this mode has been justified that it can not be a characteristic of nanodiamond Raman spectra. The second group of peaks explains that with the growing molecular size, the peaks get closer. If we go into more detail, as shown in figure 4.16, where we enlarge the spectra for the last three molecules of both series, the peaks belonging to  $T_2$  rise up at frequency around  $1200\text{ cm}^{-1}$ . Note that for the spectra of O6 ~ O8, there is not the misleading  $E$  symmetric band as in the spectra of tetrahedral nanodiamonds. The strongest peak in the spectra of O6 ~ O8 is of  $T_2$  symmetry. The mode of this peak is the CC-stretching mode, which is consistent to the mode at  $1332\text{ cm}^{-1}$  of the experimental Raman spectra of nanodiamonds. This mode is in fact slightly red-shifting with growing molecular size. But for the largest systems we had here, it is almost not moving.

We try to examine whether or not the present peaks on the Raman spectra are those we expect. As previously proposed by Negri<sup>96</sup> for polycyclic aromatic hydrocarbons (PAH), and Filik<sup>95</sup> for molecular diamonds, the mass of the terminating hydrogen atoms are artificially changed to 100 amu, which leads to a result that only the carbon atoms enclosed by the hydrogens are allowed to vibrate. This simulates the condition of the carbon atoms in a real crystal, and decouples the noisy signals caused by the CH vibrations within the same region of the CC stretching mode for real diamond crystal in the Raman spectrum. Following the same idea, we set the mass of the hydrogen atoms to be 10000 amu instead and repeat the SCC-DFTB vibrational

spectra calculations for all the diamond models, aiming to obtain the peak in the Raman spectra corresponding to the  $1332\text{ cm}^{-1}$  peak in the experimental Raman spectrum of bulky diamond. We term these diamonds “infinitely heavy hydrogens” (infH) diamonds. Only the modes related to carbon vibration are left in the infH spectra. Obviously, the peak of  $T_2$  symmetry  $\sim 1200\text{ cm}^{-1}$  shown in Figure 4.17 is the strongest signal in both series of infH diamonds.

In the end of this preliminary study, we present the infH Raman spectra that only contain  $T_2$ -symmetric modes. The spectra are given in Figure 4.18 and Figure 4.19. They give the evidence that the  $\sim 1200$  peak is almost solely from the  $T_2$  mode intensities. Although the present value of the frequency is  $\sim 130\text{ cm}^{-1}$  from the real experimental result. The theoretically calculated frequency of diamond Raman spectra had been shown that depend strongly on the method used.<sup>97</sup> At this stage, we can conclude that the  $1200\text{ cm}^{-1}$  is the SCC-DFTB signal of nanodiamond Raman spectra.

#### Tetrahedral diamond hydrocarbons



### Octahedral diamond hydrocarbons

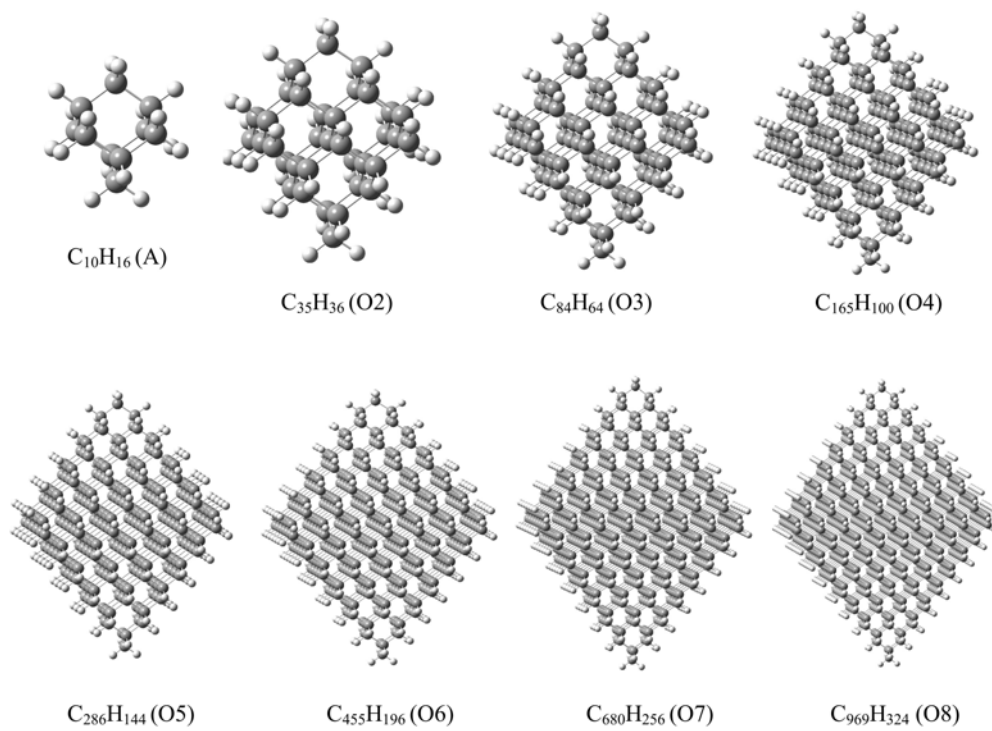
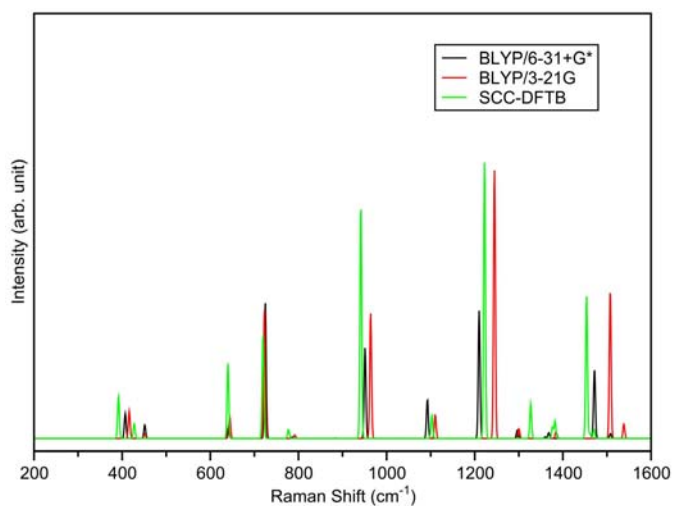
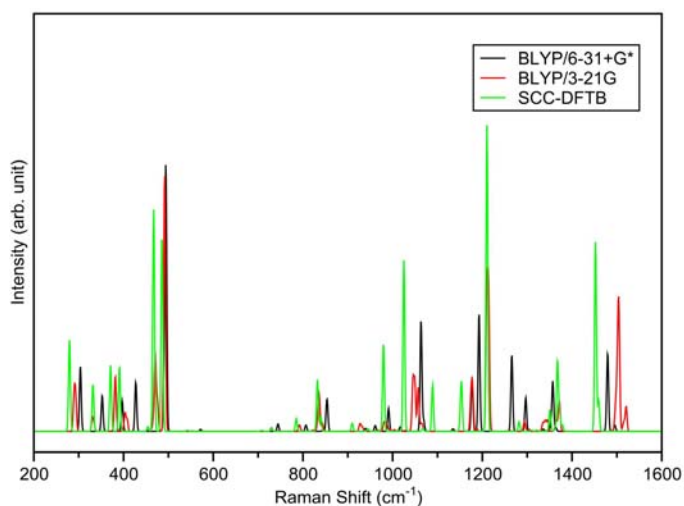


**Figure 4.13** The structures, molecular formula, and abbreviations of the tetrahedral and octahedral nanodiamonds.

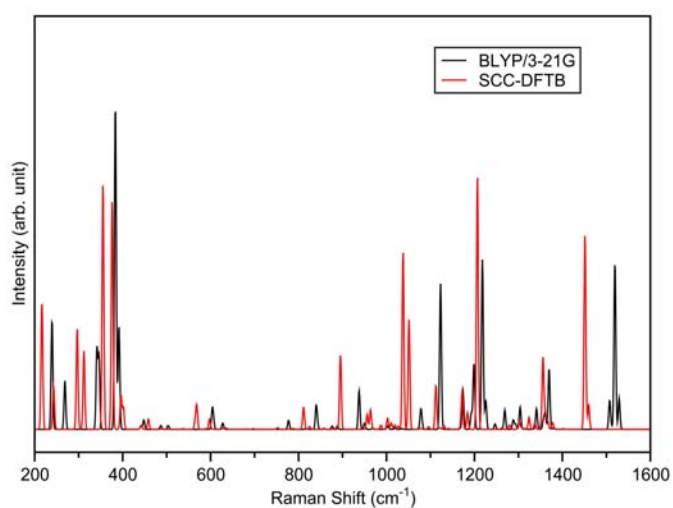
Raman spectra of A



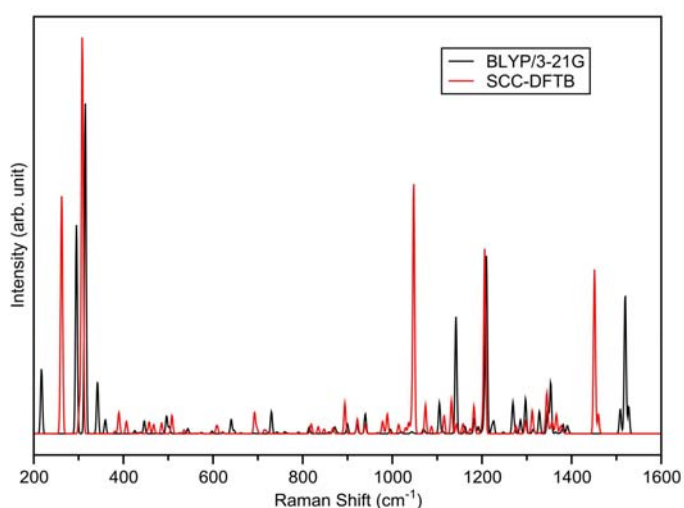
Raman spectra of T2



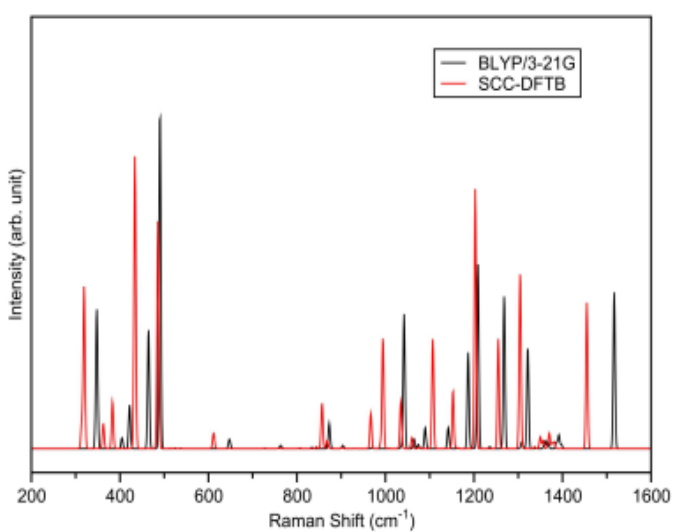
Raman spectra of T3



Raman spectra of T4



Raman spectra of O2



Raman spectra of O3

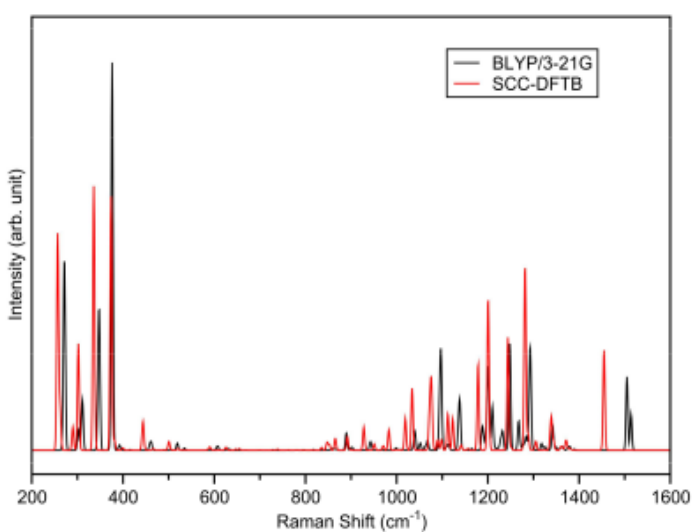


**Figure 4.14** Comparison of the Raman spectra calculated by BLYP/3-31G, SCC-DFTB, and BLYP/6-31G\* (A and T2 only).



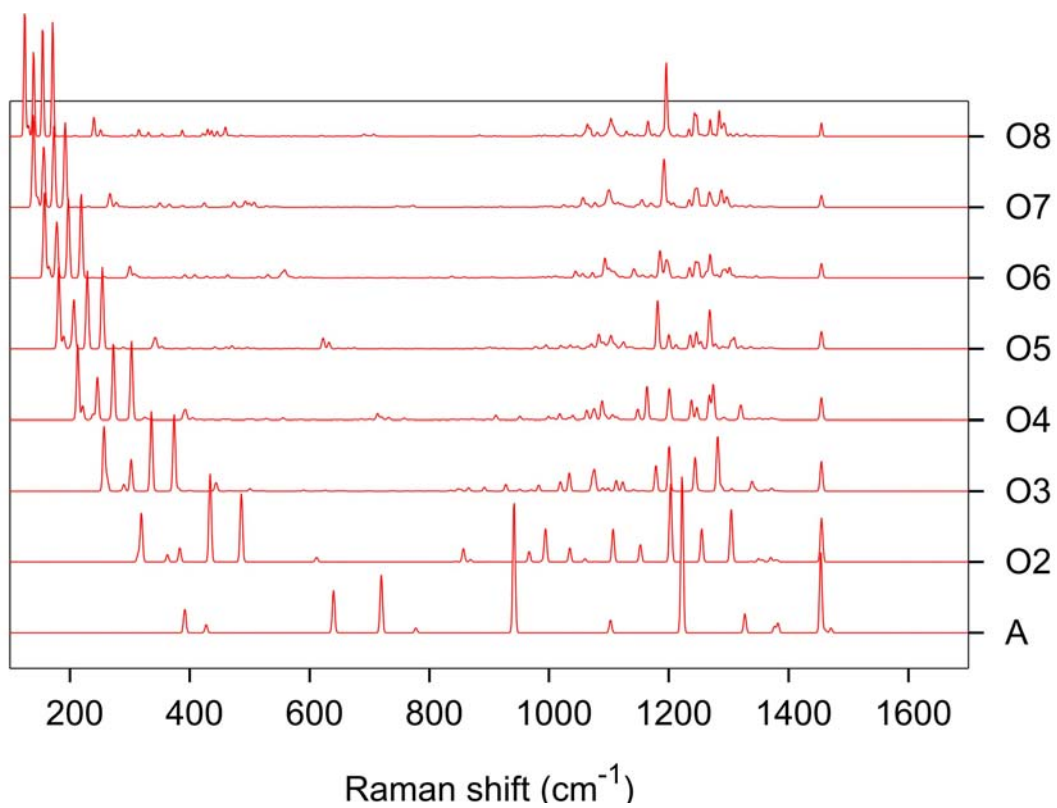
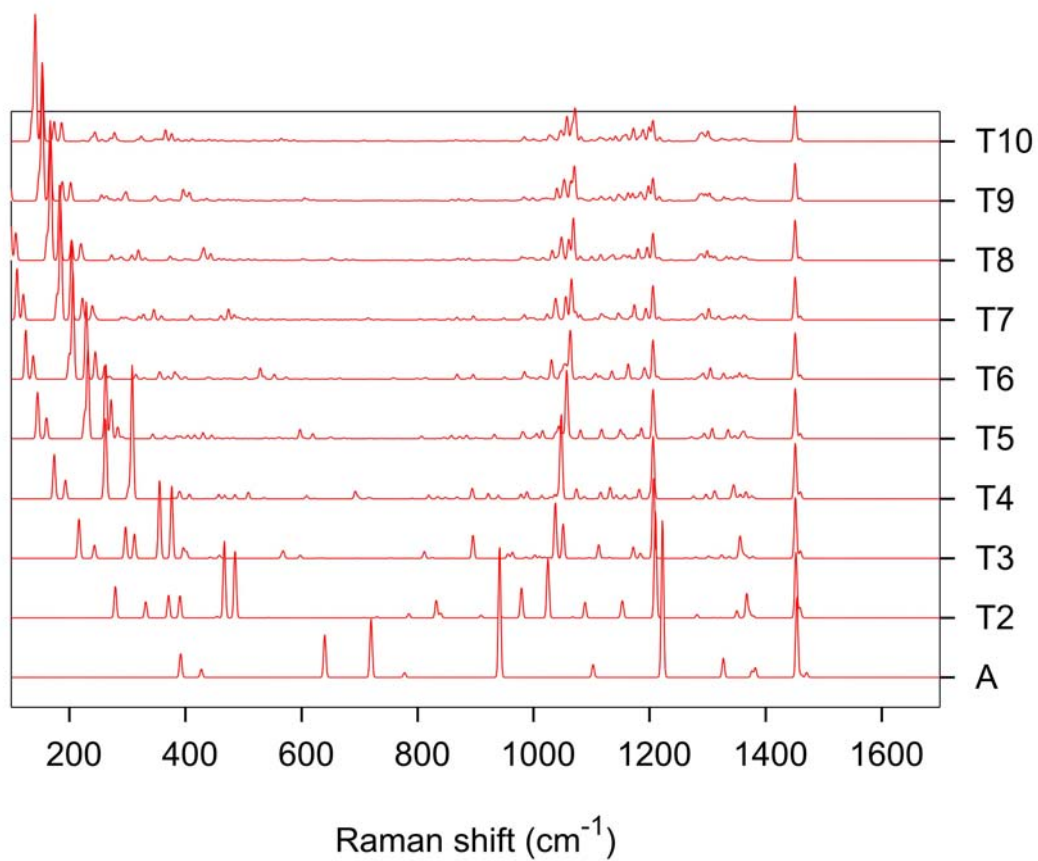
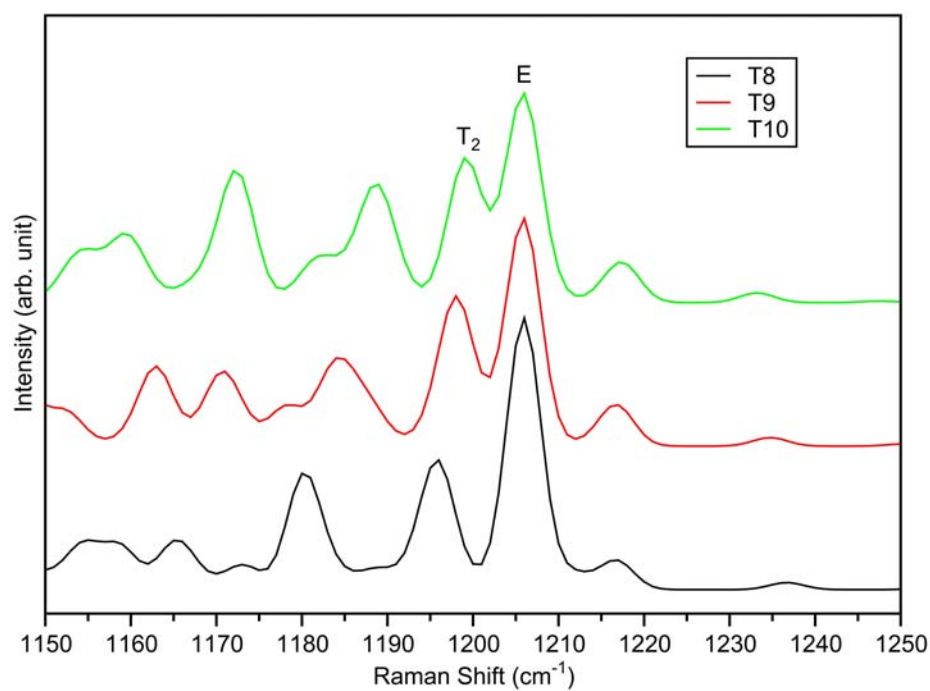


**Figure 4.15** The Raman spectra evolution with respect to the size of the tetrahedral and octahedral nanodiamonds.



### Raman spectra of T8~T10



### Raman spectra of O6~O8

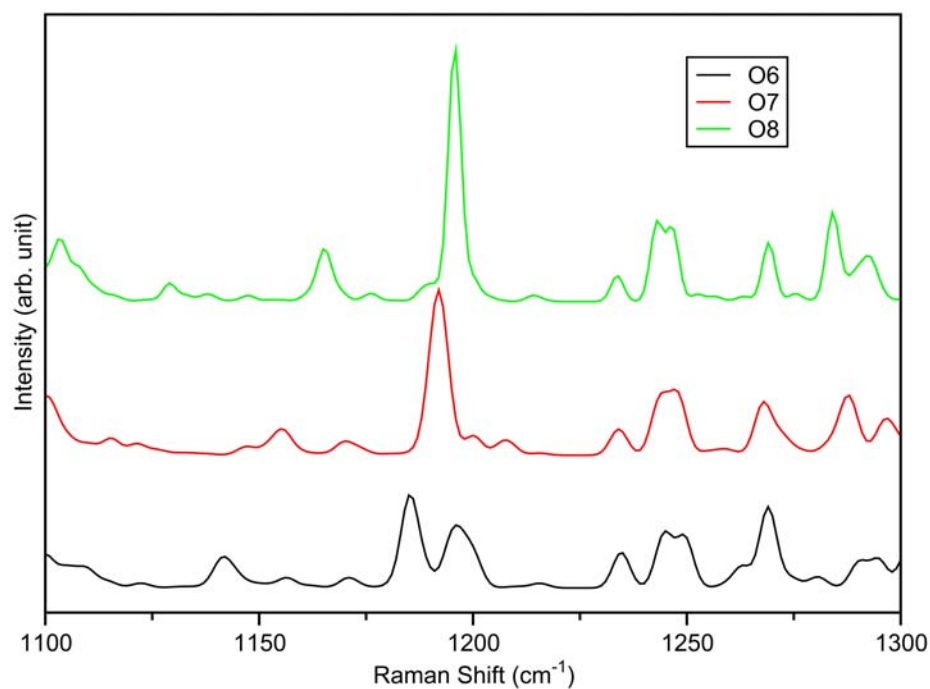


**Figure 4.16** The evolution of the  $T_2$  peak in the Raman spectra of the three largest nanodiamonds for tetrahedral and octahedral nanodiamonds.

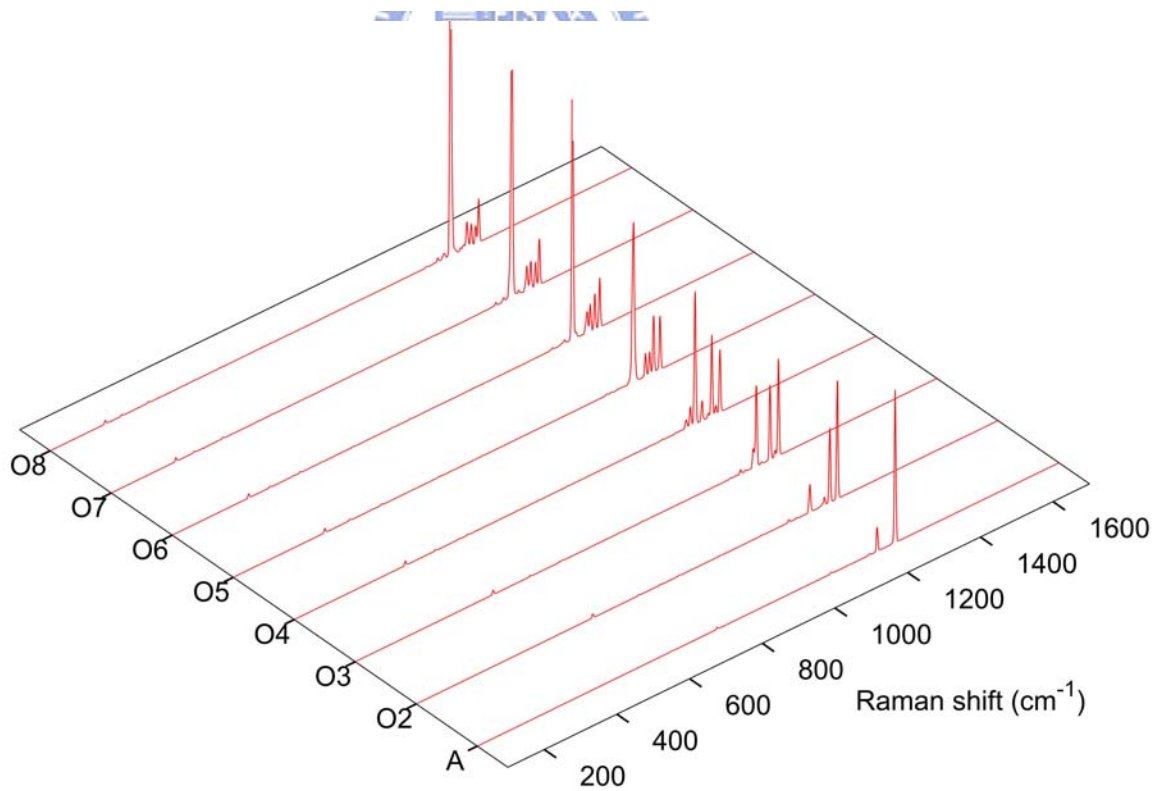
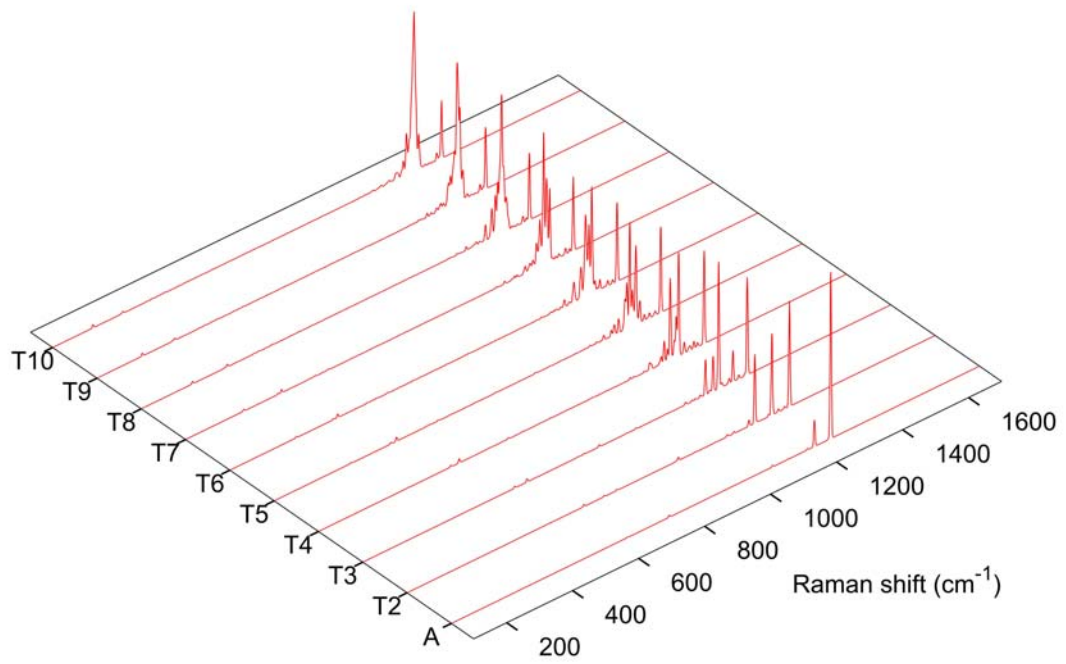


**Figure 4.17** The evolution of Raman spectra for both tetrahedral and octahedral nanodiamonds with “infH” case.

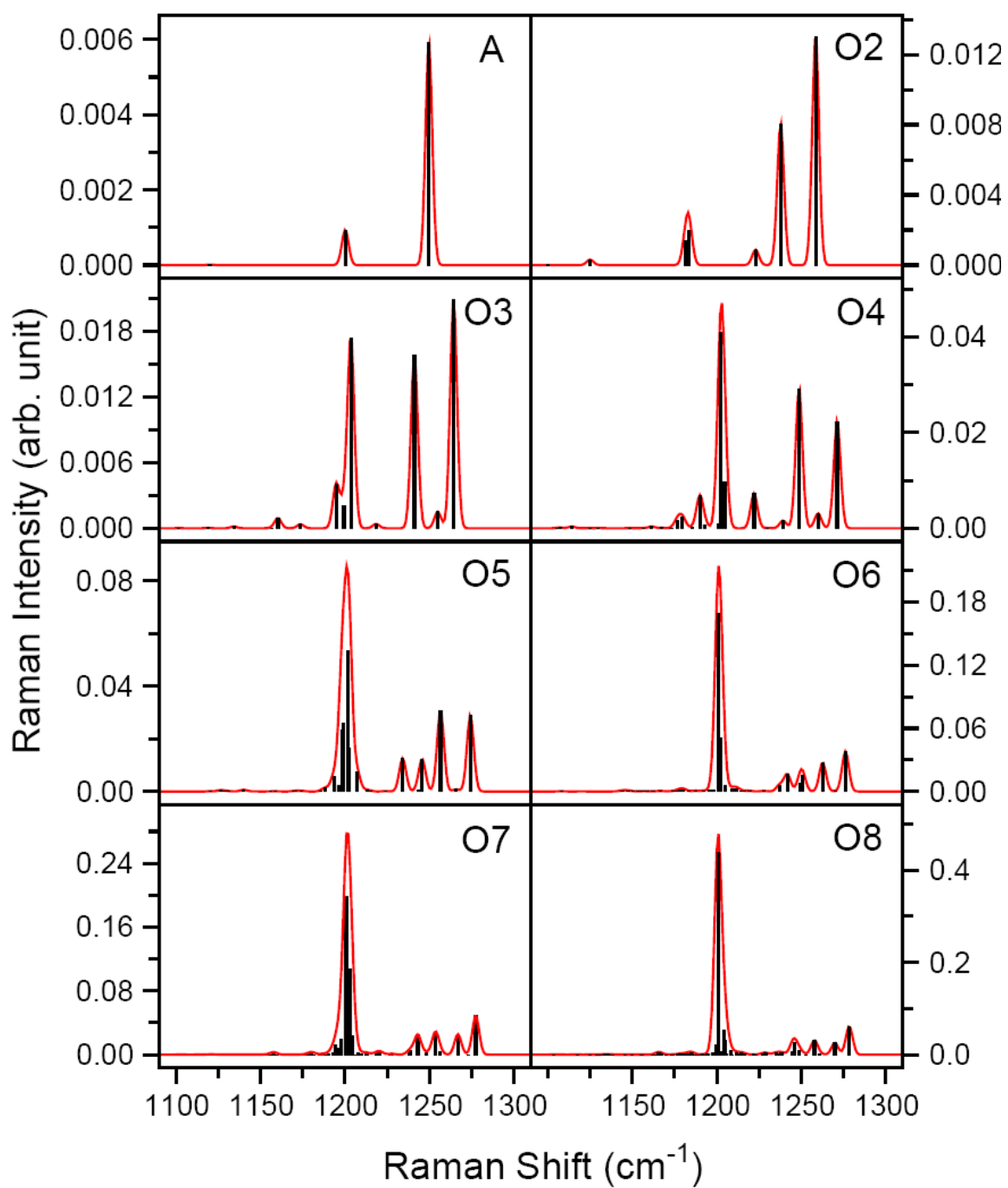


**Figure 4.18** The formation of the band at around  $1200\text{ cm}^{-1}$  of the “infH” tetrahedral nanodiamonds.

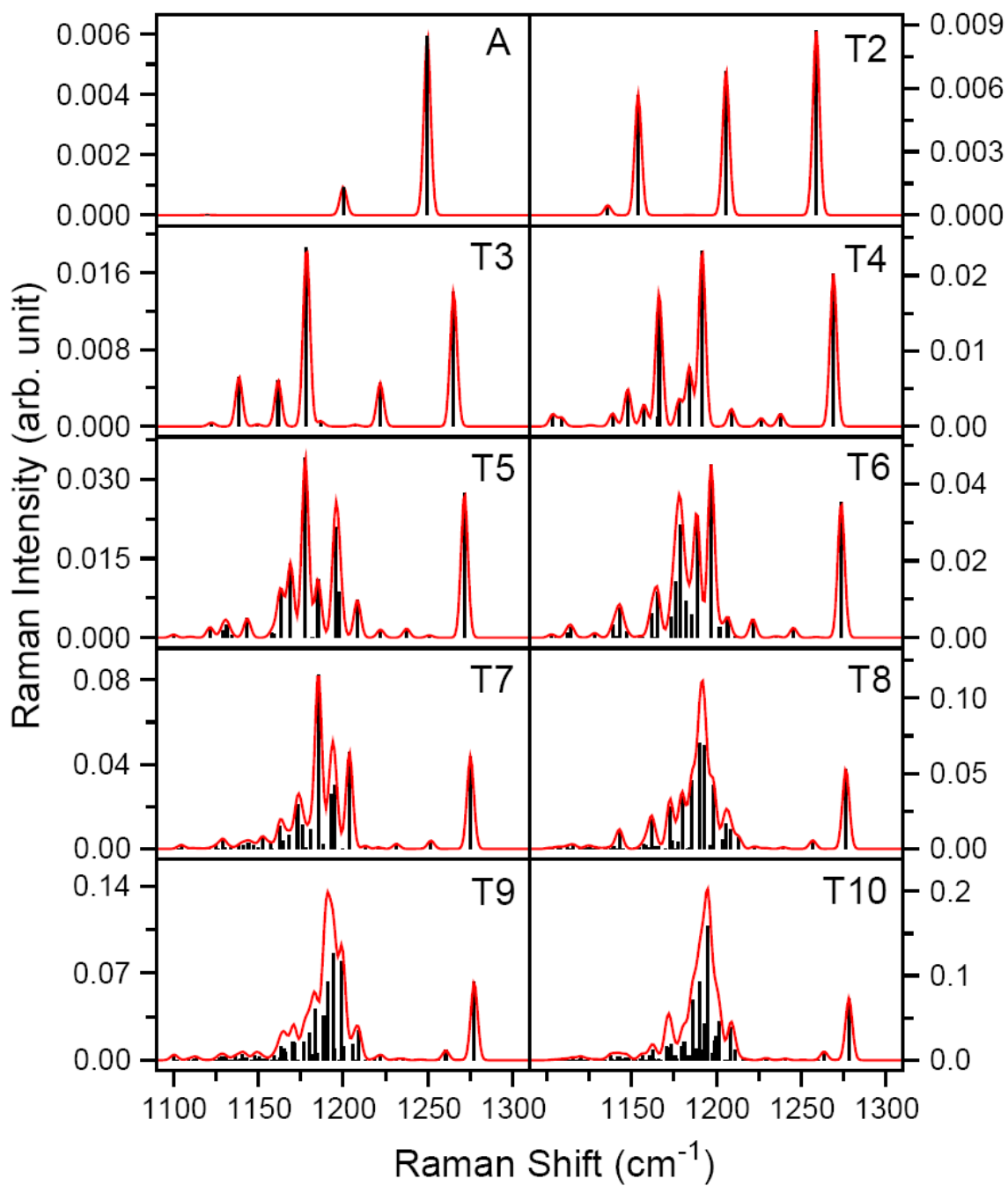


**Figure 4.19** The formation of the band at around  $1200\text{ cm}^{-1}$  of the octahedral nanodiamonds.

### 4.3 Polycyclic Aromatic Hydrocarbons (PAHs)

Raman spectra of the PAHs contain two characteristic peaks, one is called the D band at around  $1300\text{ cm}^{-1}$ , the other one at about  $1600\text{ cm}^{-1}$  is called G band.<sup>7</sup> The D band results from the defects or disorder in the sample. The G band is so-named because it is the only feature observed in the first order Raman spectra of highly ordered graphite crystal. The vibrational mode is of  $A_{1g}$  symmetry and is the aromatic ring breathing mode for the D band, while the mode for the G band is the  $E_{2g}$  CC-stretching vibration, as shown in Figure 4.20

Several studies concentrate on the theoretical capturing of these two modes and discuss their intensity ratio (D/G ratio).<sup>7,96,98-100</sup> This enables the characterization of the Raman spectra for the presence of the  $sp^2$  carbons in the specimen. The research groups obtain the molecular Raman spectra of the PAHs and try to extract the solid-state like characteristics.

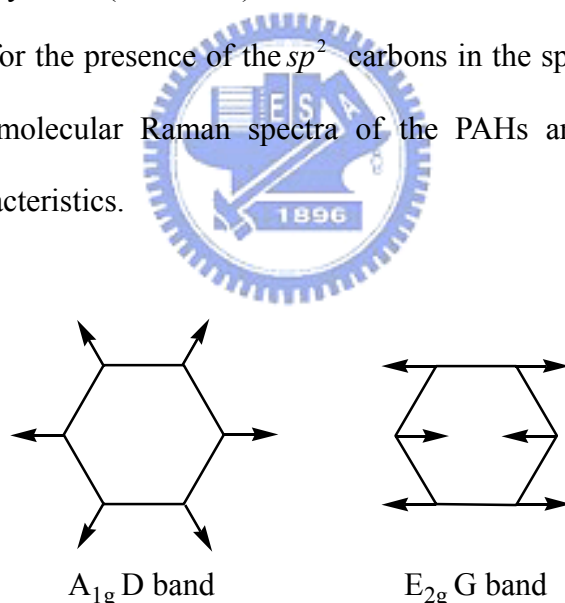


**Figure 4.20** The symmetries and vibration vectors of the D band and G band in Raman spectra of PAHs.

In this study, we try to get the solid-state like characteristics with much larger systems. Two series of PAHs have been done, one is the usual graphene flakes, and the other is the so-called hexa-peri-benzacoronenes (HPBs). They can be distinguished by the different peripheries. The margins of graphenes are of the zig-zag

form, while those of HPBs are of armchair form. Both series have the symmetry point group  $D_{6h}$ . We name these two series of PAHs in a simple way. We name graphenes as  $C_n$ , where  $n$  is the number of the layers surrounding the central benzene ring. HPBs are called  $B_m$ , where  $m$  presents the number of benzene rings from the center to the margin, the central benzene is excluded. The molecules being considered are listed in table 4.4 and also the examples of nomenclature in figure 4.21 for  $C_3$  and  $B_3$ .

**Table 4.4** Abbreviations, molecular formula, and number of atoms for Graphenes and HPBs.

Graphenes			HPB		
	molecular formula	# of atoms		molecular formula	# of atoms
C1	C <sub>24</sub> H <sub>12</sub>	36	B2	C <sub>42</sub> H <sub>18</sub>	52
C2	C <sub>54</sub> H <sub>18</sub>	72	B3	C <sub>114</sub> H <sub>30</sub>	144
C3	C <sub>96</sub> H <sub>24</sub>	120	B4	C <sub>222</sub> H <sub>42</sub>	262
C4	C <sub>150</sub> H <sub>30</sub>	180	B5	C <sub>366</sub> H <sub>54</sub>	420
C5	C <sub>216</sub> H <sub>36</sub>	252	B6	C <sub>546</sub> H <sub>66</sub>	612
C6	C <sub>294</sub> H <sub>42</sub>	336	B7	C <sub>762</sub> H <sub>78</sub>	840
C7	C <sub>384</sub> H <sub>48</sub>	396	B8	C <sub>904</sub> H <sub>90</sub>	1104
C8	C <sub>486</sub> H <sub>54</sub>	540			
C9	C <sub>600</sub> H <sub>60</sub>	660			
C10	C <sub>726</sub> H <sub>66</sub>	792			
C11	C <sub>864</sub> H <sub>72</sub>	936			
C12	C <sub>1014</sub> H <sub>78</sub>	1092			
C13	C <sub>1176</sub> H <sub>84</sub>	1260			

The structures of the HPBs are not flat anymore after  $B_3$ , this fact was found because we obtained imaginary frequencies thereafter. The imaginary modes vibrate along the non-planar mode. The re-optimization along the imaginary mode gives us a new geometry as shown in Figure 4.22 for  $B_3$ . Although the HPBs are non-planar, we still set them as planar in this study, because the energy difference in energies of both

conformations are small (the difference in energy is 0.0007 Hartree and the imaginary frequencies are -9.470i, 9.473i and 9.613i for B3 ). Two of the opposite apices raise up in these deformed geometries, this is thought to avoid the repulsion between the armchair peripheries. The same situation can be seen for the non-planar structure of poly-para-phenylene (PPP). The deformation leads the molecular symmetry to reduce from  $D_{6h}$  to  $C_2$ . An example of the deformed structure is shown in Figure 4.21 for B3.

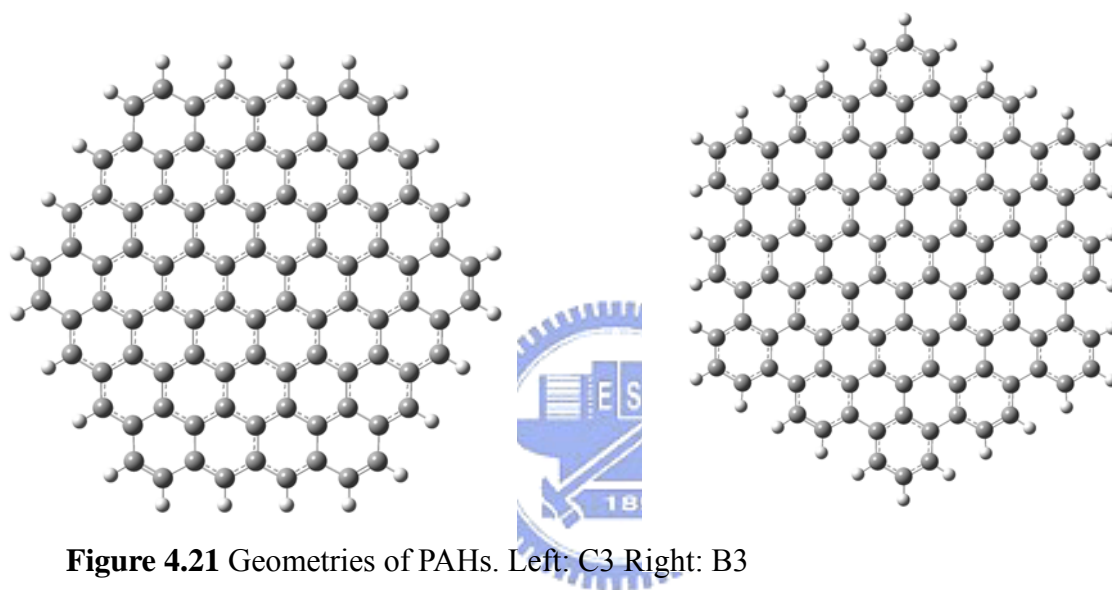


**Figure 4.21** Geometries of PAHs. Left: C3 Right: B3



**Figure 4.22** The deformed B3 obtained by optimization along the imaginary vibration mode.

For comparison of the vibrations of the  $sp^2$  carbon, we also performed the infH Raman spectra for graphenes and HPBs. We set the mass of hydrogen atoms as 10000 amu, which is the same as in the diamond study.

As for diamond, the SCC-DFTB spectra are examined by comparing them with

the BLYP/3-21G results for small molecules, C3 and C4. Figure 4.23 shows the comparison. As we can see, despite of the discrepancy happens  $\sim 1200 \text{ cm}^{-1}$  which correspond to the singly degenerate mode of CH waving, the other parts show satisfactory accordance.

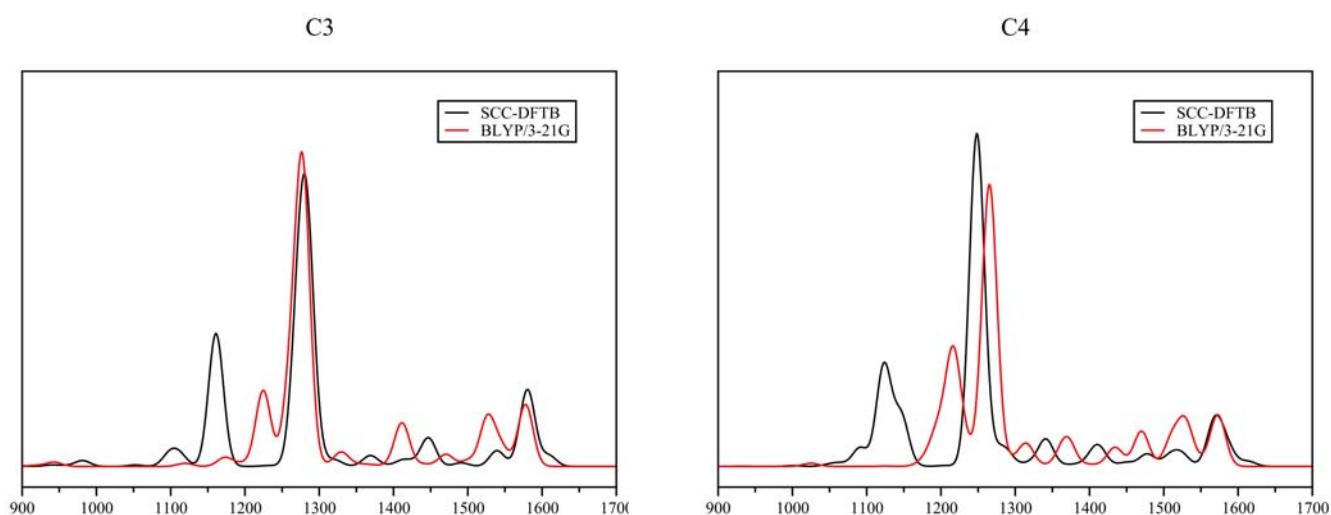


**Figure 4.23** Comparison of the SCC-DFTB and BLYP/3-21G Raman spectra of C3 and C4.



Currently, we have obtained the all the Raman spectra of PAHs terminated with normal hydrogen atoms except the one of C11. The Raman spectrum of C11 suffers numerical instability which is caused by the numerical differentiation of polarizability tensor respect to external electric field. We are working on different values of electric fields for obtaining more accurate spectrum of C11. The spectra are shown in Figure 4.24



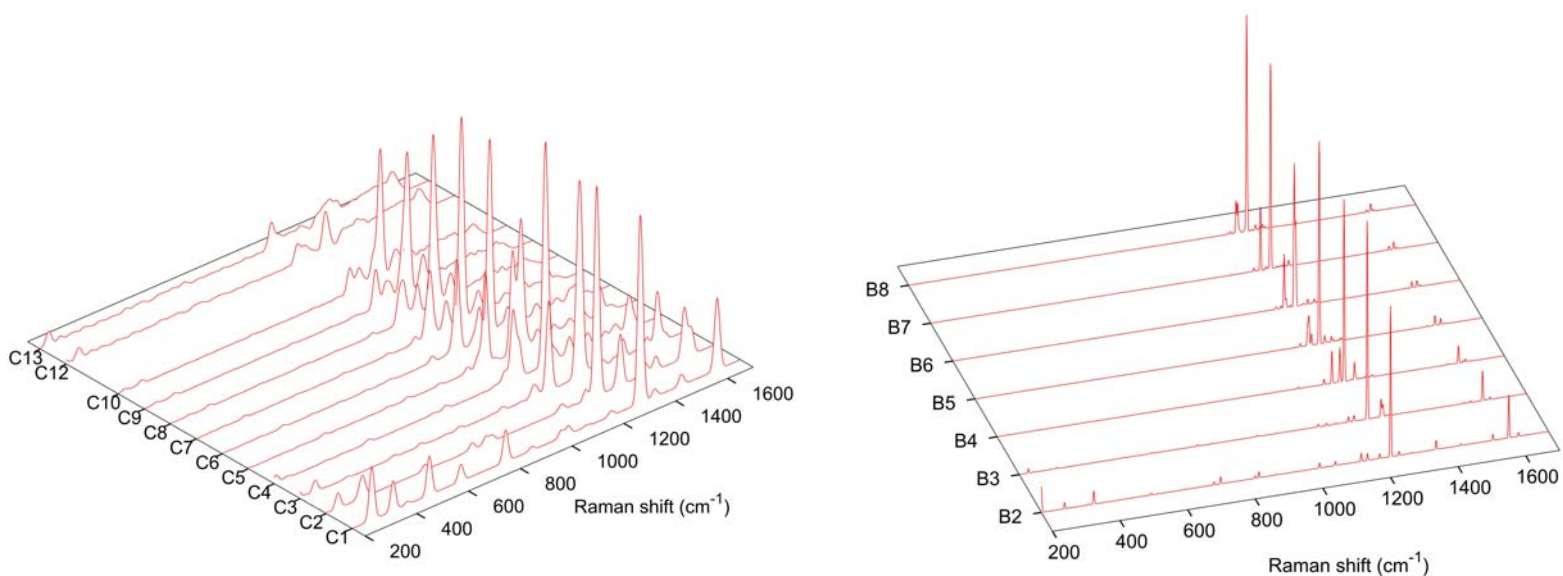


**Figure 4.24** Evolutions of Raman spectra of both graphenes and HPBs.

In Figure 4.24, there are some common features for both graphene flakes and HPBs. The  $\sim 1200 \text{ cm}^{-1}$  peaks are the  $A_{1g}$  bands and they are the most intensive peak in these spectra. The  $\sim 1600 \text{ cm}^{-1}$  peak of  $E_{2g}$  symmetry is keeping decaying with growing flake size. Worthy to note is that the drastic intensity drop of the  $A_{1g}$  bands, occurs after C10 in graphene Raman spectra, indicates that it is at the critical point of the D/G ratio change as presented by Ferrari *et al.*<sup>7</sup>

For the infH Raman spectra, the spectra of C11 and B8 is still under calculation in Figure 4.25. Detailed analysis on these spectra is needed for us to investigate the correspondence of the vibrations of the  $sp^2$  carbons in bulky environment and in molecular surroundings.

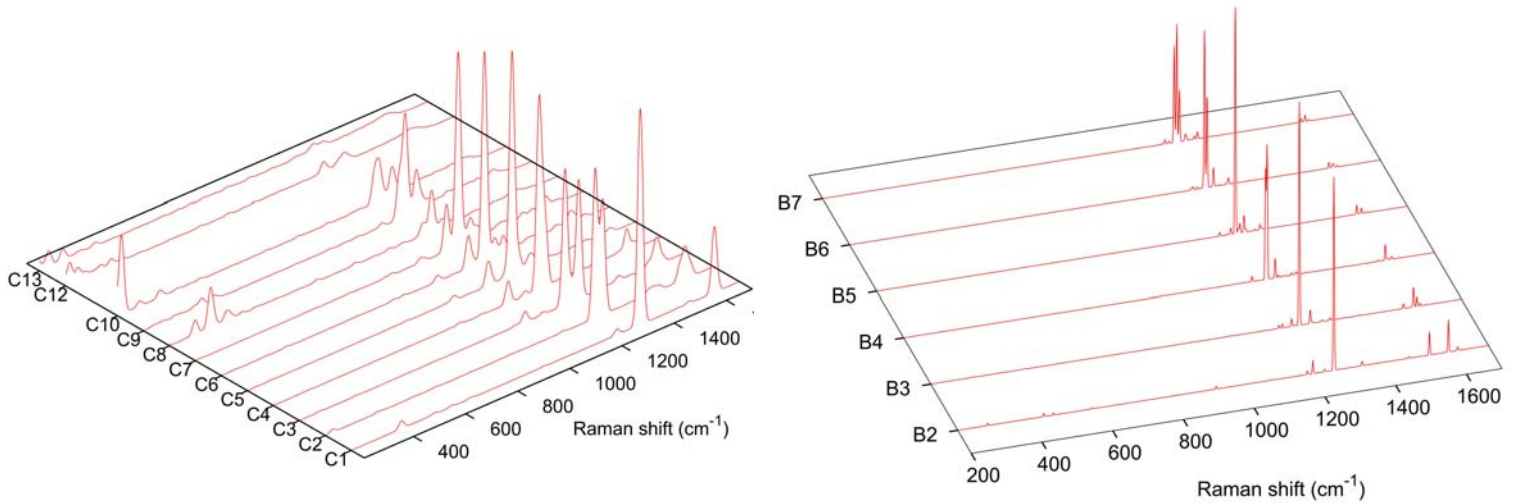
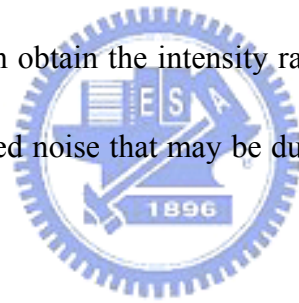


**Figure 4.25** The evolutions of Raman spectra of “infH” graphenes and HPBs.

To obtain the D/G ratio, we used the projector method to select only the  $A_{1g}$  and  $E_{2g}$  modes. Thus we can obtain the intensity ratio of the spectra. But presently the results still have unexpected noise that may be due to the spline fitting bug of the SCC-DFTB repulsive energy.



## 4.4 Icosahedral Fullerenes

### 4.4.1 Geometrical Description of Icosahedral Fullerenes

Graphene sheets are composed of hexagonal rings of  $sp^2$  hybridized carbon atoms. It is possible to curve the graphene sheets by introducing pentagonal rings so as to form closed cages known as fullerenes.  $C_{60}$ , the most early found and possibly most famous member in the fullerene family, was discovered in 1985 by Kroto *et al.*<sup>101</sup> Among the various symmetries of fullerene cages differ in morphology and size, icosahedral fullerenes are the most highly symmetric ones. The general rule of making icosahedral fullerenes had already been described in detail.<sup>102,103</sup> Here we just

briefly review the rule. An icosahedron is formed by the equilateral triangles as building blocks. If the edges of the equilateral triangle differ, different kinds of icosahedral fullerenes will be made. In 1937, Goldberg<sup>104</sup> showed that the number of vertices  $v$  in polyhedra of icosahedral symmetry can be related to two integers  $m$  and  $n$  ( $0 < m \geq n \geq 0$ ) by the *Goldberg equation*:

$$v = 20(m^2 + mn + n^2)$$

$v$  here is regarded as the number of carbon atoms (we denote  $N_c$ ) in a fullerene,  $m$  and  $n$  show the lattice point  $(m,n)$  on a graphene sheet.<sup>103</sup> The procedure of forming an graphitic onion are putting the first graphene sheet with centered origin  $(0,0)$ . The second pentagonal ring is located next to this origin, and we place another pentagonal ring next to the lattice point  $(m,n)$ . Finally, we put the third pentagonal ring equilaterally with respect to the other two rings. This procedure generates a equilateral triangle as the building block of the icosahedral fullerenes. If the edge of the triangle is in the armchair form, then the resulting fullerene is of full  $I_h$  symmetry. In generalization, all the graphitic onions formed in the way described above can be classified into three families:

(1)  $I_h$  symmetry (armchair) if  $m=n$

$$N_c = 60n^2$$

$n$	1	2	3	4
$N_c$	60	240	540	960

(2)  $I$  symmetry (helical arrangement) if  $m = n + 2$

$$N_c = 20(3n^2 + 6n + 4)$$

$(m,n)$	(2,0)	(3,1)	(4,2)	(5,3)
$N_c$	80	260	560	980

(3)  $I$  symmetry (helical arrangement) if  $m = n + 1$

$$Nc = 20(3n^2 + 3n + 1)$$

$(m,n)$	(2,1)	(3,2)	(4,3)	(5,4)
$Nc$	140	380	740	1220

Here we show the  $I_h$  symmetric fullerenes. Fullerene  $C_{60}$ ,  $C_{240}$ ,  $C_{540}$ ,  $C_{960}$  have been chosen. Their SCC-DFTB optimized geometries are shown in Figure 4.26 along the principal  $C_5$  axis. Note that the size of each cage is not plotted according to the real geometrical ratio.

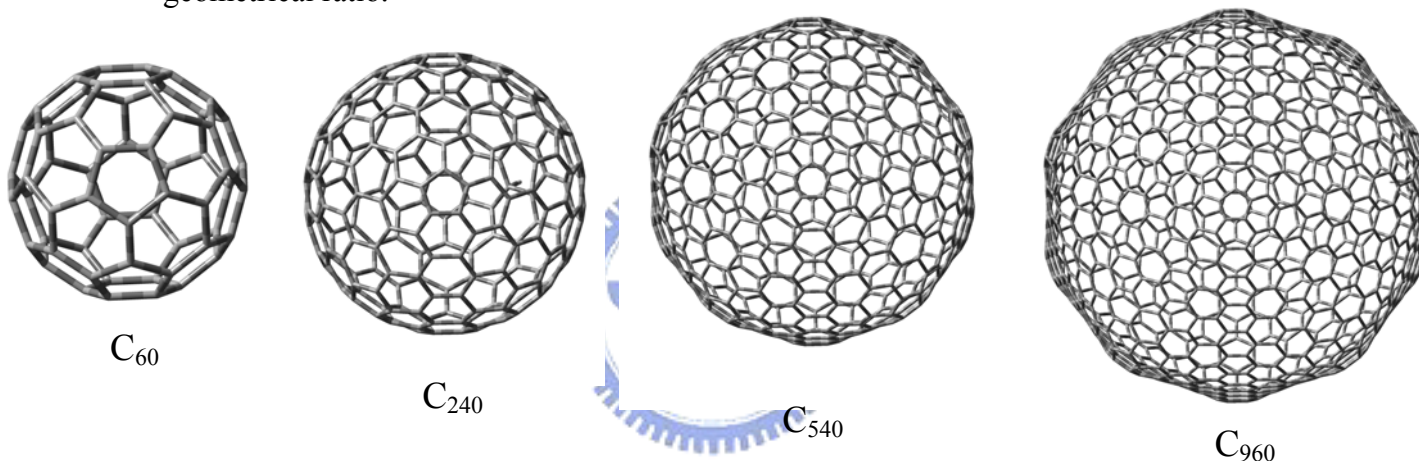


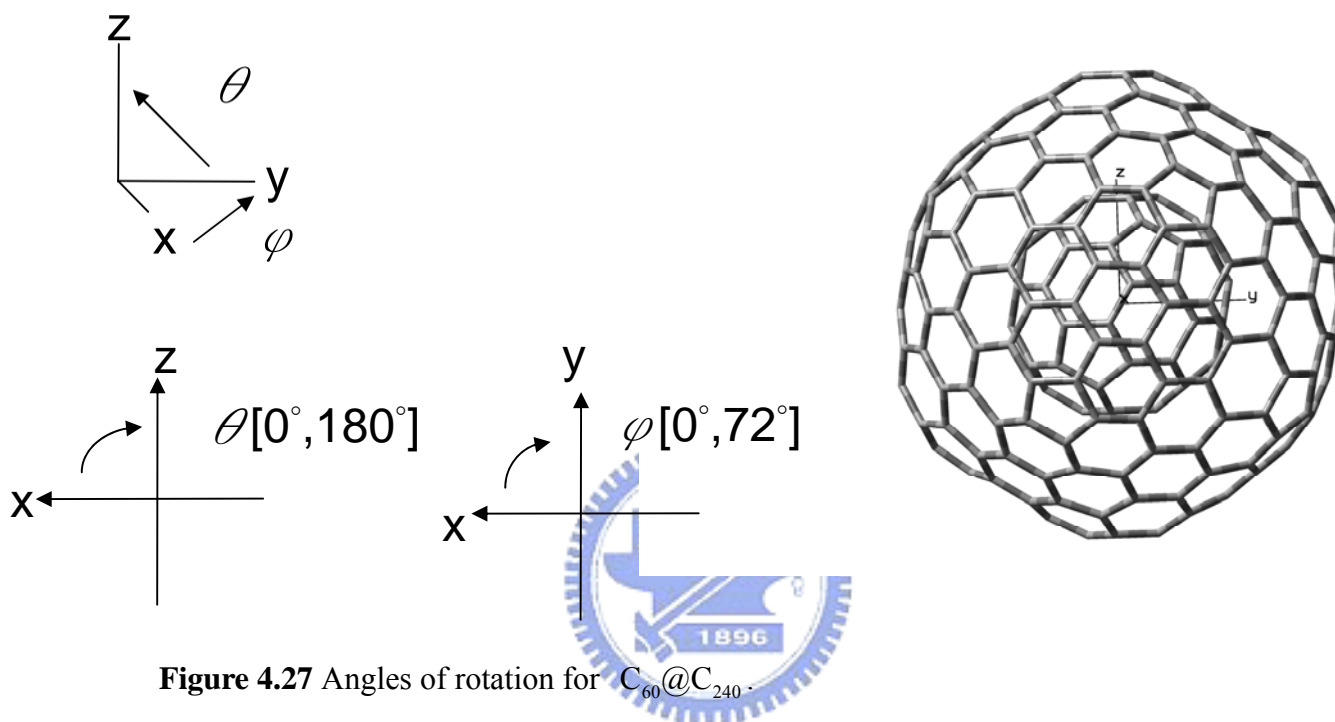
**Figure 4.26** Structures of the icosahedral fullerenes considered in this study.

#### 4.4.2 Potential Energy Scan (PES) of $C_{60}@C_{240}$ -Search for The Most Stable Structure

It is interesting to investigate how the fullerene behaves if they are combined together. Several articles had been focused on the energies and structures of the multi-shell fullerenes. Trying to capture the possible conformations of both the inner and outer cage, we present the PES of  $C_{60}@C_{240}$  using the SCC-DFTB method.

We combine the  $I_h$   $C_{60}$  and  $C_{240}$  structures optimized at the SCC-DFTB level. The setting of the Cartesian coordinates are shown in Figure 4.27, the distance measured between the five-membered rings of both fullerenes is 3.952 Å. To obtain a fine energy profile, we rotate the  $C_{60}$  every one degree from  $0^\circ$  to  $180^\circ$  vertically and from

$0^\circ$  to  $72^\circ$  horizontally. These two rotations form the repeating unit of the real PES and include all the possible conformations. Other combinations of  $\theta$  and  $\varphi$  will just repeat the energy in the repeating unit. The notations of angles and direction of rotation are also presented in Figure 4.27.



We used both Slater-Kirkwood and Lennard-Jones dispersive interaction models for this PES scan. Before discussing the PES of  $C_{60}@C_{240}$ , the two dispersion models should be compared to see which one is more accurate. We performed a benchmark calculation for these models. We adapt the benzene dimer as a testing system<sup>105-107</sup>. There exist three different arrangements of the benzene dimer. They are sandwich, T-shaped and parallel-displaced, respectively. The geometries of these structures are shown in Figure 4.28.

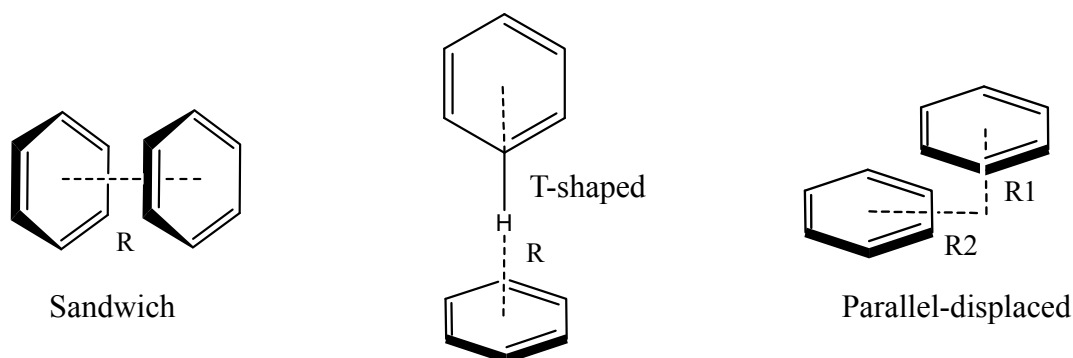


**Figure 4.28** The three different orientations of the benzene dimer.

We first optimized the geometry for a single benzene ring, then we made the different arrangements in Figure 4.28 by this unit. The computed results are shown in Figure 4.29 and compared with the results obtained from estimated CCSD(T)/aug-cc-pVQZ\*<sup>106</sup>. For the sandwich conformation, the energy is reported to be -1.70 kcal/mol by ref 106, and the inter-ring distance R is 3.9 Å. For the SCC-DFTB calculations, both LJ and SK show two potential wells in the potential energy curve.

Although the LJ model has a stronger overestimation of interaction energy, it reflects the R mode accurately compared with the high level *ab-initio* result. For the T-shaped arrangement, the energy and distance from ref 106 are -2.61 kcal/mol and 5.1 Å. both models have their energy minimum at the same R = 5.30 Å, but the minimum for LJ is lower. There are two geometrical parameters, R1 and R2, determining the parallel-displaced conformation (Figure 4.28). Ref10 reported R1 to be 3.6 Å and R2 to be 1.6 Å. The energy of this combination is -2.63 kcal/mol. Our results, for both models, show that R1 equals to 2.9Å and R2 equals to 2.6 Å. The energies are both around -8 kcal/mol, but the energy for LJ is lower.

In conclusion, comparing with the high level *ab-initio* calculation, SCC-DFTB dispersion models give qualitatively correct results. Further, the LJ potential is always



lower in energy for the three different benzene dimer conformations. The results from both SK and LJ are comparably identical, but in the case of sandwich benzene dimer, the LJ model predicts the distance more accurately.

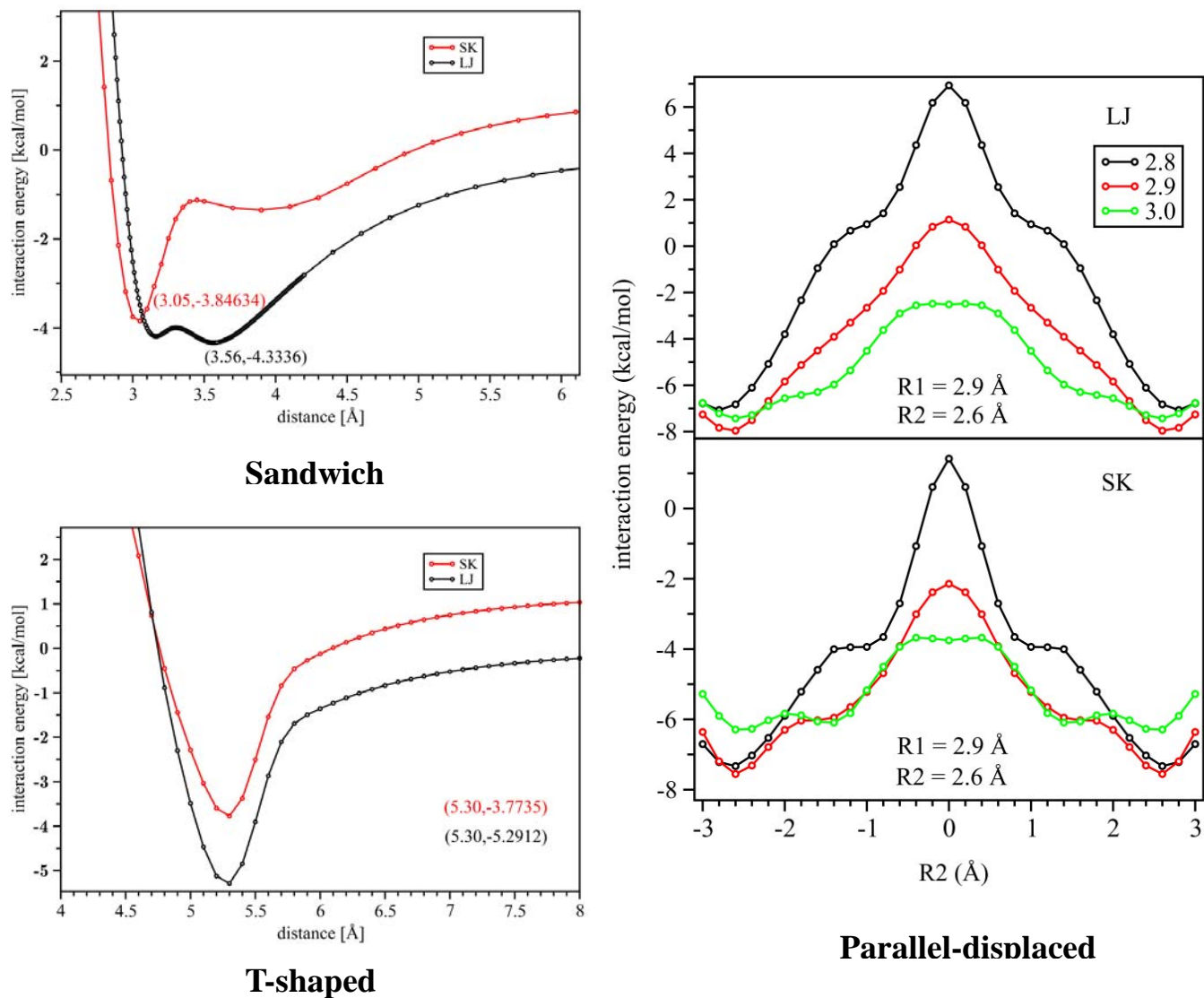


**Figure 4.29** The potential energy curves of the three different benzene dimers.

Unfortunately, owing to the numerical problem while solving the generalized eigenvalue problem, we currently have completed the PES of  $C_{60}@C_{240}$  by using the LJ model. The most important feature can be found: the very small energy fluctuation is found. As presented in the energy scale of Figure 4.30, this small energy difference corresponds to the extremely low critical temperature, which indicates that  $C_{60}$  is

freely rotating inside  $C_{240}$ .

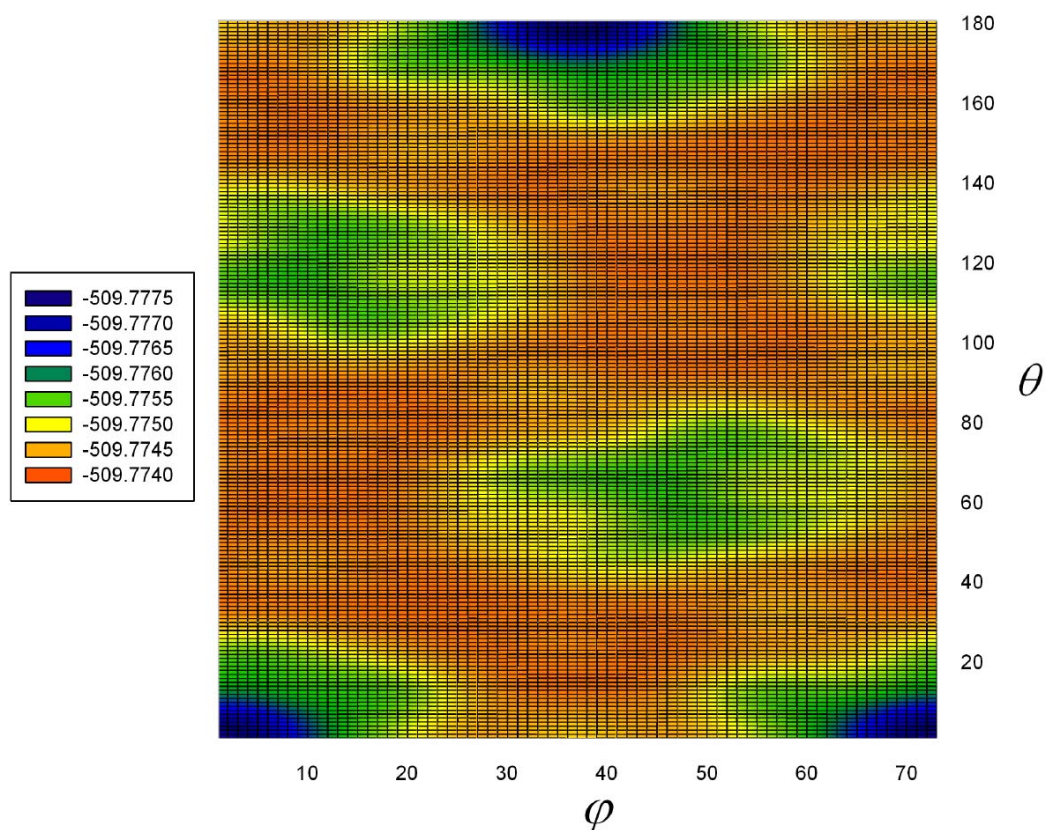
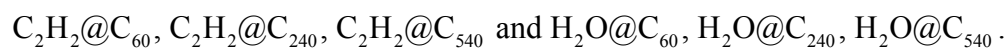


**Figure 4.30** The PES of  $C_{60}@C_{240}$  using the LJ model. Energy in Hartree.

### 4.4.3 Signal Shielding in the Vibrational Spectra

#### 4.4.3.1 Endohedral Fullerenes

Two series of systems were chosen as the models for endohedral fullerenes:



Based on the present investigation, we can conclude that if the space between the fullerene cage and the inserted molecule is large enough, then the vibrational signals from the small molecule are completely masked by the signals from the cage. The resulting IR spectra are given in Figure 4.31 and Raman spectra are in Figure 4.32. Next, we will analyze the deformation of the outer cage and the interaction between cages.



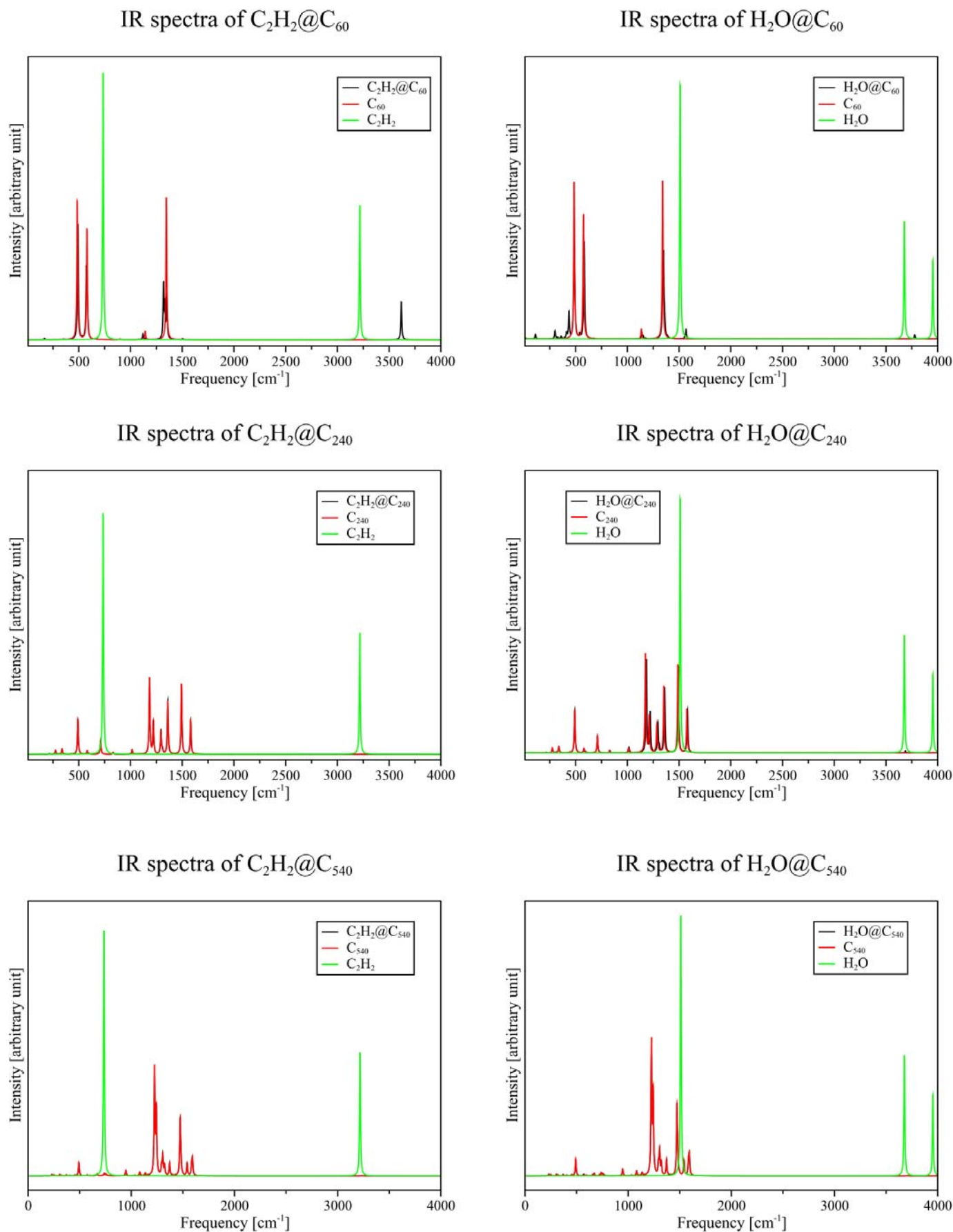
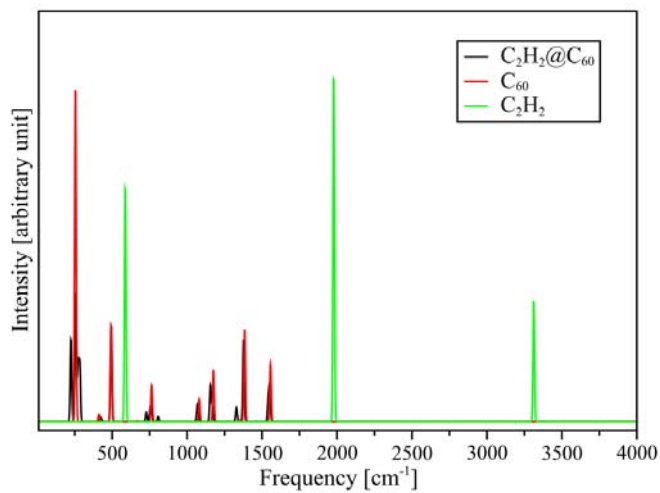
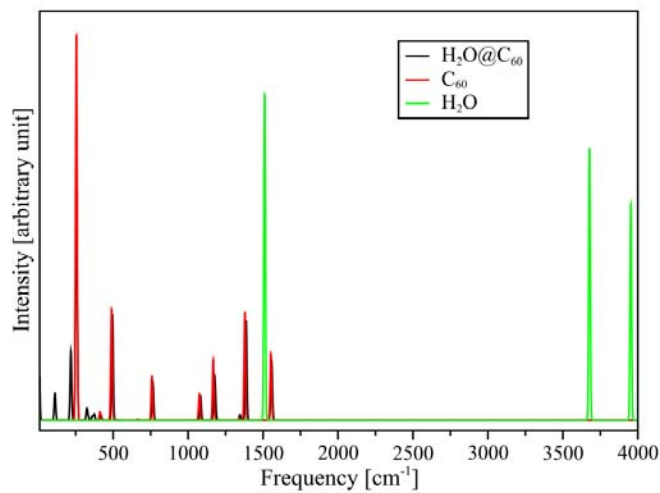


**Figure 4.31** IR spectra of the endohedral fullerenes.

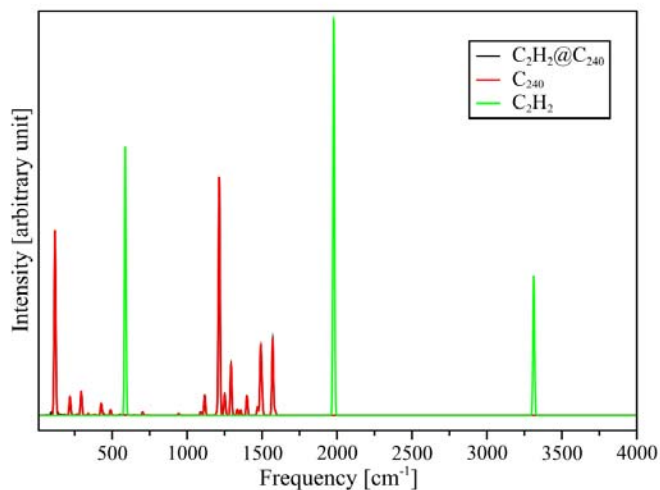
Raman spectra of  $C_2H_2@C_{60}$



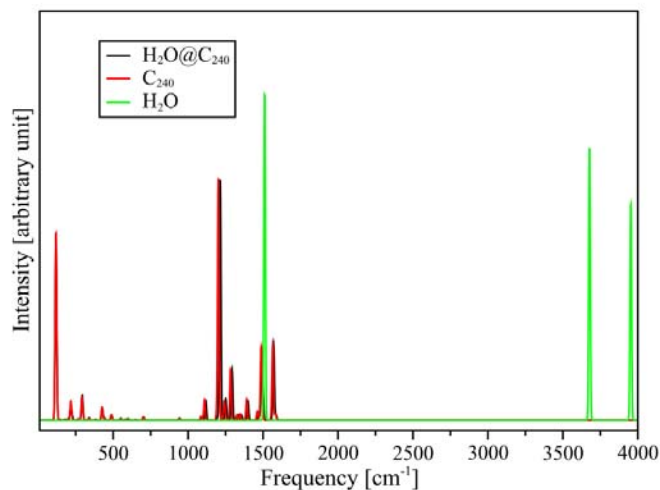
Raman spectra of  $H_2O@C_{60}$



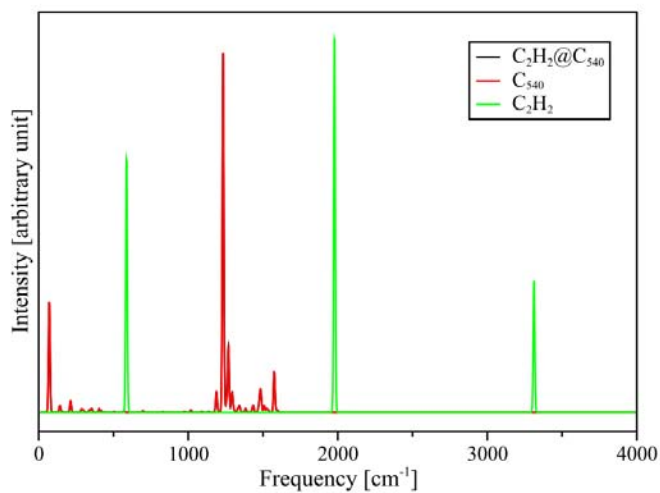
Raman spectra of  $C_2H_2@C_{240}$



Raman spectra of  $H_2O@C_{240}$



Raman spectra of  $C_2H_2@C_{540}$



Raman spectra of  $H_2O@C_{540}$

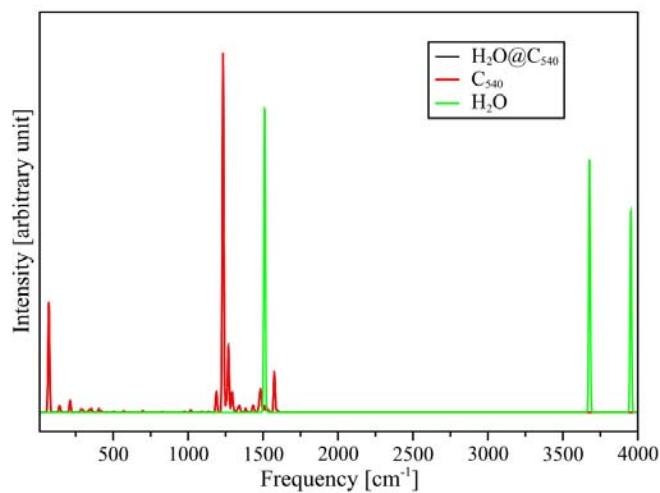
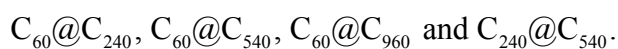


**Figure 4.32** Raman spectra of the endohedral fullerenes.

### 4.4.3.2 Multi-shell Fullerenes

In this topic, the nested fullerenes under study are:



and three-layer multi-shell fullerenes:



The optimized geometries of the systems are given in Figure 4.33

For the reason of clarity, we changed the color of some inner fullerenes to reveal the orientation of the inner fullerene. As pointed out in the PES study of  $C_{60}@C_{240}$ , the energy barrier for the molecule to rotate inside a fullerene cage is extremely small. Thus the inner molecule can be regarded as freely rotating inside the cage. This indicates that there exist vast of energetic local minima on the PES of these systems. Hence the geometrical optimization can not assure to reach the genuine global minimum. Again similar to the endohedral fullerenes, the inner cages initially stay in the middle in the first optimized structures of larger-outer-cage systems, but turns out that these geometries have imaginary vibrational frequencies, and the imaginary modes are actually translation of the inner cages, making them displace from the origin. Further optimizations along the imaginary modes provide lead us to the geometries that the inner cages are not in the center anymore, even in the case of  $C_{60}@C_{540}$ ,  $C_{60}$  rotated to overlap its hexagonal ring to the pentagonal ring of  $C_{540}$ . The imaginary modes are removed for these further-optimized geometries. Note that although the molecules are allowed to rotate inside the outer cage, most of the multi-shell systems still keep the inner cage in the middle, this conformation may make the all the pentagonal rings and hexagonal rings from different cages overlap most, strengthen the dispersive attraction, hence lower the energy of the system. The vibrational spectra are shown in Figure 4.34 for IR and Figure 4.35 for Raman.

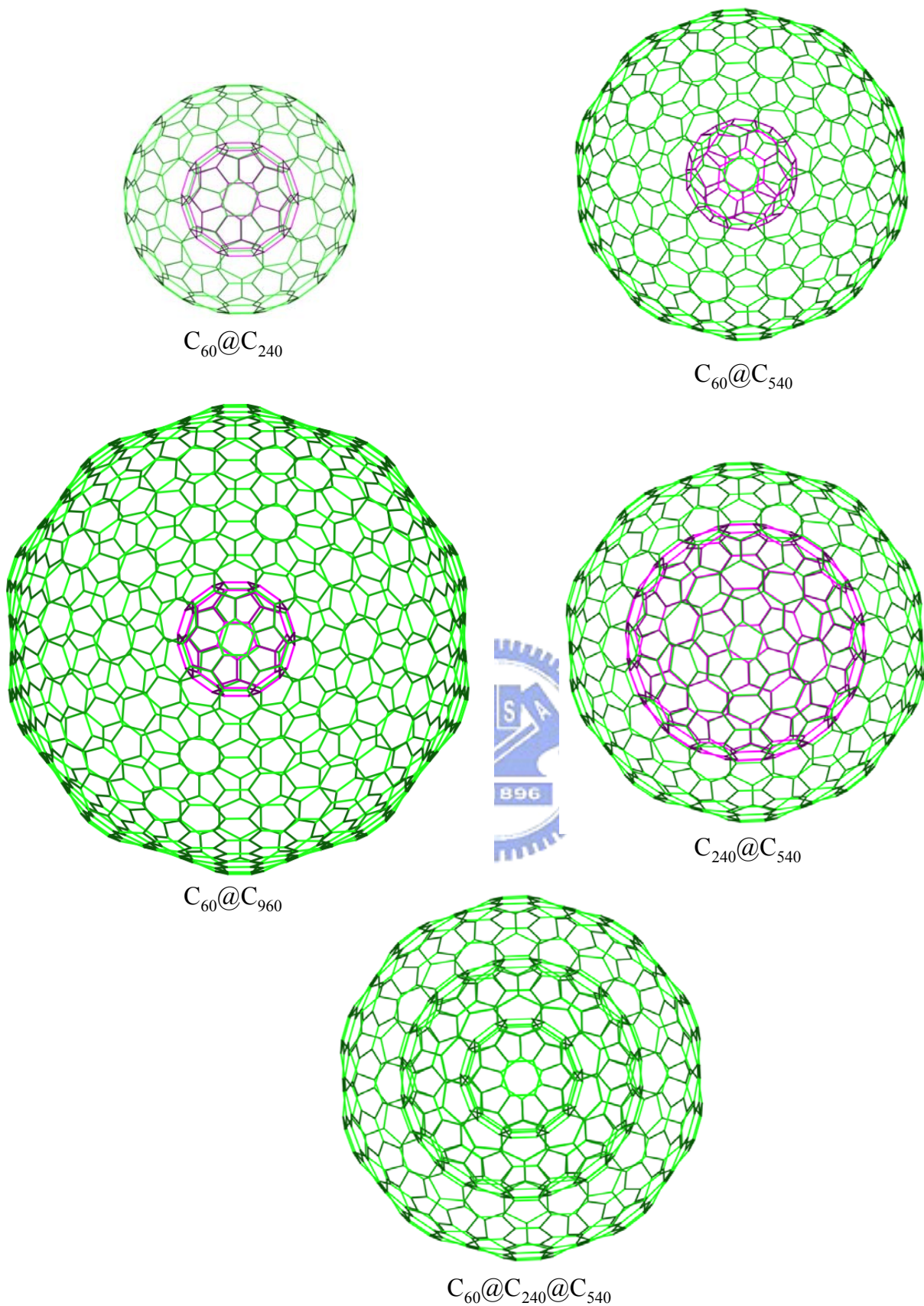
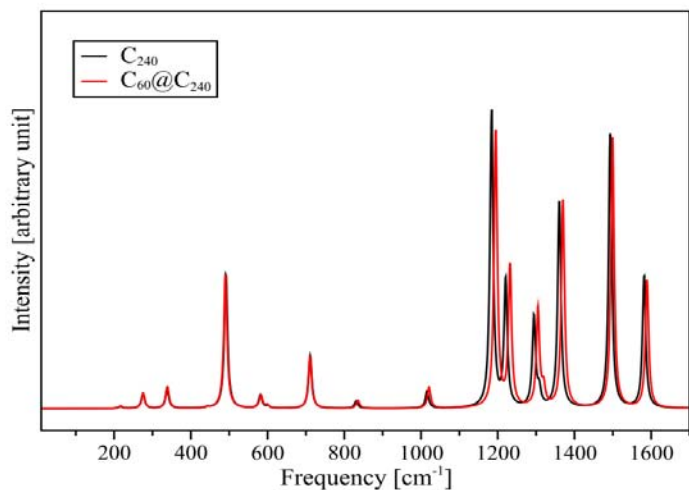
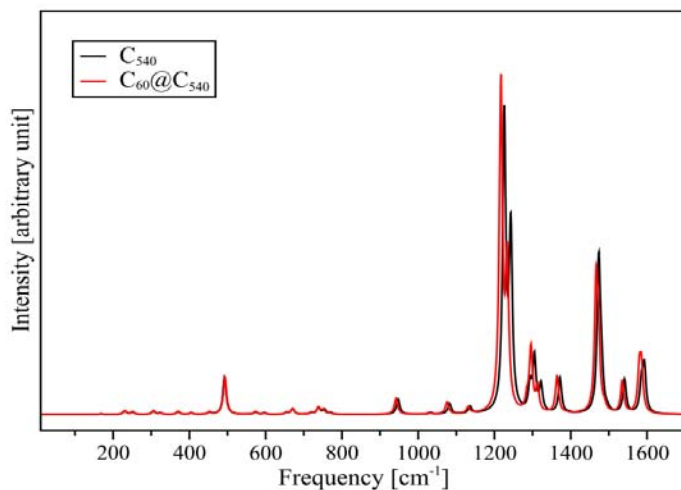


**Figure 4.33** Models of all the considered multi-shell fullerenes. Except for  $C_{60}@C_{240}@C_{540}$ , the color of the inner fullerenes are changed to purple for the multi-shell fullerenes

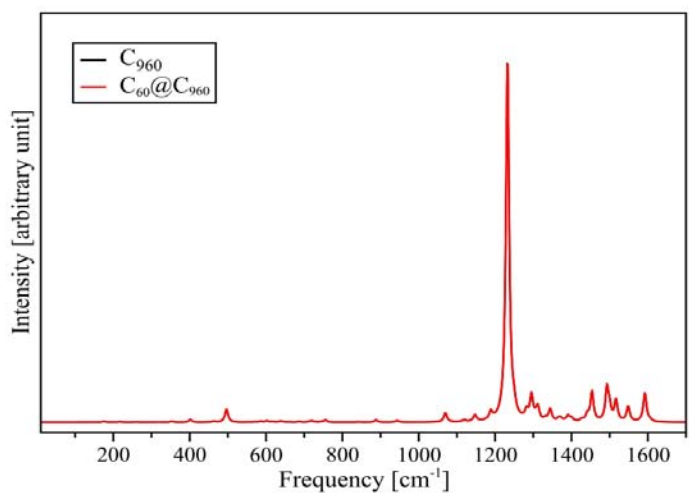
IR spectra of  $C_{60}@C_{240}$



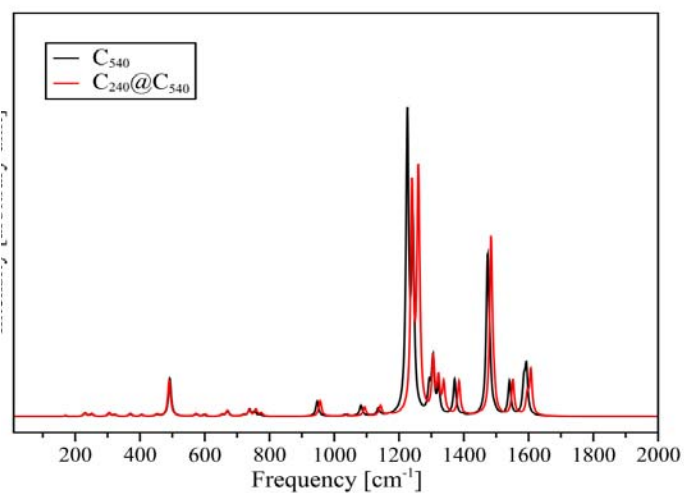
IR spectra of  $C_{60}@C_{540}$



IR spectra of  $C_{60}@C_{960}$



IR spectra of  $C_{240}@C_{540}$



IR spectra of  $C_{60}@C_{240}@C_{540}$

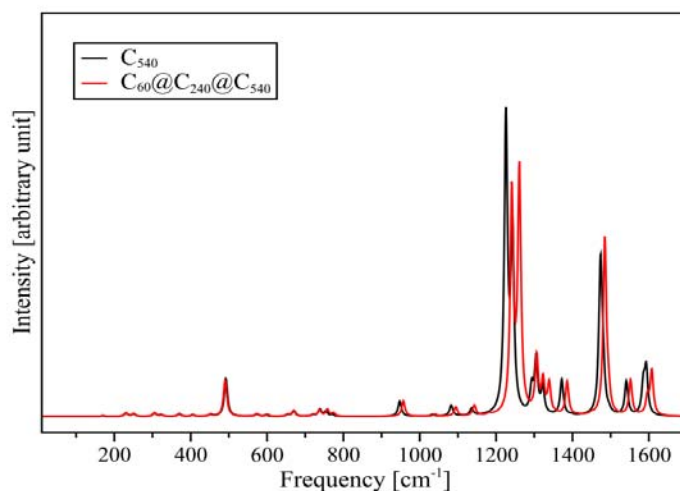
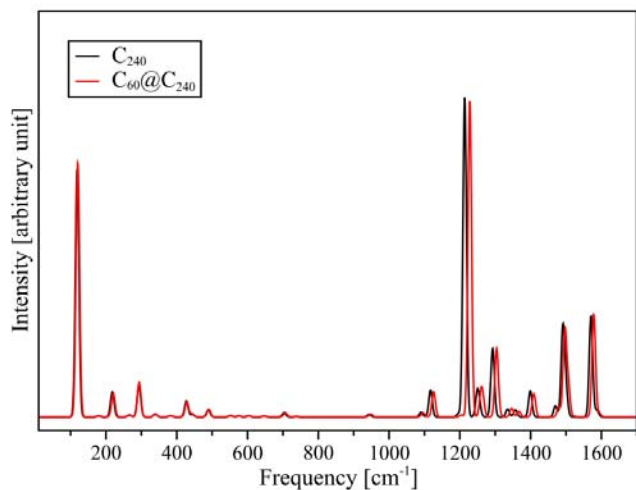


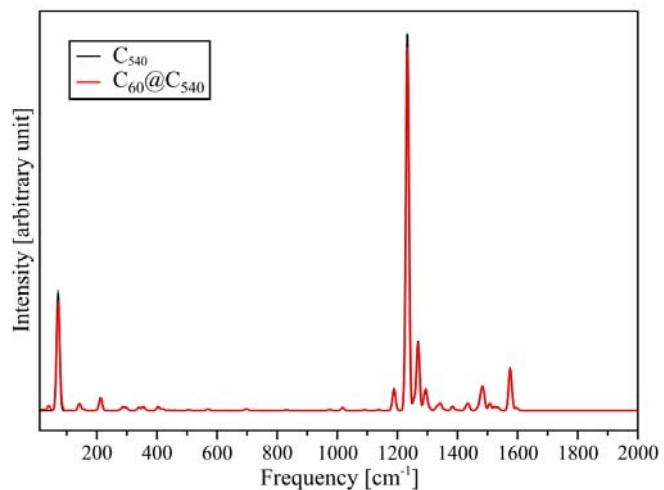
**Figure 4.34** IR spectra of multi-shell fullerenes.



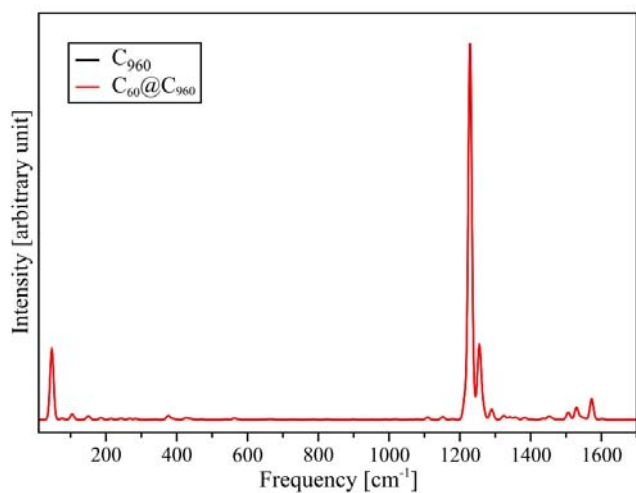
Raman spectra of  $C_{60}@C_{240}$



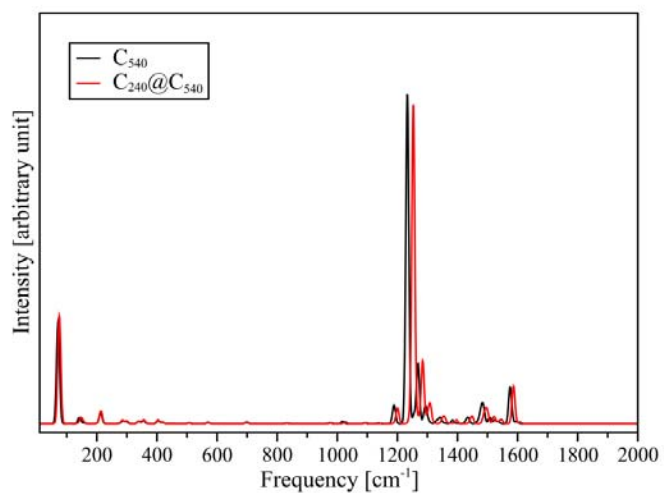
Raman spectra of  $C_{60}@C_{540}$



Raman spectra of  $C_{60}@C_{960}$



Raman spectra of  $C_{240}@C_{540}$



Raman spectra of  $C_{60}@C_{240}@C_{540}$

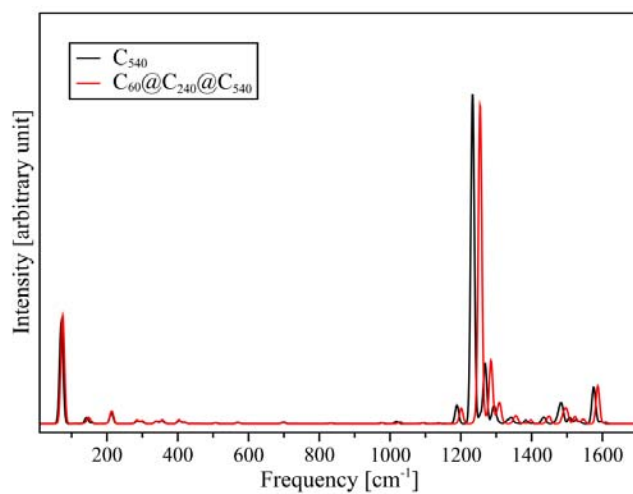



**Figure 4.35** Raman spectra of multi-shell fullerenes.

Similar to the endohedral fullerenes, the vibrational spectra of multi-shell fullerenes present only the signals from the outer cage, the signals from the inner shells are totally shielded.

In the larger-cage cases, the inner fullerenes will no longer stay in the center of the outer cage. Rather, they travel to approach the wall of the outer cage. The inter-cage distances are in the range of the vdW interaction, implying that the final position of the inner cage is making the inter-cage dispersion interaction, thus lowers the total energy of the system. Further analysis has to be done on the vibrational mode couplings of the inner molecules and outer cage in the smaller-outer-cage systems.

## 4.4 Raman Spectra of Single-Wall Carbon Nanotubes

### (SWNTs)



SWNTs can be classified into three categories: armchair, zig-zag and chiral. This classification is according to how they are made by the combination of the indices  $(m,n)$ , with  $m$  and  $n$  positive integers.<sup>8</sup> And  $m = n$  for armchair nanotubes,  $m = 0$  for zig-zag tubes, and  $m \neq n$  for chiral ones. In present study, we have chosen the armchair SWNTs with different tube diameters and lengths. Their ends are saturated with hydrogen atoms. The models chosen in this study are listed in table 4.5

**Table 4.5** List of the SWNTs considered in this study.

indices	(4,4)	(5,5)	(6,6)	(7,7)	(8,8)	(9,9)	(10,10)
length (nm)	1	1	1	1	1	1	1
	2	2	2	2	2	2	2
	3	3	3	3	3	3	3
	4	4	4	4	4	4	4
	5	5	5	5	5	5	5
	6	6					
	7	7					
	8	8					
	9	9					
	10	10					
	13	13					

One example of the CNT structures is given below

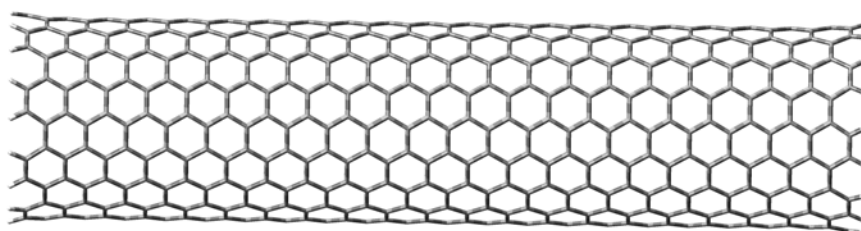


**Figure 4.36** Model of (9,9) 5nm SWNT.

The main goal of this study is to observe the convergence of the Raman spectra of finite SWNT toward infinite SWNT. The Raman spectra of real SWNTs contain three principal bands, one is called the ring breathing mode (RBM) at the frequency  $\sim 200 \text{ cm}^{-1}$ , the second and third ones are the same as those of graphite – the D band  $\sim 1350 \text{ cm}^{-1}$  due to disorder and the G band at around  $1580 \text{ cm}^{-1}$  due to carbons in the aromatic rings in graphite.<sup>8</sup> According to the original paper from Tour *et al*, the Raman spectra of ultra short SWNTs may vary from the usual SWNT.<sup>108</sup> Figure 4.37 shows the SCC-DFTB calculated Raman spectra of the armchair SWNTs various



sets of diameter and length. The half-width of the Gaussians smearing the Raman intensity is  $1.5 \text{ cm}^{-1}$ . Unfortunately, even for the longest model with length equals to 13 nm, the sign of the typical G band can not be found in the computed spectra. Only in the 13 nm (4,4) SWNT, the D band drastically decays compared with other (4,4) SWNTs.

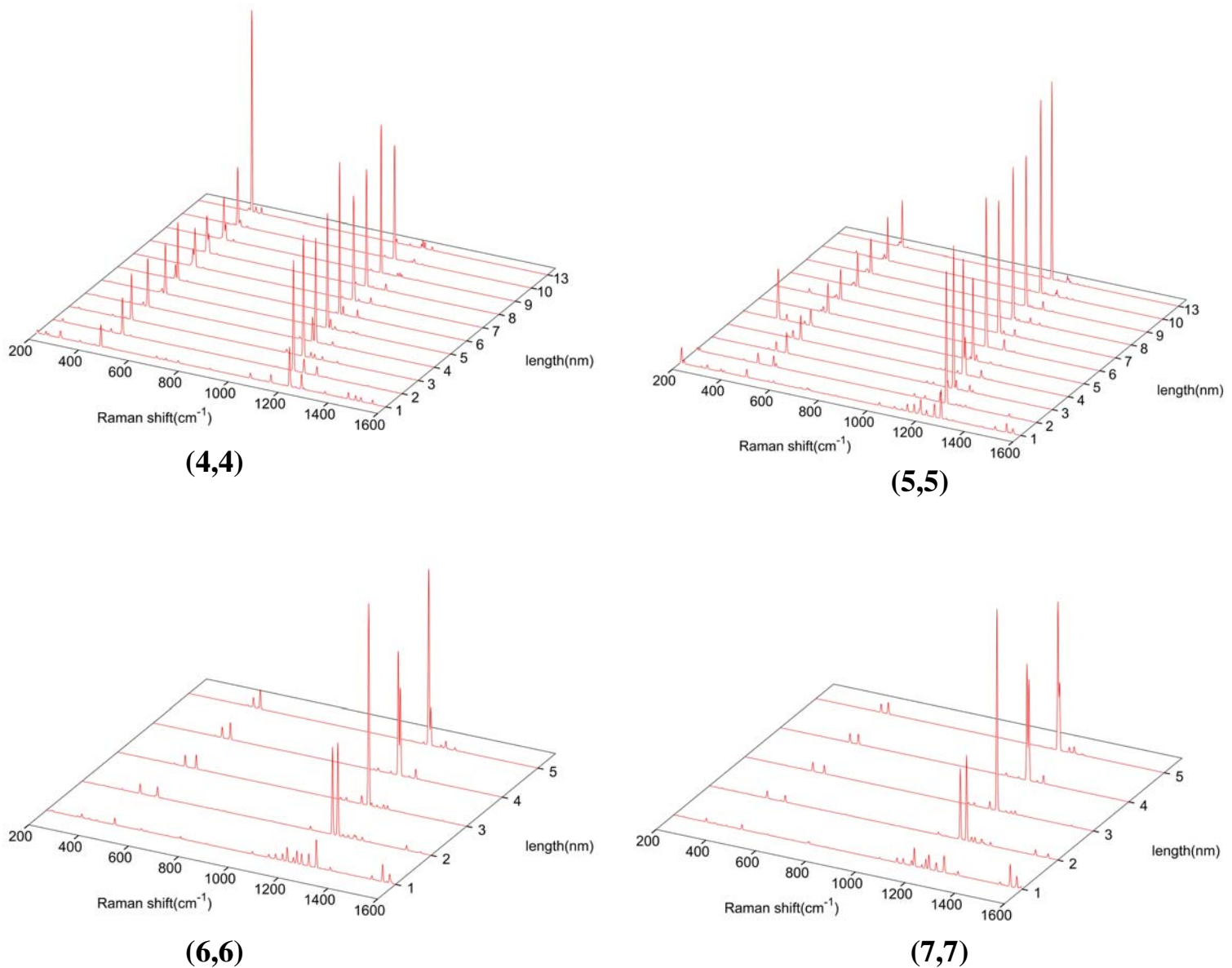
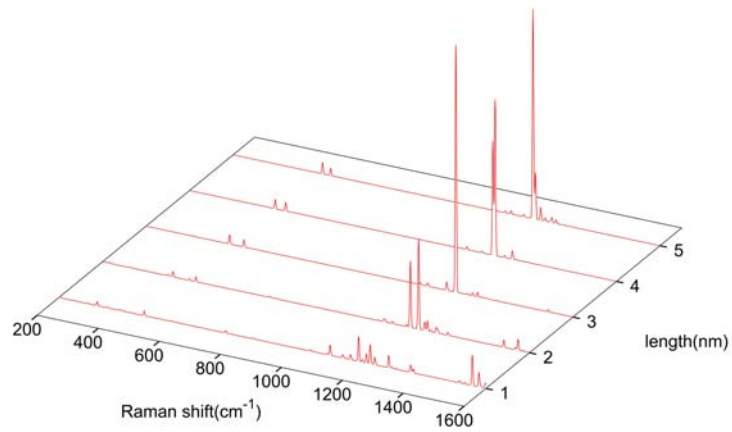
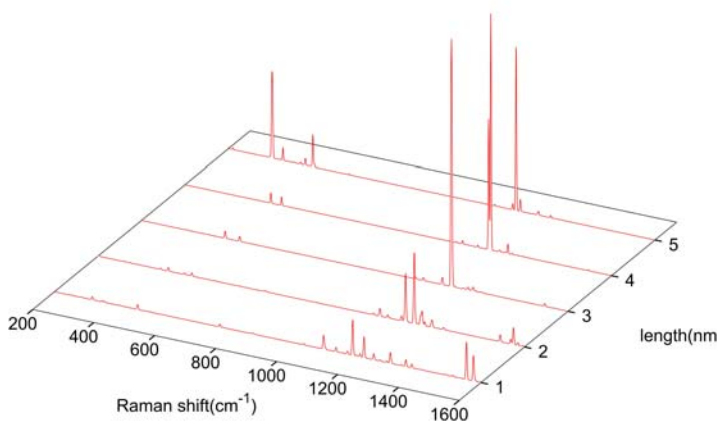


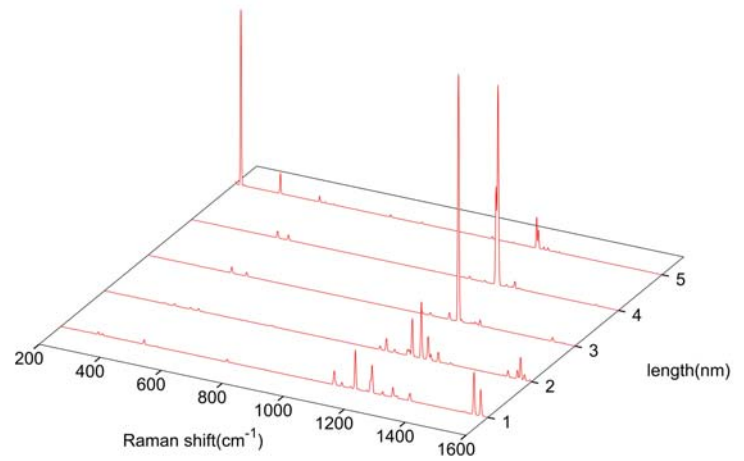
**Figure 4.37** Raman spectra of SWNTs considered in this study.



**(8,8)**



**(9,9)**



**(10,10)**

**Figure 4.37** continued.

# Chapter 5

## Conclusions

The SCC-DFTB method had been applied for studying the geometrical, electronic and vibrational properties of the  $\pi$  conjugated polymer chains and carbon nanostructures.

For the  $\pi$  conjugated polymeric systems, we have studied the evolutions of geometry, DOS and energy gaps, induced atomic charges, dipole and quadrupole moments as well as polarizabilities in five series of linear oligomers. Each of the series contained oligomers containing from one to 50 monomer units. The monomers were *cis*-butadiene, cyclopentadiene and three most common heterocyclic unsaturated rings: furan, pyrrole and thiophene. We found that the most of the studied properties show pronounced convergence towards constant values. Analysis of geometry and induced atomic charges of individual monomer units along the oligomer chain showed that for quite short chains (20-mers) the interior of the chain is virtually indistinguishable from the corresponding polymer, calculated at the same level of theory. Only several terminal units—about 3 to 4 for geometries and charges—showed deviations from the bulk values. Such a fast convergence of the geometric parameters as well as atomic charges is of great practical importance as it allows for investigating quasi-one dimensional polymers using relatively small, molecular models. This observation should thus simplify both experimental and theoretical studies on such properties of polymers as reactivity, interactions between

the polymer chains or influence of structural defects on the chain geometry and charge distribution. Similarly, the fast, convergent behavior of the electronic DOSs allows for theoretical insight into the band gaps and conductive properties of polymers from the oligomer level. This should be especially convenient in studying the energetics of the guest electronic levels appearing after doping the oligomer with electron-deficient or electron-rich atoms. Note that in order to quantitatively reproduce the energy gap, one has to consider longer oligomers than those appropriate for studying geometry or charge related properties, since the convergence of the HOMO-LUMO gap with increasing chain length is slower than the evolution of e.g. charge distribution. Some of the properties we have investigated show even slower convergence towards the infinite limits. In fact, quadrupole moments and polarizabilities seem not to reach saturation whatsoever, even if they are renormalized to the “property per monomer” values. This clearly shows that for these properties using the oligomer approach is not directly applicable to characterize the corresponding polymers, for which the contributions from individual monomers are obviously constant. Apparently, the second (and likely also higher) order tensor properties are extremely sensitive to the presence of the terminal parts of the oligomer chains, which cannot be neglected even for very long molecules. The contributions to those tensor properties from monomer units localized in the oligomer interior may still prove resemble those of polymers. Currently an investigation into this issue is under way in our laboratory.

For the nanodiamonds, two different types of structures belonging to the  $T_d$  point group have been studied, which are octahedral diamonds and tetrahedral diamonds. At around  $1200\text{ cm}^{-1}$ , the peaks shown in the SCC-DFTB Raman spectra of both series of nanodiamonds are coalescing and growing in intensity. Most of these peaks are of  $T_2$  symmetry. Furthermore, the evolution of the Raman spectra of “infH” nanodiamonds is consistent with the normal spectra. Both kinds of spectra offer the sign of the

unique  $1332\text{ cm}^{-1}$  peak of experimental Raman spectra of single crystal diamond. This suggests that for diamond, we have reached the border between the molecular stage and the solid-state stage and the  $\sim 1200\text{ cm}^{-1}$  band shown in the SCC-DFTB Raman spectra is corresponding to the experimental  $1332\text{ cm}^{-1}$  peak

The calculated Raman spectra of PAHs show that for both graphene flakes and HPBs growing in molecular size, the intensity of the  $\sim 1600\text{ cm}^{-1}$   $E_{2g}$  peak decays. In graphene, the intensity of the  $\sim 1200\text{ cm}^{-1}$   $A_{1g}$  peaks decrease drastically after C10, suggesting that the transformation of the D/G ratio occurs. But for the HPBs the intensity of the  $A_{1g}$  peaks does not show any significant change. It is possible that the studied models are still too small to provide a clear picture of the molecule-to-solid transition.

The PES of the multi-shell fullerene  $C_{60}@C_{240}$  was scanned by the SCC-DFTB+ code using the LJ dispersion potential. In the most stable conformation for this complex is all the five- and six-membered rings of the two fullerenes overlap perfectly, which results in the same  $I_h$  symmetry as the single-cage fullerenes. The computed energy barrier is merely 1.6 kcal/mol, presenting a picture that the  $C_{60}$  can freely rotate inside  $C_{240}$ .

Both the single-shell fullerenes and multi-shell fullerenes (include the endohedral ones) had been studied with a special focus on their Raman spectra. The signal shielding effect was found for both cases. Auxiliary signals will appear in the spectra if the inserted molecule and the outer cage are close to each other; these signals are probably due to the dispersion interaction between the two shells.

By studying the Raman spectra of armchair SWNT series, the characters of the experimental Raman spectra has not been recovered for the 15 nm (5,5) SWNT.

Some of the projects reported in this Thesis are still under investigations and more convincing and complete results will be presented in the future.

## References

- (1) Jensen, F. *Introduction to Computational Chemistry*, 1 ed.; John Wiley & Sons.
- (2) Kittel, C. *Introduction to Solid State Physics*; John Wiley & Sons 2005.
- (3) Mermin, N. W. A. N. D. *Solid State Physics*; Brooks/Cole, 1976.
- (4) Elstner, M.; Porezag, D.; Jungnickel, G.; Elsner, J.; Haugk, M.; Frauenheim, T.; Suhai, S.; Seifert, G. *Physical Review B* **1998**, *58*, 7260.
- (5) Witek, H. A.; Morokuma, K. *Journal of Computational Chemistry* **2004**, *25*, 1858.
- (6) Frauenheim, T.; Seifert, G.; Elstner, M.; Hajnal, Z.; Jungnickel, G.; Porezag, D.; Suhai, S.; Scholz, R. *Physica Status Solidi B-Basic Solid State Physics* **2000**, *217*, 41.
- (7) Ferrari, A. C.; Robertson, J. *Physical Review B* **2000**, *61*, 14095.
- (8) Dresselhaus, M. S.; Dresselhaus, G.; Saito, R.; Jorio, A. *Physics Reports-Review Section of Physics Letters* **2005**, *409*, 47.
- (9) Dronskowski, R. *Computational Chemistry of Solid State Materials* 139 ed., 2005.
- (10) Elliott, S. *The Physics and Chemistry of Solids*; John Wiley & Sons 1998.
- (11) McHale, J. L. *Molecular Spectroscopy*, 1 ed.; PRENTICE HALL, Upper Saddle River, New Jersey 07458, 1999.
- (12) Long, D. A. *The Raman effect - a unified treatment of the theory of Raman scattering by molecules*; John Wiley & Sons, 2002.
- (13) Matthew, W.; Foulkes, C.; Haydock, R. *Physical Review B* **1989**, *39*, 12520.
- (14) Koster, J. C. S. G. F. *Physical Review* **1954**, *94*.
- (15) Kohn, P. H. W. *Physical Review* **1964**, *136*.
- (16) Porezag, D.; Frauenheim, T.; Kohler, T.; Seifert, G.; Kaschner, R. *Physical Review B* **1995**, *51*, 12947.
- (17) J. F. Dobson, B. P. D., J. Wang *Electronic Density Functional Theory: Recent Progress and New Directions*; Plenum, New York, 1997.
- (18) Elstner, M.; Hobza, P.; Frauenheim, T.; Suhai, S.; Kaxiras, E. *Journal of Chemical Physics* **2001**, *114*, 5149.
- (19) Zhechkov, L.; Heine, T.; Patchkovskii, S.; Seifert, G.; Duarte, H. A. *Journal of Chemical Theory and Computation* **2005**, *1*, 841.

- (20) Halgren, T. A. *Journal of the American Chemical Society* **1992**, *114*, 7827.
- (21) Rappe, A. K.; Casewit, C. J.; Colwell, K. S.; Goddard, W. A.; Skiff, W. M. *Journal of the American Chemical Society* **1992**, *114*, 10024.
- (22) Witek, H. A.; Irle, S.; Morokuma, K. *Journal of Chemical Physics* **2004**, *121*, 5163.
- (23) Witek, H. A.; Morokuma, K.; Stradomska, A. *Journal of Chemical Physics* **2004**, *121*, 5171.
- (24) Witek, H. A.; Morokuma, K.; Stradomska, A. *Journal of Theoretical & Computational Chemistry* **2005**, *4*, 639.
- (25) Aradi, B.; Hourahine, B.; Frauenheim, T. *J Phys Chem A* **2007**, *111*, 5678.
- (26) Karpfen, A.; Kertesz, M. *Journal of Physical Chemistry* **1991**, *95*, 7680.
- (27) Zotti, G.; Martina, S.; Wegner, G.; Schluter, A. D. *Advanced Materials* **1992**, *4*, 798.
- (28) Roncali, J.; Yassar, A.; Garnier, F. *Journal of the Chemical Society-Chemical Communications* **1988**, 581.
- (29) Glenis, S.; Benz, M.; Legoff, E.; Schindler, J. L.; Kannewurf, C. R.; Kanatzidis, M. G. *Journal of the American Chemical Society* **1993**, *115*, 12519.
- (30) Chung, T. C.; Kaufman, J. H.; Heeger, A. J.; Wudl, F. *Physical Review B* **1984**, *30*, 702.
- (31) Hong, S. Y.; Marynick, D. S. *Macromolecules* **1995**, *28*, 4991.
- (32) Hong, S. Y.; Kwon, S. J.; Kim, S. C.; Marynick, D. S. *Synthetic Metals* **1995**, *69*, 701.
- (33) Hong, S. Y.; Kwon, S. J.; Kim, S. C. *Journal of Chemical Physics* **1995**, *103*, 1871.
- (34) Hissler, M.; Dyer, P. W.; Reau, R. *Coordination Chemistry Reviews* **2003**, *244*, 1.
- (35) Hernandez, V.; Navarrete, J. T. L.; Marcos, J. I. *Synthetic Metals* **1991**, *41*, 789.
- (36) Bredas, J. L.; Scott, J. C.; Yakushi, K.; Street, G. B. *Physical Review B* **1984**, *30*, 1023.
- (37) Toussaint, J. M.; Bredas, J. L. *Synthetic Metals* **1995**, *69*, 637.
- (38) Kanazawa, K. K.; Diaz, A. F.; Geiss, R. H.; Gill, W. D.; Kwak, J. F.; Logan, J. A.; Rabolt, J. F.; Street, G. B. *Journal of the Chemical Society-Chemical Communications* **1979**, 854.
- (39) Ford, W. K.; Duke, C. B.; Salaneck, W. R. *Journal of Chemical Physics* **1982**, *77*, 5030.
- (40) Kertesz, M.; Choi, C. H.; Yang, S. J. *Chemical Reviews* **2005**, *105*, 3448.
- (41) Bakhshi, A. K.; Ladik, J.; Seel, M. *Physical Review B* **1987**, *35*, 704.



- (42) Hirata, S.; Torii, H.; Tasumi, M. *Physical Review B* **1998**, *57*, 11994.
- (43) Ma, J.; Li, S. H.; Jiang, Y. S. *Macromolecules* **2002**, *35*, 1109.
- (44) Salzner, U.; Lagowski, J. B.; Pickup, P. G.; Poirier, R. A. *Synthetic Metals* **1998**, *96*, 177.
- (45) Hutchison, G. R.; Ratner, M. A.; Marks, T. J. *Journal of Physical Chemistry A* **2002**, *106*, 10596.
- (46) Zade, S. S.; Bendikov, M. *Organic Letters* **2006**, *8*, 5243.
- (47) Zotti, G.; Comisso, N.; Daprano, G.; Leclerc, M. *Advanced Materials* **1992**, *4*, 749.
- (48) Chou, C. P.; Li, W. F.; Witek, H. A.; M. Andrzejak *Vibrational Spectroscopy Of Linear Carbon Chains*; World Scientific Singapore, 2009.
- (49) Shirakawa, H.; Louis, E. J.; Macdiarmid, A. G.; Chiang, C. K.; Heeger, A. J. *Journal of the Chemical Society-Chemical Communications* **1977**, 578.
- (50) Burroughes, J. H.; Bradley, D. D. C.; Brown, A. R.; Marks, R. N.; Mackay, K.; Friend, R. H.; Burns, P. L.; Holmes, A. B. *Nature* **1990**, *347*, 539.
- (51) Greenham, N. C.; Moratti, S. C.; Bradley, D. D. C.; Friend, R. H.; Holmes, A. B. *Nature* **1993**, *365*, 628.
- (52) Gross, M.; Muller, D. C.; Nothofer, H. G.; Scherf, U.; Neher, D.; Brauchle, C.; Meerholz, K. *Nature* **2000**, *405*, 661.
- (53) Bartlett, P. N.; Birkin, P. R. *Synthetic Metals* **1993**, *61*, 15.
- (54) Gerard, M.; Chaubey, A.; Malhotra, B. D. *Biosensors & Bioelectronics* **2002**, *17*, 345.
- (55) Granstrom, M.; Petritsch, K.; Arias, A. C.; Lux, A.; Andersson, M. R.; Friend, R. H. *Nature* **1998**, *395*, 257.
- (56) Whang, Y. E.; Miyata, S.; Salaneck, W. R.; I. Lundstrom; Ranby, B. *Conjugated Polymers and Related Materials* Oxford University Press, 1993.
- (57) Hutchison, G. R.; Zhao, Y. J.; Delley, B.; Freeman, A. J.; Ratner, M. A.; Marks, T. J. *Physical Review B* **2003**, *68*.
- (58) Zade, S. S.; Bendikov, M. *Chemistry-a European Journal* **2007**, *13*, 3688.
- (59) Vogel, E.; Sombroek, J.; Wagemann, W. *Angewandte Chemie International Edition in English* **1975**, *14*.
- (60) Vogel, E.; Roth, H. D. *Angewandte Chemie International Edition in English* **1964**, *3*.
- (61) Vogel, E.; Haberland, U.; Günther, H. *Angewandte Chemie International Edition in English* **1970**, *9*.
- (62) Vogel, E.; Deger, H. M.; Hebel, P.; Lex, J. *Angewandte Chemie International Edition in English* **1980**, *19*.
- (63) Scott, L. T.; Sumpter, C. A.; Gantzel, P. K.; Maverick, E.; Trueblood, K. N.



*Tetrahedron* **2001**, *57*, 3795.

(64) Haddon, R. C. *Journal of the American Chemical Society* **1987**, *109*, 1676.

(65) Norton, J. E.; Houk, K. N. *Journal of the American Chemical Society* **2005**, *127*, 4162.

(66) NIST Computational Chemistry Comparison and Benchmark Database, NIST Standard Reference Database Number 101  
Release 14, Sept 2006, Editor: Russell D. Johnson III  
<http://srdata.nist.gov/cccbdb>

(67) Note that this is a serious limitation of the SCC-DFTB method, since the quadrupole moment computed using a continuous orbital-based distribution of electron does not show such a behavior. Similar effect is also observed for polarizability.

(68) Zhao, M. T.; Singh, B. P.; Prasad, P. N. *Journal of Chemical Physics* **1988**, *89*, 5535.

(69) Tretiak, S.; Chernyak, V.; Mukamel, S. *Physical Review Letters* **1996**, *77*, 4656.

(70) Toto, J. L.; Toto, T. T.; Demelo, C. P.; Robins, K. A. *Journal of Chemical Physics* **1995**, *102*, 8048.

(71) Torrens, F.; Sanchez-Marin, J.; Nebot-Gil, I. *Theochem-Journal of Molecular Structure* **1998**, *426*, 105.

(72) Schulz, M.; Tretiak, S.; Chernyak, V.; Mukamel, S. *Journal of the American Chemical Society* **2000**, *122*, 452.

(73) Otto, P.; Piris, M.; Martinez, A.; Ladik, J. *Synthetic Metals* **2004**, *141*, 277.

(74) Leiva, P.; Martinez, A.; Otto, P. *Synthetic Metals* **2006**, *156*, 648.

(75) Kishino, S.; Ueno, Y.; Ochiai, K.; Rikukawa, M.; Sanui, K.; Kobayashi, T.; Kunugita, H.; Ema, K. *Physical Review B* **1998**, *58*, 13430.

(76) Delaere, D.; Nguyen, M. T.; Vanquickenborne, L. G. *Physical Chemistry Chemical Physics* **2002**, *4*, 1522.

(77) Dalskov, E. K.; Oddershede, J.; Bishop, D. M. *Journal of Chemical Physics* **1998**, *108*, 2152.

(78) Becke, A. D. *Journal of Chemical Physics* **1993**, *98*, 1372.

(79) Perdew, J. P.; Burke, K.; Ernzerhof, M. *Physical Review Letters* **1996**, *77*, 3865.

(80) Tommasini, M.; Fazzi, D.; Milani, A.; Del Zoppo, M.; Castiglioni, C.; Zerbi, G. *Journal of Physical Chemistry A* **2007**, *111*, 11645.

(81) Milani, A.; Tommasini, M.; Del Zoppo, M.; Castiglioni, C.; Zerbi, G. *Physical Review B* **2006**, *74*.

(82) Kohler, B. E.; Samuel, I. D. W. *Journal of Chemical Physics* **1995**, *103*,

6248.

(83) Champagne, B.; Perpete, E. A.; van Gisbergen, S. J. A.; Baerends, E. J.; Snijders, J. G.; Soubra-Ghaoui, C.; Robins, K. A.; Kirtman, B. *Journal of Chemical Physics* **1998**, *109*, 10489.

(84) Jensen, L.; Astrand, P. O.; Osted, A.; Kongsted, J.; Mikkelsen, K. V. *Journal of Chemical Physics* **2002**, *116*, 4001.

(85) Jensen, L.; Astrand, P. O.; Mikkelsen, K. V. *Journal of Physical Chemistry A* **2004**, *108*, 8795.

(86) Berger, J. A.; de Boeij, P. L.; van Leeuwen, R. *Journal of Chemical Physics* **2005**, *123*.

(87) Kurtz, H. A. *International Journal of Quantum Chemistry. Quantum Chemistry Symposium* **1990**, *24*.

(88) Champagne, B. *International Journal of Quantum Chemistry. Quantum Chemistry Symposium* **1993**, *27*.

(89) Yang, S. J.; Ollishevski, P.; Kertesz, M. *Synthetic Metals* **2004**, *141*, 171.

(90) Greiner, N. R.; Phillips, D. S.; Johnson, J. D.; Volk, F. *Nature* **1988**, *333*, 440.

(91) Yarbrough, W. A.; Messier, R. *Science* **1990**, *247*, 688.

(92) Bachmann, P. K.; Lade, H.; Leers, D.; Wiechert, D. U.; Theunissen, G. S. A. M. *Diamond and Related Materials* **1994**, *3*, 799.

(93) Dahl, J. E.; Liu, S. G.; Carlson, R. M. K. *Science* **2003**, *299*, 96.

(94) Zhang, D. J.; Zhang, R. Q. *Journal of Physical Chemistry B* **2005**, *109*, 9006.

(95) Filik, J.; Harvey, J. N.; Allan, N. L.; May, P. W.; Dahl, J. E. P.; Liu, S.; Carlson, R. M. K. *Physical Review B* **2006**, *74*.

(96) Negri, F.; Castiglioni, C.; Tommasini, M.; Zerbi, G. *Journal of Physical Chemistry A* **2002**, *106*, 3306.

(97) Izmaylov, A. F.; Scuseria, G. E. *Journal of Chemical Physics* **2007**, *127*.

(98) Shinohara, H.; Yamakita, Y.; Ohno, K. *Journal of Molecular Structure* **1998**, *442*, 221.

(99) Mapelli, C.; Castiglioni, C.; Zerbi, G.; Mullen, K. *Physical Review B* **1999**, *60*, 12710.

(100) Di Donato, E.; Tommasini, M.; Fustella, G.; Brambilla, L.; Castiglioni, C.; Zerbi, G.; Simpson, C. D.; Mullen, K.; Negri, F. *Chemical Physics* **2004**, *301*, 81.

(101) Kroto, H. W.; Heath, J. R.; O'Brien, S. C.; Curl, R. F.; Smalley, R. E. *Nature* **1985**, *318*, 162.

(102) Manolopoulos, P. W. F. D. E. *An Atlas of Fullerenes* Dover Publications, 2006.

- (103) Terrones, M.; Terrones, G.; Terrones, H. *Structural Chemistry* **2002**, *13*, 373.
- (104) Goldberg, M. *Tohoku Math Journal* **1937**, 443.
- (105) Jha, P. C.; Rinkevicius, Z.; Agren, H.; Seal, P.; Chakrabarti, S. *Physical Chemistry Chemical Physics* **2008**, *10*, 2715.
- (106) Sinnokrot, M. O.; Sherrill, C. D. *Journal of Physical Chemistry A* **2004**, *108*, 10200.
- (107) Sinnokrot, M. O.; Sherrill, C. D. *Journal of Physical Chemistry A* **2006**, *110*, 10656.
- (108) Chen, Z. Y.; Kobashi, K.; Rauwald, U.; Booker, R.; Fan, H.; Hwang, W. F.; Tour, J. M. *Journal of the American Chemical Society* **2006**, *128*, 10568.

